# Development of Electrodes and Coatings for Sodium Ion Energy Storage

by
Tyler Or

A thesis
presented to the University of Waterloo
in fulfillment of the
thesis requirement for the degree of
Master of Applied Science
in
Chemical Engineering

Waterloo, Ontario, Canada, 2020

## Author's Declaration

This thesis consists of material all of which I authored or co-authored: see Statement of Contributions included in the thesis. This is a true copy of the thesis, including any required final revisions, as accepted by my examiners.

I understand that my thesis may be made electronically available to the public.

## Statement of Contributions

**Section 1** was partially adapted from a published review manuscript that I co-authored:

Or, T.; Gourley, S. W. D.; Kaliyappan, K.; Yu, A.; Chen, Z. Recycling of Mixed Cathode Lithium-ion Batteries for Electric Vehicles: Current Status and Future Outlook. *Carbon Energy* **2020**, 2 (1), 6 – 43.

Tyler Or conducted the literature survey and prepared the manuscript, Storm W.D. Gourley and Dr. Karthikeyan Kaliyappan contributed to certain sections, figure designs, and revisions, and Dr. Aiping Yu and Dr. Zhongwei Chen designed the scope and revised the manuscript. All authors reviewed and approved the final version of the manuscript.

**Section 4** consists of a research manuscript submitted to *ChemElectroChem* that I co-authored:

Or, T.; Kaliyappan, K.; Bai, Z.; Chen, Z. High-Voltage Stability and Characterization of P2-$Na_{2/3}Mn_{1-y}Mg_yO_2$ Cathode For Sodium-Ion Batteries. *Submitted* **2020**.

Tyler Or conducted the study and wrote the manuscript. Dr. Karthikeyan Kaliyappan and Dr. Zhengyu Bai helped design the study, while Dr. Zhongwei Chen supervised the project. All authors reviewed and approved the final version of the manuscript.

**Section 5** consists of a published research manuscript that I co-authored:

Or, T.; Kaliyappan, K.; Li, G.; Abureden, S.; Bai, Z.; Chen, Z. $Na_2CoPO_4F$ as a Pseudocapacitive Anode for High-Performance and Ultrastable Hybrid Sodium-Ion Capacitors. *Electrochim. Acta* **2020**, 136024.

Tyler Or and Dr. Karthikeyan Kaliyappan contributed equally to the work. Dr. Gaoran Li, Dr. Salah Abureden, and Dr. Zhengyu Bai helped revise the manuscript while Dr. Zhongwei Chen supervised the project. All authors reviewed and approved the final version of the manuscript.

**Section 6** consists of work in progress intended for publication (venue undecided). Tyler Or designed and conducted the experiments, Dr. Karthikeyan Kaliyappan assisted with the experimental design and Dr. Zhongwei Chen supervised the project.

## Abstract

Sodium-ion energy storage technologies have recently garnered interest due to potential constraints in the supply of lithium in the distant future assuming that lithium-ion batteries (LIBs) are widely adopted for large-scale applications (*i.e.,* electric vehicles and stationary energy storage). Sodium-ion batteries (SIBs) possess an identical chemistry and operating mechanism to LIBs, and thus strategies from extensive LIB development are directly translatable. However, replacing $Li^+$ with $Na^+$ as the charge carrier presents significant challenges, notably the poor intercalation/de-intercalation reversibility in the host lattice and sluggish solid-state $Na^+$ diffusion kinetics due to the relatively large size of the $Na^+$ ion. It is critical to develop cathode materials that demonstrate high energy output and good reversibility, while being comprised of low-cost and abundant materials. On the other hand, hybrid Na-ion capacitors (NICs) are a different class of secondary energy storage designed to bridge the performance gap between SIBs and electric double-layer capacitors (EDLCs). They typically comprise of an insertion electrode and a carbonaceous capacitive electrode in an organic (carbonate-based) electrolyte and can deliver 3-4 times the energy density compared to EDLCs albeit with lower rate performance (energy output at high current) and cycle stability. However, while commercial supercapacitors are stable over millions of charge-discharge cycles, few reports in the literature on NICs demonstrate a capacity retention ≥90% over 10,000 cycles. The design, preparation, and improvement of novel insertion electrodes to match suitable capacitive electrodes is urgently required to develop NICs, which can occupy a unique sector in the secondary energy storage market.

SIBs that utilize Mn-rich cathodes (based on $Na_xMnO_2$) can meet the criteria of high energy output and low cost; however, reliance on the $Mn^{3+}/Mn^{4+}$ redox is associated with poor cycle stability due

to Jahn-Teller induced distortion from the $Mn^{3+}$ ion. This issue can be mitigated by partially substituting Mn with Mg. With this in mind, we systematically assessed the performance of layered P2-$Na_{2/3}Mn_{1-y}Mg_yO_2$ at y = 0, 0.05, and 0.1 synthesized using a modified Pechini method. In the interest of maximizing the energy density of the material, we used high upper cut-off voltages of 4.5 V, 4.6 V, and 4.7 V *vs* $Na/Na^+$, which is typically not explored in the literature. $Na_{2/3}Mn_{0.95}Mg_{0.05}O_2$ displayed a similar initial discharge capacity to $Na_{2/3}MnO_2$ with significant improvements in cycle retention. It was most promising when cycled between 2 – 4.5 V, retaining 140 mAh $g^{-1}$ (82% retention) and 116 mAh $g^{-1}$ (68% retention) after 50 and 100 cycles respectively at low current. A higher Mg dopant quantity led to improvements in cyclability and rate performance albeit with lower initial discharge capacity. Electrochemical and physical (*ex-situ* XRD) characterization was used to delineate the role of high-voltage phase transitions, SEI layer formation, electrolyte solvent insertion into sodium slabs, and active material degradation/dissolution toward capacity loss. Overall the high capacity, stability, and environmentally benign composition of the P2-$Na_{2/3}Mn_{1-y}Mg_yO_2$ cathode is promising for the development of SIBs.

In my second contribution, I synthesized and assessed $Na_2CoPO_4F$ (NCPF) as an insertion anode for NICs for the first time with commercial activated carbon (AC) as the capacitive cathode. The constructed NCPF//AC NIC exhibited exceptional rate performance, retaining 78% of its energy density (corresponding to 24 Wh $kg^{-1}$) when the power density was ramped from 125 to 5000 W $kg^{-1}$. In addition, its long-term stability when cycled from 0 – 3 V is among the highest reported in the literature, retaining 93% of its energy density (24 Wh $kg^{-1}$) after 100,000 cycles at 1 kW $kg^{-1}$. Furthermore, at an elevated voltage range of 0–3.25 V, the NIC retained 80% of its

energy density (26 Wh $kg^{-1}$) after 30,000 cycles at 375 W $kg^{-1}$. The performance is ascribed to the kinetic compatibility between the adsorptive cathode and pseudocapacitive anode, where pseudocapacitance is enhanced by the nanosized morphology on the surface of NCPF. The NIC system reported herein demonstrates supercapacitor-type benchmarks while also possessing a higher energy density.

Lastly, I tested alucone and titanicone organometallic coatings on P2-$Na_{2/3}Ni_{0.23}Mn_{2/3}Cu_{0.1}O_2$ SIB electrodes to improve the cycle stability. When cycled from 2 – 4.5 V *vs* $Na/Na^+$ at low current, the coatings demonstrated evidence of suppressing electrolyte decomposition; however, they did not improve the overall cycle stability. At this voltage range, degradation was predominated by the irreversible P2-O2 phase transition (onset ~4.22 V). However, the suppressed electrolyte decomposition resulted in improved rate performances of the coated samples. Alucone was less electronically conductive and thus less electrolyte-reactive than titanicone. At elevated currents from 2 – 4.5 V, electrolyte decomposition and the high-voltage P2-O2 phase transition were kinetically suppressed, and thus stability was predominated by particle cracking, surface exfoliation, and fractured connectivity. Here, the coatings substantially improved the cycle retention by maintaining the overall integrity of the electrode. After 500 cycles, the pristine electrode decayed entirely, suggesting significant losses of interconnectivity between the active particles, carbonaceous matrix, and current collector, while the electrodes coated with alucone and titanicone retained 81% and 70% capacity respectively. When cycled from 1.5 – 4.1 V *vs* $Na/Na^+$ at low current, the P2-O2 phase transition was avoided while the $Mn^{3+}/Mn^{4+}$ became active. In this scenario, the coatings significantly improved cycle retention by suppressing Mn dissolution.

## Acknowledgements

Financial support from the Natural Sciences and Engineering Research Council of Canada (NSERC), the University of Waterloo, and Henan Normal University is acknowledged. The work presented here was supported by the 111 Project (No. D17007). Tyler Or was personally supported through the NSERC Canada Graduate Scholarships – Master's Program and the Waterloo Engineering Excellence Master's Fellowship. Valuable mentorship from Dr. Karthikeyan Kaliyappan and Prof. Zhongwei Chen is gratefully acknowledged.

## Table of Contents

## List of Figures

## List of Tables

## List of Abbreviations

AC – Activated carbon

Alu-5C – Alucone coating using five MLD cycles

Alu-10C – Alucone coating using ten MLD cycles

Tit-5C – Titanicone coating using five MLD cycles

Tit-10C – Titanicone coating using ten MLD cycles

ALD – Atomic layer deposition

BET – Brunauer-Emmett-Teller

$C_{dl}$ – Double-layer capacitance (EIS parameter)

CEI – Cathode-electrolyte interface

CPE – Constant phase element (EIS parameter)

CV – Cyclic voltammetry

EDLC – Electric double-layer capacitor

EDX – Energy dispersive x-ray spectroscopy

EIS – Electrochemical impedance spectroscopy

EV – Electric vehicle

GITT – Galvanostatic intermittent titration technique

HIC – Hybrid-ion capacitor

ICP-AES – Inductively coupled plasma atomic emission spectroscopy

LIB – Lithium-ion battery

LIC – Lithium-ion capacitor

mA $g^{-1}$ – Milliamp per gram

mAh $g^{-1}$ – Milliamp hours per gram

LFP – $LiFePO_4$ LIB cathode

LMO – $Li_2Mn_2O_4$ LIB cathode

MLD – Molecular layer deposition

NCA – LIB cathode of form $LiNi_{0.8}Co_{0.15}Al_{0.05}O_2$

NCP – Sodium-ion cathode composition of $NaCoPO_4$

NCPF – Sodium-ion cathode composition of $Na_2CoPO_4F$

NIC – Na-ion capacitor

nm – Nanometer

NMC – LIB cathode of form $LiNi_xMn_yCo_zO_2$

PEG – Poly(ethylene glycol)

$R_{ct}$ – Charge-transfer resistance (EIS parameter)

$R_f$ – Resistance of $Na^+$ diffusion through the SEI layer (EIS parameter)

$R_S$ – Bulk series resistance (EIS parameter)

$R_{sei}$ – Resistance of Na+ diffusion through a surface film

SEI – Solid-electrolyte interface

SEM – Scanning electron microscopy

SHE – Standard hydrogen electrode

SIB – Sodium-ion battery

TGA – Thermogravimetric analysis

USGS – United States Geological Survey

V – Voltage

Wh $kg^{-1}$ – Watt hours per kilogram

W $kg^{-1}$ – Watts per kilogram

XPS – X-ray photoelectron spectroscopy

XRD – X-ray diffraction

$Z_W$ – Warburg element (EIS parameter)

## List of Symbols

ºC – Degrees Celsius

Å – Angstrom

μm – Micrometer

Z' – Real resistance (EIS)

Z'' – Imaginary resistance (EIS)

**Ω** – Ohm

F – Farad

eV – Electron volt

*d* – Lattice interlayer distance

**λ** – Wavelength

$\theta$ – Angle

$n_m$ – Number of moles (GITT)

$V_m$ – Molar volume (GITT)

S – Electrode surface area (GITT)

$\Delta E_s$ – Steady state voltage change from the constant current pulse (GITT)

$\Delta E_t$ – Voltage change from the constant current pulse (GITT)

$\tau$ – Time of current pulse (s) (GITT)

## 1. Introduction

Rapid increases in global energy demand necessitates technological advancements in clean energy storage. Current energy generation relies on fossil fuels, which are inherently finite, limited in geographic distribution, and release greenhouse gases into the atmosphere during conversion. Although renewable energy technologies (*e.g.,* wind, solar, and geothermal) show promise, their energy output is intermittent and thus requires energy storage solutions to generate an uninterrupted power supply system. Lithium-ion batteries (LIBs) are currently the most popular energy storage technology for mobile devices (cell phones, laptops, wireless earphones, *etc*.) and plug-in electric vehicles (EVs) due to their unmatched combination of energy density (150-200 Wh $kg^{-1}$, normalized by device mass), power density (>300 W $kg^{-1}$), and cycle stability (~2000 cycles). Demand for LIB production is correlated with the recent and skyrocketing growth of the EV market (Figure 1A). The International Energy Agency estimates based on current and expected policies that global EV sales could reach 4 million in 2020 and 21.5 million by 2030, corresponding to a ~24% yearly sales growth and a stock value of $13 and $130 million respectively.[1] Avicenne Energy estimated that EVs dominated the energy output of LIBs in 2017, more than doubling the usage from portable electronics (Figure 1C). [2] This is projected to further increase (+31.6%) by 2025.

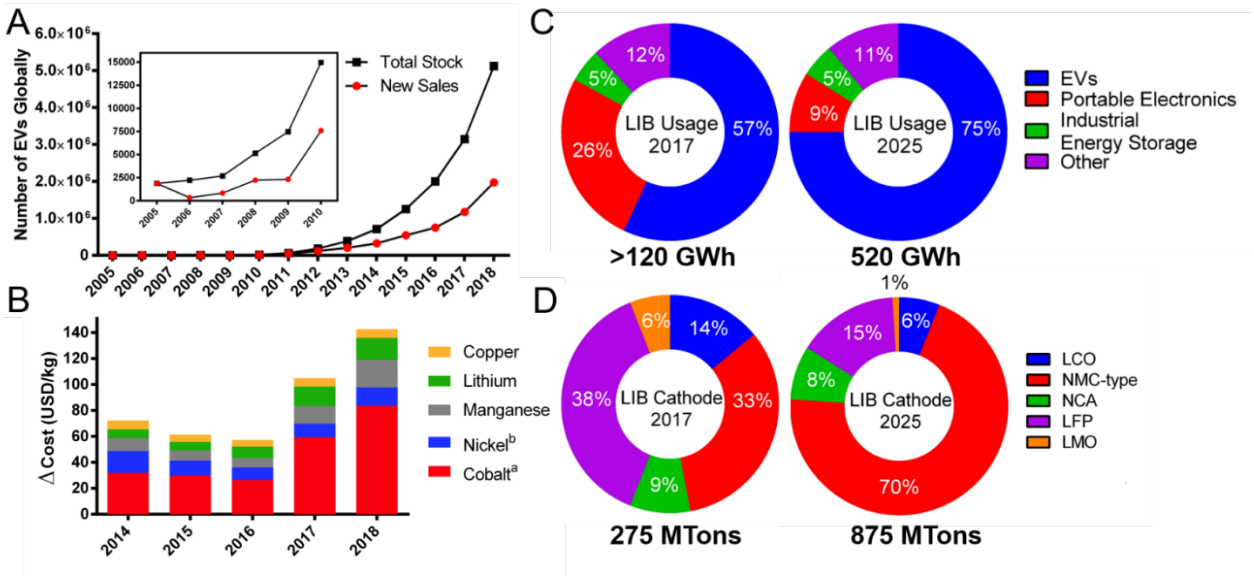


**Figure 1.** A) Global new EV sales to date B) Price (represented in bar size) of valuable metals used in LIBs in 2018 from the U.S. Geological Survey. Projection of LIB market share based on C) application and D) cathode composition. Projection assumes that Tesla, Inc. remains the only major EV manufacture to adopt NCA cells in 2025. Reprinted with permission from Wiley 2020.[3]

The United States Geological Survey (USGS) estimates that 39% of all lithium produced is used in primary and secondary lithium-based batteries.[4] Thus, large-scale and widespread applications for LIBs has arisen concerns for long-term availability of raw lithium reserves. The consensus regarding suggests that although the exact quantity of recoverable global lithium reserves is uncertain, they should be able to meet long-term projected demands (up to 2100).[5–7] However, the uneven geographic distribution of the reserves can cause price spikes for raw lithium materials. For instance, cumulative lithium demands in China may exceed the country's lithium reserves around 2028.[8] In addition, global demands for lithium could surpass production by 2050.[9,10] These concerns have motivated research toward sodium-ion batteries (SIBs), which as the name suggests utilizes $Na^+$ instead of $Li^+$ as the charge carrier. SIB development is promising due to the similar theoretical energy density and chemistry to LIBs. The various synthesis approaches and coatings developed for LIB cathodes often translate directly so SIB cathodes. SIB development may be

particularly attractive for grid storage applications, where volumetric and gravimetric energy density are relatively unimportant while material cost is critical.

## 1.1. Thesis Organization

This thesis comprises seven sections. **Section 1** introduces the reader to the general motivation in developing sodium-ion energy storage technologies. **Section 2** introduces fundamental background with respect to metal-ion energy storage. As electrodes for LIBs are closely related to SIBs, they are also reviewed in this section. An emphasis is then placed on layered sodium-ion cathodes and methods to improve their stability at high upper cut-off voltages. The concept and motivation of developing hybrid-ion capacitors is also introduced. **Section 3** details the theory and mechanism of the characterization techniques used in this thesis. **Section 4** investigates a layered sodium-ion cathode cycled at ambitiously high upper cut-off voltages. The failure mechanisms that inhibit cycle stability are characterized and explained in detail. **Section 5** investigates a novel orthorhombic insertion electrode material that was applied as an anode for a hybrid sodium-ion capacitor. When paired with capacitive activated carbon as the cathode, the fabricated sodium-ion capacitor delivered an ultrahigh cycle stability and rate performance. **Section 6** continues the investigation of layered sodium-ion cathodes cycled at high cut-off voltages. Alucone and titanicone deposited by molecular layer deposition were coated on the electrodes to determine whether they could extend the cycle stability. Finally, the conclusions and future research directions with respect to these projects are discussed in **Section 7.**

## 2. Background and Historical Context

### 2.1. Secondary Battery Technology

Secondary (rechargeable) batteries deliver/store energy from electrochemical reactions. They comprise multiple cells connected in series and parallel to generate the desired voltage output and capacity respectively. The principal components of a cell are: a) the anode, which is oxidized and liberates electrons that travel through an external circuit, b) the cathode, which is reduced and accepts electrons, c) the electrolyte, which facilitates the transfer of electrons between the electrodes through the diffusion of ions, and d) an electronically insulating separator that prevents an electrical short-circuit between the electrodes while also being permeable to ion diffusion (Figure 2). It is worth mentioning that a solid-state battery (emerging technology) may utilize a ceramic electrolyte that can facilitate ion transport and simultaneously serve as the separator.[11] In a secondary battery, the electrochemical reactions are reversible and thus the anode/cathode designations are reversed during charge/discharge (Figure 2). The cathode and anode designated during discharge are often referred to as such, or more precisely known as the positive and negative electrode respectively.

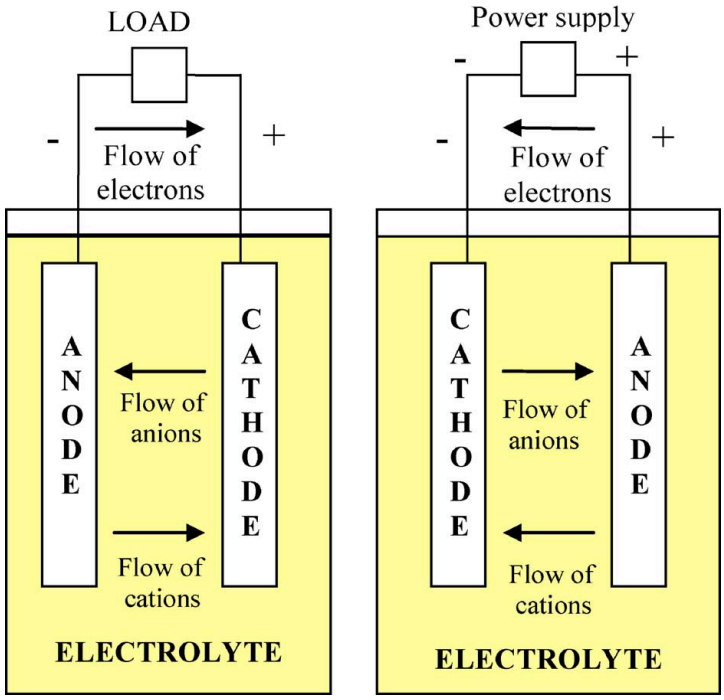


**Figure 2.** Principal components of a secondary cell. Reprinted with permission from Elsevier, 2009.[12]

The lead-acid (Pb-acid) is the earliest known secondary battery that was invented in 1859 by French physicist Gaston Planté. Although this battery has outdated electrochemical performance, it currently still has high commercial relevance due to its ultra-low cost. The key disadvantage is the toxic composition of Pb and sulfuric acid, although governments worldwide have implemented effective collection and recycling infrastructure to address this. The cell electrochemical reactions are depicted below in Equations 1 – 3:

Anode: $Pb(s) + HSO_4^-(aq) \rightarrow PbSO_4(s) + H^+(aq) + 2\ e^-$ [1]

Cathode: $PbO_2(s) + HSO_4^-(aq) + 3H^+(aq) + 2\ e^- \rightarrow PbSO_4(s) + 2H_2O(l)$ [2]

Overall: $Pb(s) + PbO_2(s) + 2H_2SO_4(aq) \rightleftharpoons 2PbSO_4(s) + 2H_2O(l)$ [3]

Ni-Cd batteries demonstrate approximately double the energy density compared to Pb-acid batteries (Table 1). Due to the toxicity of Cd, they have been rapidly replaced by Ni-MH batteries since the 1990s. The reaction mechanism is depicted in Equations 4 – 6 below:

Anode: $Cd(s) + 2OH^-(aq) \rightarrow Cd(OH)_2(s) + 2e^-$ [4]

Cathode: $2NiO(OH)(s) + 2H_2O(l) + 2e^- \rightarrow 2Ni(OH)_2(s) + 2OH^-(aq)$ [5]

Overall: $Cd(s) + 2NiO(OH)(s) + 2H_2O(l) \rightleftharpoons Cd(OH)_2(s) + 2Ni(OH)_2(s)$ [6]

Ni-MH batteries display exceptional volumetric energy density (140 – 300 Wh $L^{-1}$) and power output compared to Ni-Cd. Thus, they have attracted interest for EV applications and are still relevant today in hybrid EVs. However, Ni-based batteries will continue to lose market share to LIBs, which display state-of-the-art electrochemical performance with continuously falling costs. The electrochemical reaction of Ni-MH batteries is depicted as:

Anode: $M^*H\ (s) + OH^-(aq) \rightarrow M^*(s) + H_2O(l) + e^-$

Cathode: $NiO(OH)(s) + H_2O(l) + e^- \rightarrow Ni(OH)_2(s) + OH^-(aq)$

Overall: $M^*H\ (s) + NiO(OH)(s) \rightleftharpoons M^*(s) + Ni(OH)_2(s)$

* M represents $AB_5$, where A is a rare earth mixture and B is a transition metal.

The low energy density of Ni-based batteries compared to LIBs is attributed to the low cell voltage (Table 1). However, this is necessary due to the low stability of the aqueous electrolyte, where water electrolysis thermodynamically occurs at a voltage window of 1.23 V. It is worth mentioning that Pb-acid batteries can operate at a higher voltage (2 V) due to the overpotentials of the oxygen/hydrogen evolution reaction.[13] The main degradation mechanism of Pb-acid and Ni-based batteries is the alternations of electrode shape and structure from constant stripping and deposition of the metal electrodes throughout extended charge-discharge cycles. Furthermore, limitations to the power density are attributed to the complex electrochemical reactions and deposition mechanisms, which inherently have relatively sluggish kinetics.[14,15] The trends for the secondary battery market indicate that Pb-acid batteries will continue to be relevant for low-energy/cost applications, while LIBs will dominate portable/mobile applications. Emerging technologies, such as lithium-sulfur and metal-air batteries display ultra-high energy storage potential, but are far from commercial realization due to their poor cycle stability and power output.[16]

**Table 1.** Summary of commercially relevant secondary battery technologies.[12]

| Battery Technology | Energy Density (Wh $kg^{-1}$) | Power Density (W $kg^{-1}$) | Typical Operating Voltage (V) | Typical Cycle Life (# cycles) | Applications |
|---|---|---|---|---|---|
| Pb-acid | 30 | 180 | 2 | 1200 – 1800 | Low-cost and low-energy requirements, vehicle ignition |
| Ni-Cd | 60 | 150 | 1.2 | 1500 – 3000 | Low cost portable electronics |
| Ni-MH | 80 | 300 | 1.2 | 1500 | Low cost portable electronics, hybrid EVs |
| LIB | 150 – 200 | >300 | 3.7 | 2000 | Portable and wearable electronics, EVs |

## 2.2. Operating Mechanism and Development of Lithium-Ion Batteries

Figure 3 below depicts the major components and operating mechanism of a conventional LIB cell, which is a more specific variant of Figure 2. The negative and positive electrode correspond to the anode and cathode respectively during discharge and are often referred to as such. The separator typically comprises porous poly(ethylene)/poly(propylene) plastic or glass fiber, which is an electrically insulating material that prevents an electrical short-circuit from contact between the electrodes, but is porous to allow ionic conductivity. The electrolyte is typically lithium hexafluorophosphate ($LiPF_6$) dissolved in a mixture of ethylene carbonate and either dimethyl carbonate, diethyl carbonate, or ethyl methyl carbonate. This organic solvent is chosen due to its high electrochemical stability, allowing the battery to operate at a higher voltage range. The operating principle relies on the intercalation and de-intercalation of Li-ions between the electrodes, where Li-ions can be reversibly inserted and removed from the host network. During charging, the positive electrode serves as a 'source' of lithium ions. A power source is applied to the battery in order to oxidize the transition metal oxide, resulting in the release of a Li-ion into the electrolyte (*i.e.,* de-intercalation) and simultaneously releasing an electron into the external

circuit. The electron combines with a Li-ion intercalated at the graphite-based negative electrode. During discharge, the reverse reaction occurs spontaneously, where an electron and Li-ion are simultaneously released from the negative electrode, and the electron released can be used to power a load. A variety of compositions for the positive electrode are commercially available, with the most common being lithium cobalt oxide ($LiCoO_2$), lithium iron phosphate ($LiFePO_4$), Li-NMC ($LiNi_{1/3}Mn_{1/3}Co_{1/3}O_2$), and Li-NCA ($LiNi_{0.8}Co_{0.15}Al_{0.05}O_2$). The various Li-ion batteries are referenced according to the positive electrode composition, as the positive electrode dictates the battery capacity and energy density, while the negative electrode is always a graphite-based material. These positive electrode materials have advantages and trade-offs with respect to energy density, power capabilities, cost, toxicity, safety, and stability

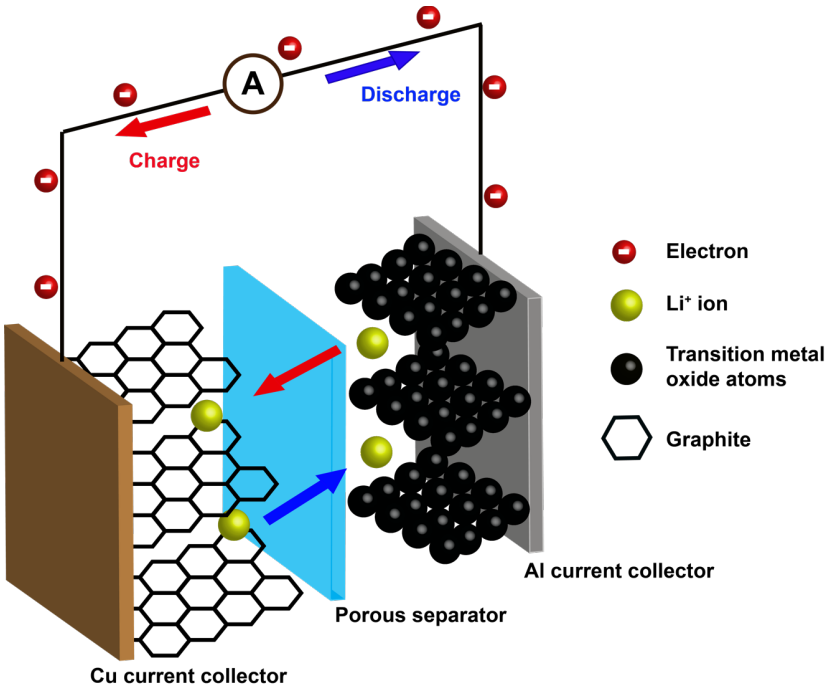


**Figure 3.** Components and operating mechanism of a lithium-ion battery. Reprinted with permission from Wiley, 2020.[3]

Anode: $Li_xC_6 \rightarrow C_6 + xLi^+ + xe^-$
Cathode: $Li_{1-x}CoO_2 + xLi^+ + xe^- \rightarrow LiCoO_2$
Overall: $Li_xC_6 + Li_{1-x}CoO_2 \rightleftharpoons C_6 + LiCoO_2$

$0 < x < 0.5$*

*For $LiCoO_2$, over-extraction leads to severe phase changes and cobalt dissolution from the generation of $Co^{4+}$

As the invention of the LIB was awarded the Nobel Prize in Chemistry in 2019, its historical development is worth discussing. The intercalation mechanism in LIBs was first discovered by Stanley Whittingham in 1972 based on a layered titanium disulfide host for lithium.[17] The concept was then formalized by Michel Armand in the late 1970s.[18] Lazzari and Scrostati subsequently demonstrated a proof-of-concept LIB using lithiated tunsgent dioxide and titanium disulfide as intercalation electrodes cycled between 1.6 and 2.2 V.[19] A seminal finding in 1980 from work by John Goodenough's research group discovered that lithiated transition metal oxides isostructural to $NaFeO_2$ could reversibly deintercalate and intercalate lithium ions.[20] This included $LiCoO_2$, which SONY used when they introduced the first commercial LIB in 1991 and is still prevalent as a cathode material today. However, LIBs could not be commercialized until a suitable negative electrode material was developed. At that time (1980s), companies including SONY, Exxon, Energizer, and Bell Laboratories used a lithium metal strip as the negative electrode, which caused safety concerns due to the growth of lithium dendrite during battery cycling, resulting in a short circuit that caused occasional and unpredictable cell explosions.[19] The discovery of graphite as an intercalation host material came as early as the 1980s from work by Rachid Yazami. However, early work on graphite ran into issues with the co-intercalation of solvent molecules, resulting in solvent reduction and structural degradation. Seminal contributions by Akira Yoshino and Jeff Dahn's research group involved the use of petroleum coke (calcined between 800 – 1600˚C), which can better resist solvent intercalation. Because Yoshino was the first to discover and report this finding in a seminal patent in 1985, he (along with Goodenough and Whittingham) is widely recognized as the inventor of the LIB.[21] $LiCoO_2$ and petroleum coke was used in the original

SONY product. However, using coke as the negative electrode resulted in a low specific capacity and energy (80 Wh $kg^{-1}$), so the next development was the use of hard carbon (120 Wh $kg^{-1}$). Later on, mesophase carbon microbeads (MCMB, 155 Wh $kg^{-1}$) were used as the negative electrode, which was formed by calcining petroleum pitch at 400˚C, resulting in the formation of spherical particles, which are extracted and re-calcined at ~2600˚C to improve graphitization.

## 2.3. Electrodes for Lithium-Ion Batteries

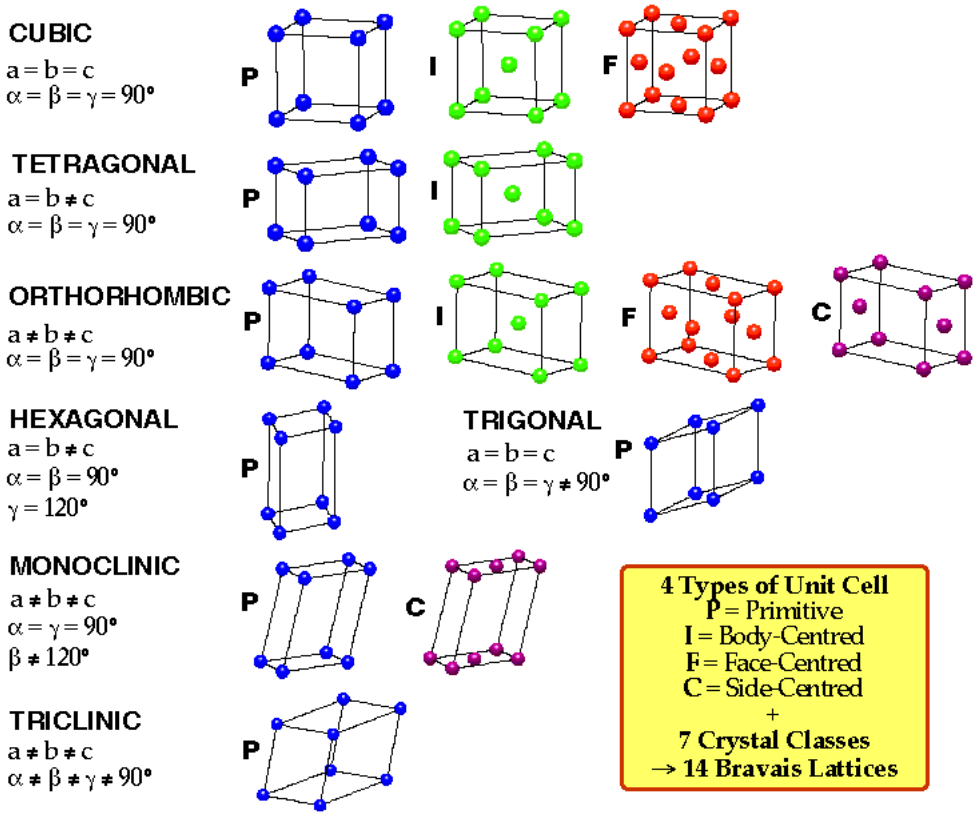


**Figure 4.** General crystal lattice geometries.[22]

LIB cathodes are often broadly classified into three main structural categories: layered, spinel, and olivine type, which comprise the most commercially relevant materials today.

### 2.3.1. Layered Cathodes

Layered cathodes are typically visualized as alternating slab layers comprising $Li^+$ and transition metal oxides (Figure 5). As such, $Li^+$ has a 2D solid-state diffusion path for (de)intercalation. The basic layered compounds include: $LiCoO_2$, $LiNiO_2$, $LiCrO_2$, $Li_2MoO_3$, and $Li_{0.7}MnO_2$. They possess a rhombohedral unit cell structure (Figure 4) with symmetry of the hexagonal space group $R\overline{3}_m$. The $Li^+$ and transition metal ions occupy octahedral sites while $O^{2-}$ forms planar sheets in between. Layered compounds may comprise more than one transition metal. As such, mixed-metal compositions can be viewed as a partial substitution of transition metals (*e.g.,* metal dopant) or a solid solution product. For instance, $LiNi_{0.5}Co_{0.5}O_2$ is a solid solution of $LiCoO_2$, and $LiNiO_2$. Layered cathodes comprise the most commercially relevant materials, dating back to the first LIB introduced by SONY in 1991 based on $LiCoO_2$. $LiCoO_2$-based batteries are still prevalent today for portable electronics due to the technological maturity, although the market share is rapidly shifting toward $LiNi_{1/3}Mn_{1/3}Co_{1/3}O_2$ as it is widespread in EV applications (Figure 1).

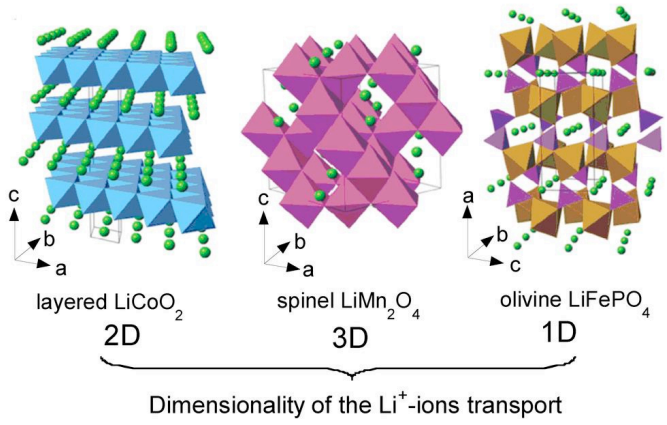


**Figure 5.** Structure and $Li^+$ diffusion pathway of layered, spinel, and olivine LIB cathodes. Reprinted with permission from Elsevier, 2015.[23]

### 2.3.2. Spinel Cathodes

The spinel group refers to a class of minerals that display a chemical formula of form $AB_2X_4$ (A, B = cations, X = anions). The cations reside in octahedral and tetrahedral sites while the anions display cubic close packing. As seen in Figure 5, the structure allows for 3D solid-state diffusion pathways for $Li^+$, resulting in high LIB rate performances. The most relevant cathode material is $LiMn_2O_4$, comprising a 1:1 mixture of $Mn^{3+}$ and $Mn^{4+}$ (denoted $Mn^{+3.5}$). It is worth mentioning that layered $LiMnO_2$ is unstable after electrochemical cycling and transforms into the spinel structure. Although the high rate performance of $LiMn_2O_4$ makes it ideal for application such as power tools, its main setback is the low practical capacity and cycle stability. This is caused by the presence of $Mn^{3+}$, which due to its electronic configuration ($t_{2g}^3$-$e_g^1$) can induce Jahn-Teller distortion.[24] The Jahn-Teller distortion of $Mn^{3+}$ can cause lattice changes from the cubic to tetragonal phase, which increases the resistance for $Li^+$ diffusion. The distortion is more pronounced when discharging at high rates as $Li^+$ is more concentrated at the surface of the $LiMn_2O_4$ particles, which leads to more pronounced distortion and causes particle cracking and disconnection.[25] Moreover, $Mn^{3+}$ is unstable and generates soluble $Mn^{2+}$ based on the disproportionation reaction: $2Mn^{3+}(solid) \rightarrow Mn^{4+}(solid) + Mn^{2+}(solution)$. Suppression of Jahn-Teller distortion has commonly been addressed by partially substituting Mn with other cations to reduce the amount of $Mn^{3+}$ and thus increase the average valence state of Mn.[26–28] Various coatings have also been explored to alleviate the dissolution of Mn.[29]

### 2.3.3. Olivine Cathodes

Olivine minerals possess a chemical formula of $M_2SiO_4$ where M = Ca, Fe, Mn, Ni, or Mg. The most relevant olivine cathode is $LiFePO_4$, which has generated significant interest due to its cheap and abundant composition, and high thermal stability and safety associated with strong Fe-P-O

bonds. This restricts the evolution of $O_2$ at high temperatures and limits thermal runaway. However, the main bottleneck toward application in EVs is the high cost relative to its energy density.[30] Although $LiFePO_4$ is known to have high electrochemical stability over a ~100% depth of discharge and a flat charge/discharge profile, thus allowing the practical capacity to approach the theoretical one, the low energy density is attributed to the low nominal voltage (3.3 V *vs* graphite anode).[23] The lower energy density of $LiFePO_4$ compared to commercial layered cathodes limits the driving range of EVs. Furthermore, although the material composition of $LiFePO_4$ is cheap, the high cost is associated with the complexity of the carbon-coated nanoparticle synthesis.[31] Synthesizing this morphology is necessary as $LiFePO_4$ displays poor intrinsic electronic and ionic conductivity. The poor electronic conductivity is due to the localized positions of $Fe^{2+}$ and $Fe^{3+}$ ($LiFePO_4/FePO_4$). As seen in Figure 5, $Li^+$ can only diffuse in 1D along the *b*-axis formed by edge-shared $LiO_6$ octahedra. The nanoparticle morphology improves electrical conductivity by improving interparticle contact and also reducing the electron transport path and tunneling barrier between the particle surface and core. Meanwhile, the conductive carbon coating (amorphous and permeable to $Li^+$) ensures electrical percolation. The nanoparticle morphology also reduces the solid-state diffusion path for $Li^+$. Lowered costs of LFP through maturity and economies of scale can help expand its applicability.

### 2.3.4. Comparison among Commercial Lithium-Ion Battery Cathodes

Table 1 below compares the performance and practical applications of current commercially relevant LIB cathodes.

**Table 1.** Comparison of most common commercially available LIBs. Gravimetric and volumetric capacity normalized based on cathode active materials.[19,23,32]

| Cathode Material | Nominal Voltage (V) | Typical Gravimetric Capacity (mAh $g^{-1}$) | Typical Volumetric Capacity (mAh $cm^{-3}$) | Comments |
|---|---|---|---|---|
| $LiCoO_2$ | 3.6 | 145 | 550 | Co is toxic and expensive.<br>Typical use: portable electronic devices<br>Cost: Medium<br>Lifetime: Medium |
| $LiMn_2O_4$ | 4.0 | 120 | 496 | Mn abundant and environmentally friendly.<br>Typical use: High-power tools and e-bikes<br>Cost: Low<br>Lifetime: Low |
| $LiNi_{1/3}Mn_{1/3}Co_{1/3}O_2$ | 3.7 | 170 | 600 | Designed to reduce Co content and combine advantages of Ni and Mn<br>Typical use: Portable electronic devices and EVs<br>Cost: High<br>Lifetime: High |
| $LiFePO_4$ | 3.3 | 165 | 589 | Fe abundant and environmentally benign, high thermal stability<br>Typical use: Power tools and e-bikes<br>Cost: Medium<br>Lifetime: High |
| $LiNi_{0.8}Co_{0.15}Al_{0.05}O_2$ | 3.7 | 200 | 700 | Highest specific energy density, used in Panasonic batteries for Tesla EVs<br>Cost: High<br>Lifetime: Medium |
| $Li_4TiS_2$ | 1.9 | 210 | 697 | Highly stable and safe<br>Cost: Very high<br>Lifetime: Very high |

### 2.3.5. Anodes

In the early stages of LIB research, Li metal strips were used as the anode. Due to the uneven stripping/deposition of Li throughout cycling, this anode had poor stability and even formed dendrites that extended toward the cathode, resulting in a short circuit. Today, commercial cells utilize a graphite-based anode, which is highly safe and stable. However, there is ongoing research

to stabilize the Li metal anode for practical applications due to its ultra-high theoretical capacity (3860 mAh $g^{-1}$).[33] Natural graphite was originally tested as a LIB anode. However, it displayed low rate performance due to the high anisotropy of the graphite flakes – the flakes had a short dimension along the *c*-axis, which was often laid orthogonal to the current collector. As there was high electronic resistance along the *c*-axis, the orientation of the flakes led to sluggish $Li^+$ intercalation. This issue was addressed by milling the graphite thoroughly to produce small flakes that were randomly oriented. However, natural graphite was not compatible with propylene carbonate electrolyte as it would intercalate into graphite and degrade the structure. Commercial LIBs utilize synthetic graphite, derived by calcining (graphitizing) various carbon sources (*e.g.,* petroleum residua). Graphitized mesocarbon microbeads (MCMB) is the typical benchmark anode material.

## 2.4. Sodium-Ion Batteries

Sodium-ion batteries (SIBs) are an emerging technology that have been proposed as an alternative to LIBs due to the low cost and abundance of sodium. Although the quantity of lithium reserves is unknown and projections for the global production capacity are varied, is generally agreed upon that the lithium supply chain will be constrained if electric mobility and electrical grid storage reach the mass market.[5,9,10] Sodium is an obvious replacement for lithium due to the similar chemical properties – the operating mechanism and chemistry of SIBs is nearly identical to LIBs, so a significant amount of research from LIBs is directly translatable toward SIBs. In fact, SIBs were studied during the early days of LIB development, but work was discontinued due to the poor performances.[34] The use of $Na^+$ as the charge carrier has the following consequences toward battery performance: 1) The energy density of SIBs is inherently limited because of the higher

standard electrode potential (-2.71 V *vs* SHE) and mass of sodium compared to lithium (-3.02 V *vs* SHE). In addition, sodium cathodes tend to have a lower intercalation potential (*i.e.,* less favorable) compared to their lithium analogues, resulting in lower output voltages.[35] 2) Most importantly, $Na^+$ has a larger ionic radius (1.02 Å) compared to $Li^+$ (0.76 Å), which limits the intercalation capabilities, solid-state diffusion, and host lattice stability over repeated intercalation/deintercalation cycles of $Na^+$.[36] Thus, to fully realize the potential of SIBs in large-scale storage, cathode materials comprised of low-cost, abundant, and nontoxic materials that can deliver high energy and power output are required.

Compared to cathodes, less research has been devoted toward anodes. A key distinguishing feature from LIBs and outstanding technical challenge is that conventional graphite cannot intercalate $Na^+$ due to its insufficient interlayer space distance ($d$(002) = 0.334 nm). Seminal work from Wen *et al.* demonstrated that an expanded interlayer space ($d$(002) = 0.43 nm), prepared by the oxidation and partial reduction of graphite, could reversibly intercalate $Na^+$.[37] It is believed that a minimum interlayer distance of 0.37 nm is necessary to intercalate $Na^+$.[38] On the other hand, disordered carbons (e.g., hard, soft, or amorphous carbon), which do not display long-ranged ordering along the $z$-axis can intercalate $Na^+$ reversibly (below 0.1 V *vs* $Na/Na^+$) and are more commonly used as anode materials. The structure of hard carbon is shown in Figure 6, which comprises randomly oriented graphitic domains (few-layered graphene sheets) surrounded by amorphous regions. Charge-storage occurs through surface adsorption, pore-filling, and defect binding in the amorphous regions in addition to intercalation.[39] The reversible capacity is dependent on the particle size (degree of graphitization), porosity, and electrolyte composition.

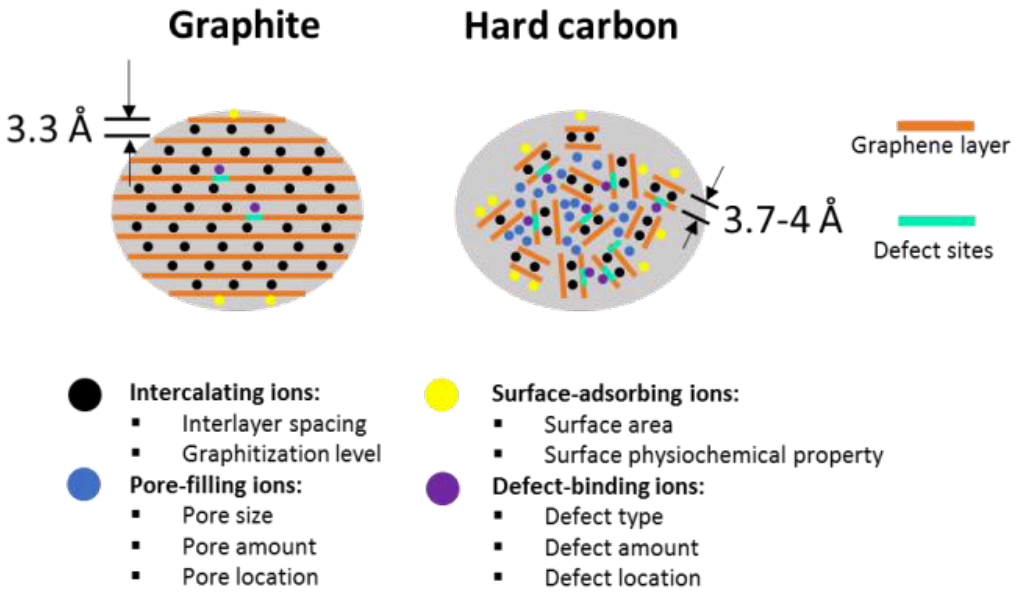


**Figure 6.** Structure and ion storage mechanism comparison of graphite and hard carbon. Reprinted with permission from Wiley, 2018.[39]

With respect to cell components, SIBs can use aluminum instead of copper as the current collector, as $Na^+$ does not alloy with aluminum. This can marginally lower the material cost.

## 2.5. High-Voltage Cathodes for Sodium-Ion Batteries

The development of cathodes that can be cycled at high cut-off voltages is critical toward fabricating high energy density SIBs. High voltage cycling enables enhanced capacity utilization (*i.e.,* higher depth of discharge) and increases the average operating voltage. As discussed in the previous section, SIB cathodes generally demonstrate a low average operating voltage compared to LIBs. For instance, cathodes reliant on Mn redox ($Na_xMnO_2$ and derivatives) display an average operating voltage < 3 V *vs* $Na/Na^+$.[40] In addition the charge/discharge curves typically have a sloping profile due to the poor $Na^+$ diffusion kinetics and complex structural/cation rearrangements. SIB cathodes that demonstrate high operating voltage (> 4 V *vs* $Na/Na^+$) typically

consist of sodium-ion phosphate and fluorophosphate materials (*e.g.,* $NaFePO_4$, $Na_3V_2(PO_4)_3$, $NaFePO_4F$, $Na_2CoPO_4F$, $Na_3V_2(PO_4)_2F_3$). The high operating voltage of these materials is ascribed to the inductive effect of the $PO_4^{3-}$ and $F^-$ anions. However, these materials demonstrate poor inherent electronic conductivity, thus often requiring a conductive coating and nanostructured morphology for adequate performance. These materials often demonstrate poor cycle retention due to significant structural evolution.

On the other hand, similar to LIB cathodes, sodium layered transition metal oxides $Na_xMO_2$ (M = One or more of Co, Fe, Ni, Ti, V, Cr, or Mn, $x$ = 0.5 – 1) often display the most optimal combination of energy density, cycle retention, and rate performance. They are often classified based on the Delmas notation – either O3 or P2-type, where the letter refers to $Na^+$ located in an octahedral (O) or prismatic (P) oxygen cage while the number refers to the repeat period of transition metal stacking (*i.e.,* number of distinguishable layers) in the unit cell (Figure 7).[41] In general, P2-type cathodes have a lower sodium content but are more structurally stable and resist phase changes during the charge/discharge process, thus resulting in a higher discharge capacity (when Na-metal foil used as counter electrode) and cycle stability. Furthermore, P2-type cathodes demonstrate favorable diffusion kinetics for $Na^+$ due to the preferred prismatic coordination of the relatively large $Na^+$ ions.[42] Although P2-type cathodes may possess a high theoretical capacity, they must be cycled at high voltage cut-offs ($V_{cut\text{-}off}$, >4.4 V *vs* $Na/Na^+$) in order to exploit this and maximize their energy density. However, extending $V_{cut\text{-}off}$ can severely compromise cathode cyclability due to irreversible phase and volume changes, active material degradation and dissolution, and uncontrolled electrolyte side reactions. Cathodes that demonstrate good cyclability at high $V_{cut\text{-}off}$ are scarce in the literature.

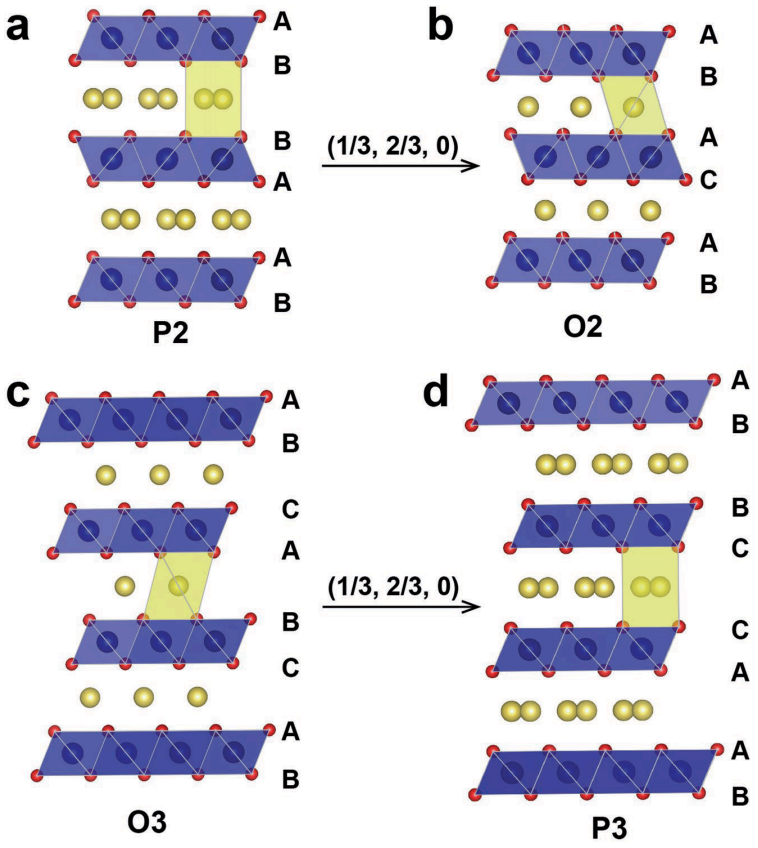


**Figure 7.** Schematic of various sodium layered structures classified by the Delmas notation. The yellow spheres represent $Na^+$ while the blue and red spheres represent the transition metal and oxide ions respectively. Reprinted with permission from Wiley, 2018.[43]

Layered cathodes cycled at high cut-off voltages typically decay due to the following failure mechanisms:[44]

1) *Irreversible structural transitions*. Extraction of $Na^+$ is often accompanied by $Na^+$/vacancy ordering and gliding of the transition metal oxide slabs. These phase changes can constrict $Na^+$ diffusion pathways and also cause volume changes leading to particle fracture. In a specific case, the high-voltage transitions of the P2 phase have been well studied. When $Na^+$ is extracted from large prismatic sites within the P2 phase with 'AB BA' stacking, adjacent transition metal oxide slabs repel electrostatically, which generally corresponds with an expansion of the *c*-axis lattice parameter and shrinking of the *a* parameter.[45] With further extraction, the process is also associated

with slab gliding for energetic balance, forming octahedral vacancies that shrink the interlayer spacing. The stacked-fault OP4 phase is an intermediate transition occurring ~3.5-3.6 V where every other prismatic layer is converted into an octahedral layer with 'AB BA CB BC' stacking. At ~4.2 – 4.3 V, the prismatic sites may convert entirely to octahedral sites, resulting in an O2 phase with 'ABC BAB' stacking. The formation of this phase is clearly observed in compositions such as P2-$Na_{2/3}Ni_{1/3}Mn_{2/3}O_2$.[45] The O2 phase transition is not as reversible as the OP4 transition and is a significant reason for capacity fade when cycling at high cut-off voltage ranges.

2) *Electrolyte oxidation*. The carbonate-based electrolyte has a thermodynamic electrochemical stability of ~4.2 V *vs* $Na/Na^+$, where oxidation at the cathode-electrolyte interface (CEI) and reduction at the anode-electrolyte interface (often referred to as the solid-electrolyte interface) will occur above this. Thus, excessive decomposition and formation of the CEI layer is expected at low-current cycling. Moreover, oxidized species in the active material (*e.g.,* $Fe^{4+}$ and $Ni^{4+}$) can accelerate electrolyte oxidation.

3) *Insertion of solvent molecules into the interlayer space*. Layered structures have a greater risk of solvent insertion at higher voltages due to the expansion of the interlayer space and $Na^+$ vacancy.

4) *Oxygen evolution*. In some cathodes, participation of oxide ions in the redox could occur at high voltages, which contributes to capacity although it is irreversible due to oxygen loss.[46] This causes significant structural rearrangements due to the oxide vacancies.

These issues must be addressed to pave the way toward the commercialization of SIBs.

## 2.6. Coatings for Improved SIB Cathode Performance

One of the earliest reports on the use of coatings in cathode materials was the conductive carbon coating on LFP nanoparticles as discussed in Section 2.3. The conductive coating provided extra

conduction pathways between active particles and the current collector, and also improved heterogeneous charge-transfer at the electrode-electrolyte interface. A variety of coatings were also tested early on to suppress Mn dissolution and phase changes that hindered the LMO cathode.[29] The first demonstration of a metal oxide coating was performed by Cho and Kim[47] where LMO was coated on LCO. The LMO coating improved the thermal stability of LCO and reduced the side-reactions between the electrode and electrolyte, resulting in improved cycle retention. Soon after, they applied an $Al_2O_3$ coating on LCO for the first time using a solution-based approach,[48] and continued their investigation by comparing the effects $ZrO_2$, $Al_2O_3$, $TiO_2$, and $B_2O_3$ coatings.[49] These coatings enhanced the cycle stability at a wider depth of discharge (2.75 – 4.4 V *vs* $Li/Li^+$), enabling greater capacity utilization (Figure 8). They observed that the coating suppressed the *c*-axis lattice expansion upon $Li^+$ extraction, and thus reasoned that the coating physically suppressed the high-voltage transition from the hexagonal to monoclinic phase. The strong performance of $ZrO_2$ over the other materials was ascribed to its high fracture toughness. However, this explanation was disputed by Chen and Dahn,[50] as their *in situ* XRD experiments did not provide evidence that metal oxide coatings could suppress phase changes. They instead proposed that the coatings mainly suppressed impedance growth on the surface of LCO. The impedance growth was associated with the use of $LiPF_6$ electrolyte.

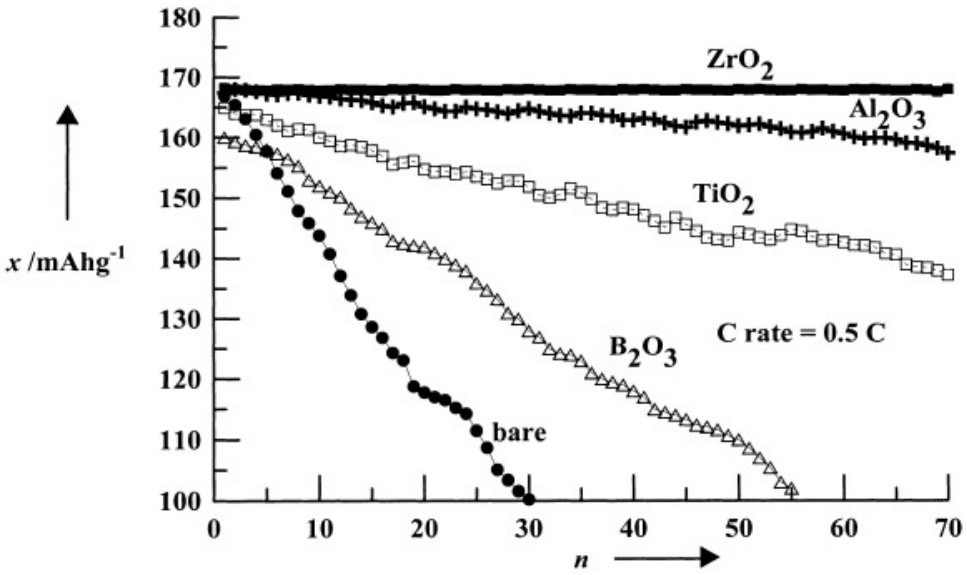


**Figure 8.** Stability of LCO coated with various ceramic coatings cycled from 2.75 – 4.4 V at 0.5 C. Reprinted with permission from Wiley, 2001.[49]

In general, cathode coatings can provide the following improvements: 1) generation of a percolated electronically conducting network on the surface of the particles, 2) surface modification to remove/cover undesirable surface functional groups, which can prevent harmful side reactions with moisture or air, 3) serving as a physical barrier from the electrolyte to suppress active material dissolution, oxygen evolution, or electrolyte oxidation at high voltages, and/or 4) serving as an HF scavenger. HF can cause significant corrosion/dissolution of the cathode active material. It is generated when $LiPF_6$ reacts with (unavoidable) trace quantities of water in the electrolyte according to Equations 7:

$$LiPF_6 + H_2O \rightarrow LiF + POF_3 + 2HF \quad [7]$$

Metal oxides (*e.g.,* $Al_2O_3$) can serve as a Lewis base and quench HF according to Equation 8:

$$Al_2O_3 + 6HF \rightarrow 2AlF_3 + 3H_2O \quad [8]$$

Thus, electrochemically inert metal oxide coatings often demonstrate improved cycle stability. However, they possess poor intrinsic electronic and ionic conductivity, which may introduce increased voltage polarization and thus losses in capacity and rate capability.

Coatings can be applied in several different ways. A rough coating is often employed, which involves a mechanical or solution-based mixing of the active material with the coating precursor followed by a sintering reaction. Although this technique is simple and scalable, the coating has relatively poor uniformity. Therefore, some particle regions may have thicker coatings while other regions are left exposed. Alternatively, atomic or chemical vapor deposition can be used to apply an ultrathin coating. This can produce highly uniform coatings with thickness control down to ~0.1 nm. Although minimum quantities of precursor are required, the technique requires lengthy reaction times and has poor scalability.[51] Atomic layer deposition will be discussed in-depth in the following section.

### 2.6.1. Atomic/Molecular Layer Deposition Coatings

Atomic layer deposition (ALD) is a thin film deposition technique that has garnered significant interest over the past decade. It involves a self-controlled binary reaction sequence where two precursors are sequentially pulsed and react with the surface of a substrate. Figure 9 below depicts a reactor schematic of the deposition of $TiO_2$ on a generic substrate. Here, the reactants are tetrakis(dimethylamido)titanium (Ti source) and water as the oxidizing precursor.

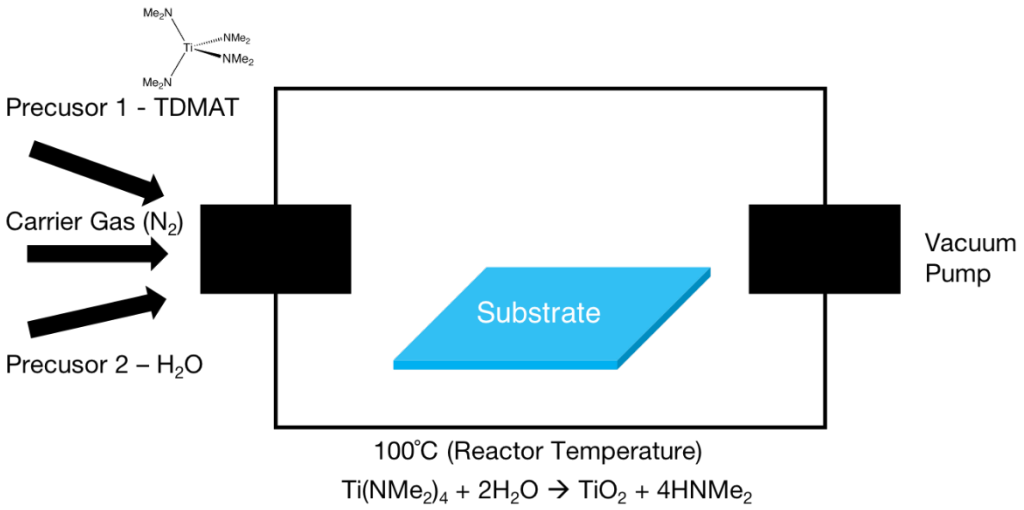


**Figure 9.** Schematic of the deposition of $TiO_2$ on a substrate with an ALD reactor.

As an extension of ALD, molecular layer deposition (MLD) utilizes an organic linker in place of the oxidizing precursor to generate an organometallic film. Figure 10 below depicts the deposition of alucone using trimethylaluminum and ethylene glycol as precursors, which was utilized in Section 6. Compared to ceramic films deposited by ALD, MLD films are more flexible and porous, allowing for improved ionic conductivity and mechanical robustness. This can be tuned by the size (carbon backbone) of the organic linker. MLD coatings are ideal for conversion-type electrodes (*e.g.,* silicon or sulfur), as the film can better accommodate the high volume changes throughout cycling. Films deposited by MLD have not been explored in the literature to a great extent.

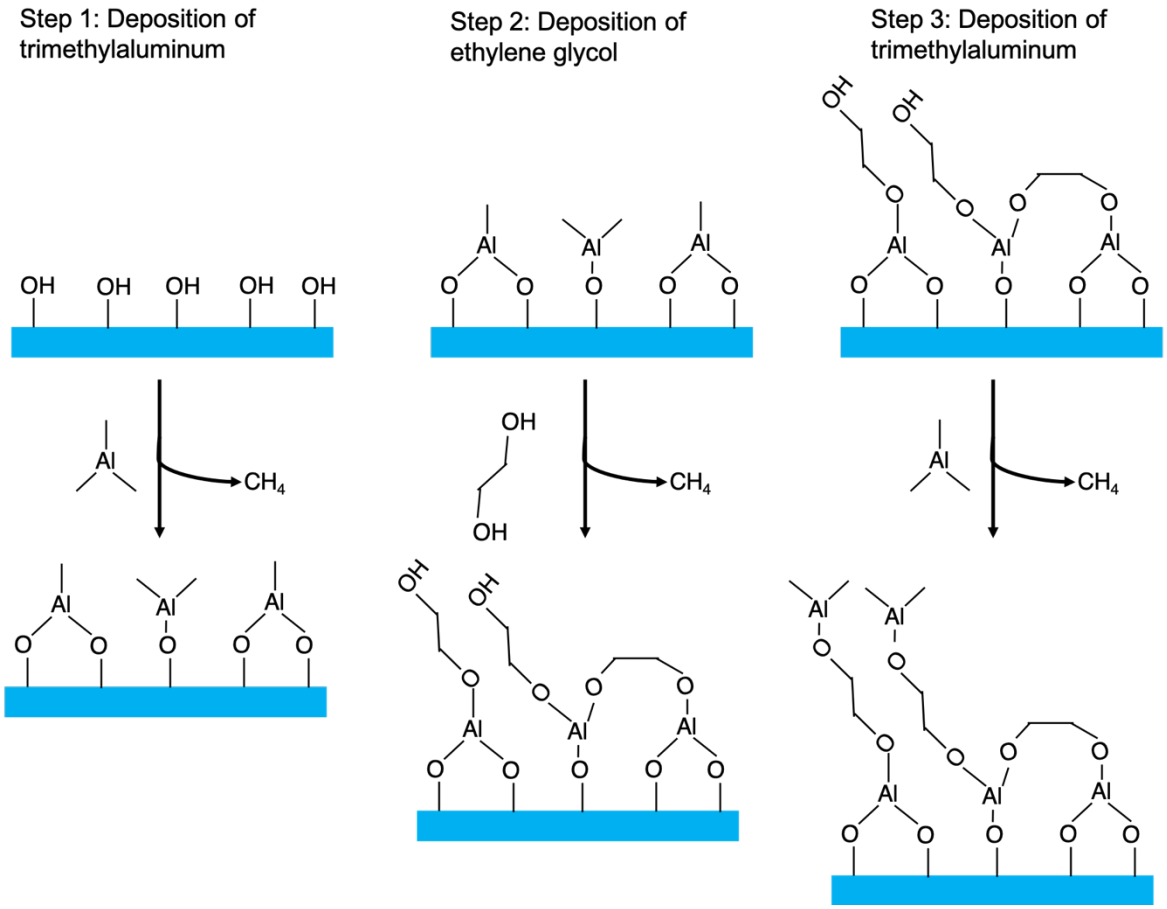


**Figure 10.** MLD (1.5 cycles) of alucone film using trimethylaluminum and ethylene glycol as precursors. Cycle is repeated to form an alucone film with the desired thickness.

## 2.7. Sodium-Ion Capacitors

Two major classes of secondary energy storage systems include LIBs and electric double-layer capacitors (EDLCs). While commercial LIBs possess an impressive combination of energy density (150-200 Wh $kg^{-1}$, normalized by device mass), power density (>300 W $kg^{-1}$), and cycle stability (~2000 cycles), their power density and cycle stability pales in comparison to EDLCs, which can reach up to 10 kW $kg^{-1}$ with stable capacity retention over millions of cycles.[52] This is due to the difference in charge storage mechanisms, where LIBs rely on the intercalation/deintercalation of $Li^+$ within the electrode crystal lattice, while EDLCs store charge based on the

adsorption/desorption of ions on the surface of a porous carbonaceous electrode that typically comprises activated carbon (AC). The intercalation/deintercalation charge storage mechanism can cause structural defects in the crystal lattice due to volumetric strain and is kinetically sluggish compared to physical adsorption/desorption. However, EDLCs have poor energy density (5-10 Wh $kg^{-1}$) as charge storage is restricted to the electrode surface, thus limiting their range of applications.[52]

On the other hand, hybrid-ion capacitors (HICs) are designed to bridge the features of metal-ion batteries and EDLCs.[53] Typically comprised of an insertion electrode and a carbonaceous capacitive electrode in an organic (carbonate-based) electrolyte, HICs can deliver 3-4 times the energy density compared of EDLCs albeit with lower rate performance (energy output at high current) and cycle stability.[53] HICs use either lithium or sodium-based salts as charge carriers, with these devices termed lithium-ion capacitors (LICs) and sodium-ion capacitors (NICs), respectively. The operating mechanism of the device relies on the intercalation/deintercalation of $Na^+$/$Li^+$ with the insertion electrode while the energy storage on the capacitive electrode relies on the formation of an electric double layer through the adsorption/desorption of counter-ions (*e.g.,* $ClO_4^-$ and $PF_6^-$) at the electrode-electrolyte interface.[54] The insertion electrode contributes to the HIC energy density as it can store charge through redox pseudocapacitive (surface) and intercalation (bulk) processes, while non-Faradaic processes on the carbonaceous electrode are responsible for delivering high power density. However, the main disadvantage of this system is the mismatched kinetics between the sluggish intercalation mechanism and the rapid capacitive charge storage. As a result, the energy density of HICs often decreases sharply at high power densities.[54] Thus, pseudocapacitive charge-storage contributions on the insertion anode are critical,

as they are kinetically facile and stable. With this in mind, it is clear that the design, preparation, and improvement of novel insertion electrodes to match suitable capacitive electrodes is urgently required to develop HICs, which can occupy a unique sector in the secondary energy storage market.

A large variety of insertion electrodes for HICs have been explored and developed in the literature, such as titania-based compounds,[55,56] carbonaceous electrodes,[57] and transition metal oxides used as intercalation cathodes in metal-ion batteries.[58–60] Some HIC systems reported recently demonstrate an impressive energy density (upper range of 60 – 80 Wh $kg^{-1}$, normalized by active material mass), narrowing the gap in energy storage capabilities with batteries.[53] However, the vast majority of HICs still display relatively poor cycle stability and rate capability. Cycle stability is a particularly important benchmark for HICs as their proposed applications (*e.g.,* regenerative breaking) are similar to that of supercapacitors.[53] However, while commercial supercapacitors are stable over millions of charge-discharge cycles, few reports in the literature on HICs demonstrate a capacity retention ≥90% over 10,000 cycles.[53]

## 3. Methods

### 3.1. Cathode Synthesis

The mixed hydroxide coprecipitation method is the most common synthesis approaches for layered transition metal oxides for both LIBs and SIBs that generally involves two steps: 1) precipitation of metals as a hydroxide precursor at high pH (eg, $Ni_{1/3}Mn_{1/3}Co_{1/3}(OH)_2$ for NMC cathode) and 2) solid-state reaction with a stoichiometric equivalent (5%-10% excess) of LiOH/NaOH or $Li_2CO_3/Na_2CO_3$.[61] The first step is typically performed under inert atmosphere ($N_2$) to avoid

oxidation and formation of metal oxides (especially for Mn). $NH_3$ is also added as a chelating agent to ensure that the metal ions are well dispersed to balance the rates of nucleation and crystal growth, which helps generate a homogeneous particle size and cation distribution for the hydroxide precursor, leading to improved electrochemical performance.[62]

In the sol-gel synthesis method for intercalation electrodes, metal ions are homogeneously dispersed in aqueous solution with the aid of chelating/gelling agents (often citric acid).[63] Weak bases such as ammonia or acetate are added to stabilize the pH and enhance metal cation binding to the chelate. Subsequent water evaporation forms a dense sol precursor to immobilize the metal ions, which is then calcined to decompose organics and induce crystallinity. A less commonly used derivation of the sol-gel synthesis is known as the modified Pechini method. In this technique, metallic ion reagents are uniformly dispersed in a dense poly(ethylene glycol) (PEG) matrix. Following sintering reactions, nanometer-sized particles with a uniform size distribution can potentially be generated.[64]

## 3.2. Battery Fabrication

After the cathode active material is synthesized, the powder is fabricated into an electrode and assembled in a CR2032 cell using sodium foil as the counter electrode (anode) for lab-scale electrochemical testing. In the work shown here, the electrode was fabricated by co-grinding the active powder with PTFE-acetylene black as the agglomeration agent (binder) and carbon black as a conductive agent. The electrode was then pressed onto a stainless steel mesh current collector. Cell fabrication was conducted in an argon-filled glove box to avoid side-reactions with moisture and oxygen (particularly with sodium metal). The electrolyte was 1 M $NaClO_4$ dissolved in 1:1

(v/v) ethylene carbonate: diethyl carbonate with 5 vol% fluoroethylene carbonate additive. Fluoroethylene carbonate is a common electrolyte additive for LIBs and SIBs as it assists with the formation of a thin and stable SEI film, resulting in reduced irreversible capacity and improved cycle performance.[65] A porous polypropylene separator is added between the anode and cathode – it is electrically insulating to prevent a short circuit while permeable to $Na^+$ diffusion.

## 3.3. Physical Characterization

### 3.3.1. X-Ray Diffraction

X-ray diffraction (XRD) is a fundamental technique to determine the identity of crystal lattices. The techniques relies on the scattering of incident X-ray photons on the crystal atom's electrons. Most scattered photons disappear through destructive interference. However, evenly-spaced lattice planes (ordered atoms) can induce constructive interference of diffracted photons at certain angles to produce an intense signal that can be detected. The constructive interference is characterized by Bragg's law: $2dsin\theta = n\lambda$, where *d* is the interlayer space between lattice planes, $\theta$ is the incident photon angle, and *n* is an integer (Figure 11). Diffraction peaks correspond to a lattice plane, which are represented by the Miller indices (*h, k, l*). The Miller indices are *derived* based on the three Cartesian coordinate intercepts of a lattice plane in a unit cell.

In battery research, XRD is critical toward assessing the synthesis method. For instance, all O3 or P2 layered structures should display identical diffraction patterns with some variations in peak position. In LIB cathode research, XRD is often used to assess the degree of intermixing between $Li^+$ and other transition metal ions (often $Li^+/Ni^{2+}$), which can lead to low reversible capacity. This is done by measuring the intensity ratio of the (*003*) and (*104*) diffraction peaks. However, this

cation mixing issue generally does not occur in SIB cathodes due to the larger size of $Na^+$. XRD is often used to monitor the evolution of the crystal lattice over electrochemical cycling – for instance the peak shifts can be observed that are associated with interlayer space (*d*) expansion along the *c*-axis upon $Na^+$ extraction. However, XRD does not provide detailed information on atomic arrangement and local environments, as it only indicates the average atomic ordering.

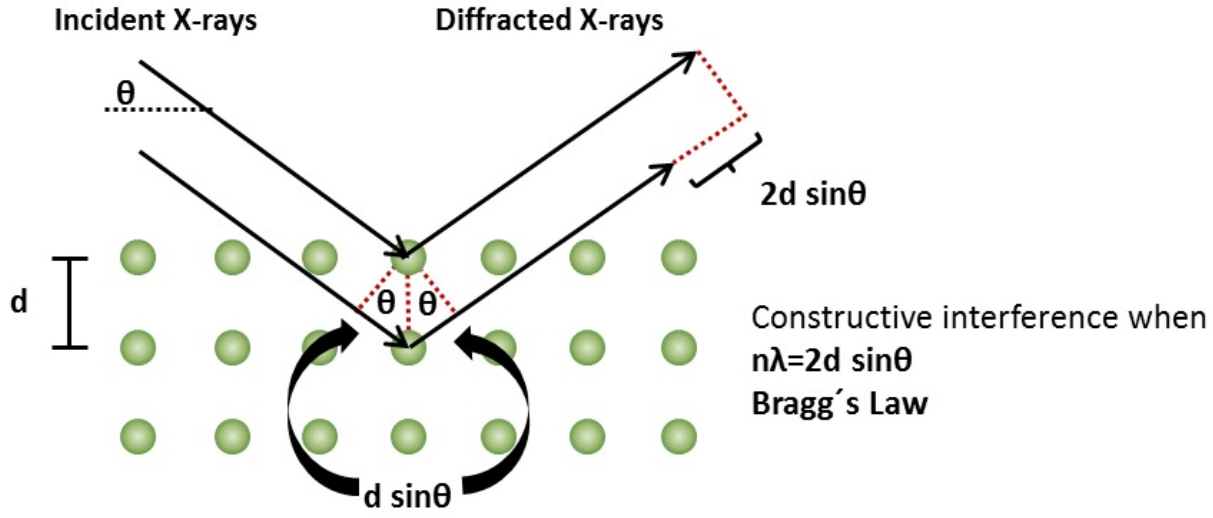


**Figure 11.** Constructive interference of diffracted X-ray photons on a lattice plane and relationship with Bragg's law.[66]

### 3.3.2. Scanning Electron Microscopy and Energy-Dispersive X-Ray Spectroscopy

Scanning electron microscopy (SEM) relies on the interaction between a focused beam of electrons bombarded on a sample surface (Figure 12), which can generate high-resolution images due to the small wavelength of the illumination source. Emissions from the sample-electron interactions are detected, with the most important involving secondary electrons, backscattered electrons, and characteristic X-rays. Secondary electrons are produced when the electron bombardment causes ionization of loosely-bound electrons (3 – 5 eV) on the sample surface.[67] This signal is primarily utilized to generate an image of the sample morphology. Secondary electrons can generate depth perception as electrons obstructed from reaching the detector will appear as a darker spot on the

image. Backscattered electrons originate from the incident electron beam that collides with atomic nuclei on the sample and scatter at high energies (> 50 eV). Thus, larger atoms will generate more scattering and a higher signal intensity. Images produced using backscattered electrons can produce excellent contrast between different elements. Finally, incident electrons can collide and eject inner shell electrons of the sample, resulting in relaxation of outer shell electrons to fill the hole. The relaxation energy loss is balanced by the emission of an X-ray photon of equivalent energy. As different elements produce characteristic X-ray emissions, this can be used to identify and quantify the relative ratio of certain elements. This microanalytical technique is known as energy-dispersive X-ray spectroscopy (EDX).

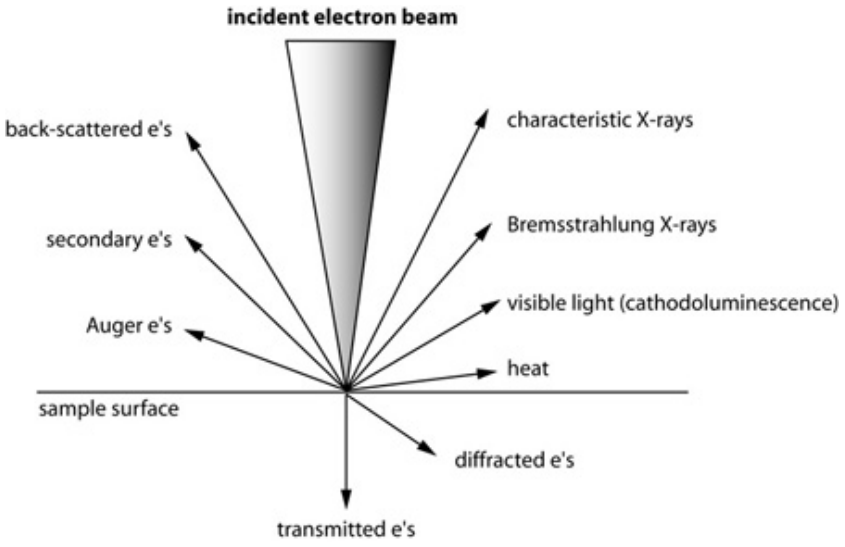


**Figure 12.** Sample-electron interactions.[68]

### 3.3.3. Thermogravimetric Analysis

Thermogravimetric analysis (TGA) precisely measures a sample's mass as a function of temperature in either a reactive or inert atmosphere. For battery applications, TGA can be used to assess the thermal stability of a cathode, for instance determining the onset temperature of oxygen

evolution. In this work, TGA was used to determine and quantify the presence of carbons on the active material, which begins to decompose at ~400˚C under air.

### 3.3.4. X-Ray Photoelectron Spectroscopy

X-ray photoelectron spectroscopy (XPS) is closely related to EDX that was discussed in Section 3.3.2. The technique relies on the complete transfer of energy from an X-ray photon to an inner shell electron, resulting in ionization. The kinetic energy (and quantity) of electrons is measured by a detector, and thus the electron binding energy can be calculated based on the fundamental equation for the photoelectric effect. XPS can be used to determine the valence state and bonding hybridization of atoms, as these events influence the electron energy levels. In general, the binding energy increases with respect to valence state and bond ionicity. A notable exception is the binding energy of the Co $2p_{3/2}$ orbital, which displays binding energies of $Co^0$ (778.2 eV) < $Co^{3+}$ (779.6 eV) < $Co^{2+}$ (780.5). This is caused by electronic rearrangement (final state) effects after the ejection of photoelectrons to minimize its energy, such as the coupling of unpaired valence electrons with the inner-shell hole.

## 3.4. Electrochemical Characterization

### 3.4.1. Battery Performance Testing

The standard battery testing protocol involves charging and discharging the battery at a constant current (galvanostatic cycling). The voltage response is recorded as a function of charge/discharge time, which is directly proportional to the specific capacity (mAh $g^{-1}$). Energy and capacity values are normalized relative to the mass of the electrode active material (*i.e.,* excluding the binder and conductive additive). The key parameters that dictate the battery performance (specific capacity

and cycle retention) are the upper and lower voltage cut-offs and the charge/discharge current (rate). The current is often reported as a specific value (mA $g^{-1}$) or defined by the C-rate. By definition, a rate of 1 C suggests that it takes one hour to charge/discharge the battery at a rated capacity while 2 C indicates half an hour. Practically, the C-rate is often defined based on a material's theoretical or practical capacity at a certain voltage range – for instance, a theoretical capacity of 140 mAh $g^{-1}$ yields 140 mA $g^{-1}$ = 1 C and 280 mA $g^{-1}$ = 2 C.

At higher charge/discharge rates, the specific capacity retained decreases due to resistances within a cell, which will polarize the voltage output in accordance with Ohm's law ($V = IR$) as seen in Figure 13. In a rate performance test, the cell is progressively cycled at higher currents to determine the capacity retention. A favorable rate performance is generally an indication of good electronic and ionic conductivity of the cathode. For a cycle stability test, the cell is galvanostatically cycled at a constant current. In general, the cycle stability may improve at higher currents, as the depth of discharge is lowered due to voltage polarization. However, for cathodes that experience high volume changes, higher currents will concentrate $Na^+$ at the cathode-electrolyte interface, producing anisotropic volume changes that could lead to particle cracking and disconnection.

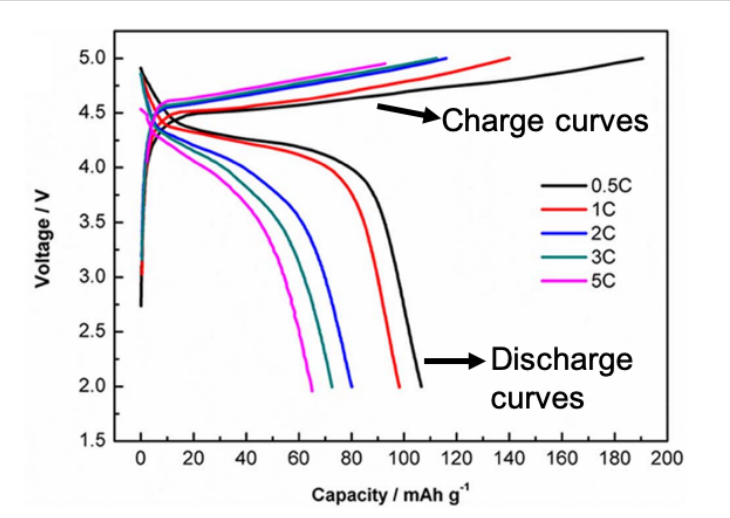

**Figure 13.** Charge-discharge curves of a cell that demonstrates poor rate performance. 1 C = 120 mA $g^{-1}$ current. Reproduced with permission from The Electrochemical Society, 2015.[69]

### 3.4.2. Electrochemical Impedance Spectroscopy

Electrochemical impedance spectroscopy (EIS) is a fundamental technique to delineate resistances within an electrochemical cell. The simplest equivalent circuit model of an electrochemical cell is based on the Randles circuit (Figure 14A). $R_S$ refers to the bulk series resistance of the cell, which is primarily dictated by the electrolyte resistance along with other Ohmic contacts. $C_{dl}$ refers to the electrical double layer at the electrode-electrolyte interface, which can be modelled by a capacitor or constant phase element (CPE). The most critical parameter is the charge-transfer resistance ($R_{ct}$), which describes the interfacial reaction between $Na^+$ and the electrodes. Three are three sequential steps to the intercalation of $Na^+$: 1) solvation/desolvation of $Na^+$, 2) diffusion of $Na^+$ through the SEI layer and potential surface coatings, and 3) Faradic charge transfer upon intercalation. The first two processes are typically rate limiting and define the bulk of $R_{ct}$. Thus, the $R_{ct}$ is often used in battery testing to monitor the stability and build-up of the SEI layer over various cycles. The third step is notable when lattice phase changes suppress $Na^+$ kinetics, and thus increases in $R_{ct}$ is sometimes used to imply phase changes, especially when tested at high voltages. After these processes, $Na^+$ diffuses within the electrode lattice, which is associated with the Warburg element ($Z_W$).

Electrochemical impedance measurements work by applying an AC potential at a range of frequencies and measuring the current response. This can delineate circuit elements due to their relationship with impedance – for instance, the impedance of a capacitor is inversely proportional to the AC frequency while the impedance of a resistor is independent of frequency. Thus, at high frequencies the $R_S$ element can be isolated (Figure 14A). Analysis is conducted using the Nyquist

plot output (Figure 14B) – the x-intercept at high frequency is $R_S$, the width of the complete semicircle is the $R_{ct}$, and the slope of the 45˚ incline at low frequency corresponds to $Z_W$. The exact values are determined using a nonlinear least squares curve fitting program. In typical circumstances, two overlapped semicircles or one asymmetric semicircle is observed. In this scenario, the high-frequency semicircle is denoted $R_{sei}$ and associated with $Na^+$ diffusion through the SEI layer and other surface film, while the mid-frequency semicircle is denoted $R_{ct}$ and is generally proportional to the solid-state diffusivity of $Na^+$ in the electrodes. The equivalent circuit in Figure 14C is used to model this and employed in most publications.

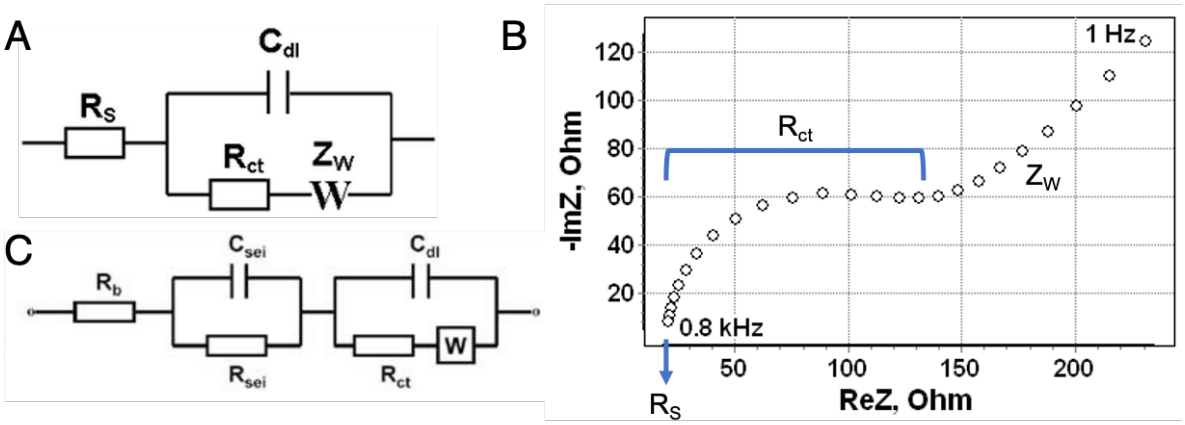


**Figure 14.** EIS analysis of a LIB/SIB cell. A) Randles circuit model for an electrochemical cell. B) Nyquist plot based on Randles circuit. C) Typical equivalent circuit model for LIB/SIB cell. Adapted with permission from Elsevier, 2004.[70]

In this work, the impedance of the coin cells were measured using a two-electrode setup (cathode and sodium foil). While this setup is simple, the impedance measured also accounts for the reaction at the sodium foil anode, which can generate some variability between cells as the sodium foil can have an unstable SEI film. A more precise measurement involves a three-electrode setup, where a separate sodium reference electrode is used that does not participate in the reaction.

### 3.4.3. Galvanostatic Intermittent Titration Technique

The galvanostatic intermittent titration technique (GITT) is often used to derive the solid state diffusion coefficient of $Na^+$ or $Li^+$ within the electrode. The technique works by applying a small constant current pulse and subsequently allowing the voltage to relax to equilibrium conditions. By correlating the voltage change to $Na^+/Li^+$ diffusion in the electrode, the diffusion coefficient can be derived by:

$$D_{Na^+} = \frac{4}{\pi\tau}\left(\frac{n_m V_m}{S}\right)^2 \left(\frac{\Delta E_s}{\Delta E_t}\right)^2$$

where $\tau$ is the duration of the current pulse, $n_m V_m$ is the active material volume ($cm^3$, number of moles multiplied by molar volume), S is the electrode surface area ($cm^2$), $\Delta E_s$ is the steady state voltage change from the current pulse, and $\Delta E_t$ is the voltage change from the constant current pulse (Figure 15). This equation assumes that the voltage window is narrow enough such that $\Delta E_s$ and $\Delta E_t$ are linear. Moreover, key assumptions from the GITT analytical theory should be noted: 1) the electrode is planar, 2) the current is constant and uniform, 3) diffusion is one-dimensional and behaves based on Fick's law, 4) ΔE is only ascribed to the diffusion of $Na^+$ or $Li^+$ in the active material, and 5) the diffusion coefficient is constant throughout.[71]

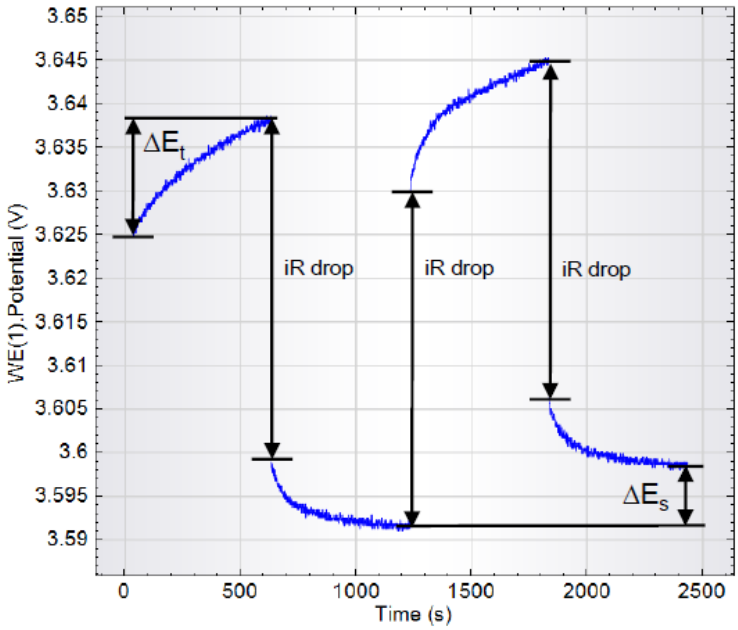


**Figure 15.** GITT measurement using 10 minutes of C/10 charge followed by 10 minutes of relaxation.[72]

# 4. High-Voltage Stability of P2-$Na_{2/3}Mn_{1-y}Mg_yO_2$ Cathode Material for Sodium-Ion Batteries

## 4.1. Introduction

The increasing global demands for energy necessitate technological advancements in clean energy storage. Current energy generation relies on fossil fuels, which are inherently finite, release carbon dioxide into the atmosphere, and are limited in geographic distribution. Lithium-ion battery (LIB) technology is the current state-of-the-art due to their unmatched energy and power density. However, increasing demands for LIBs will constrain natural lithium resources and increase prices, which poses problems for their widespread use in electric vehicles and grid energy storage.[9] Sodium-ion batteries (SIBs) are an emerging technology that has been proposed as an alternative to LIBs due to the low cost and abundance of sodium and their similar intercalation/deintercalation chemistry. SIBs are most promising for use in large-scale grid storage applications where cost and

abundance are particularly important.[73] However, while the raw material cost of sodium-based cathodes is lower than their lithium-based counterparts, the energy density of SIBs is inherently limited because of the higher standard electrode potential of sodium (-2.71 V *vs* SHE) compared to lithium (-3.02 V *vs* SHE). Furthermore, in comparison to LIBs, SIBs demonstrate considerably poorer cycle capacity.[36] This is because SIB cathodes experience structural evolution over repeated intercalation/deintercalation of $Na^+$ with the host structure due to the large ionic radius of $Na^+$ (1.02 Å) compared to $Li^+$ (0.76 Å). Thus, to fully realize the potential of SIBs in large-scale storage, cathode materials comprised of low-cost, abundant, and nontoxic materials that can deliver high energy and power output are required.

Layered transition metal oxides ($Na_xMO_2$, M = Co, Fe, Ni, Ti, V, Cr, or Mn, $x$ = 0.6 – 1) are a common class of cathode materials known for their electrochemical activity and rate performance. They are classified according to O3 and P2-type, which refers to the geometry of the sodium site (octahedral vs. trigonal prismatic) and the number of transition metal oxide layers in the unit cell.[41] In general, P2-type cathodes have a lower sodium content but are more structurally stable and resist phase changes during the charge/discharge process, thus resulting in a higher discharge capacity (when Na-metal foil used as counter electrode) and cycle stability. Furthermore, P2-type cathodes demonstrate favorable diffusion kinetics for $Na^+$ due to the preferred prismatic coordination of the relatively large $Na^+$ ions.[42] Although P2-type cathodes may possess a high theoretical capacity, they must be cycled at high voltage cut-offs ($V_{cut\text{-}off}$, >4.4 V *vs* $Na/Na^+$) in order to exploit this and maximize their energy density. However, extending $V_{cut\text{-}off}$ can severely compromise cathode cyclability due to irreversible phase and volume changes, active material

degradation and dissolution, and uncontrolled electrolyte side reactions. Cathodes that demonstrate good cyclability at high $V_{cut\text{-}off}$ are scarce in the literature.

P2-$Na_xMnO_2$ is a promising SIB cathode composition based on the $Mn^{3+}/Mn^{4+}$ redox due to the abundance, environmental benignity, low cost of Mn, and high theoretical (243 mA h $g^{-1}$) and reported discharge capacity.[74–76] However, this material often demonstrates a drastically poor cycle stability, which is caused by the presence of Jahn-Teller distorted $Mn^{3+}$ ions coupled with phase changes from the insertion and extraction of $Na^+$ ions, thus leading to structural degradation on cycling. In order to improve the performance of P2-$Na_xMnO_2$, Mn is partially substituted with Mg (P2-$Na_xMn_{1-x}Mg_xO_2$, $0 \leq x \leq 0.2$). Adding Mg as a dopant has been found to improve cycle stability by reducing the presence of $Mn^{3+}$,[76,77] enhance the rate performance,[40,78] and create smooth charge/discharge curves. In general, increasing the amount of Mg dopant improves the cycle stability at the expense of lower discharge capacities, as Mg is electrochemically inactive. However, one study reported an anomalous case where P2-$Na_{2/3}Mn_{0.72}Mg_{0.28}O_2$ demonstrated a high initial discharge capacity (~220 mA h $g^{-1}$) at 10 mA $g^{-1}$ when cycled from 1.5 – 4.4 V vs. $Na/Na^+$ albeit with poor cycle stability.[79] This was explained by the high amount of $Mg^{2+}$, which activates the oxide ions to participate in redox as evidently seen in the unique plateau at 4.2 V in the charge curve. Nevertheless, very few studies[77] have demonstrated the performance and cycle stability of P2-$Na_xMn_{1-y}Mg_yO_2$ in the high-voltage region, which is important to improve the energy density of the material, whereas most studies have characterized the material at a $\leq 4.0$ $V_{cut\text{-}off}$.[76,78,80]

In this work, P2-$Na_{2/3}Mn_{1-y}Mg_yO_2$ was synthesized using a modified Pechini process at three Mg dopant quantities, y = 0, 0.05, and 0.01 and systematically characterized at $V_{cut\text{-}off}$ of 4.5, 4.6, and 4.7 V. The long-term capacity retention (over 75 – 100 cycles) and rate performance were assessed for each composition through galvanostatic charge-discharge characterization. Mechanisms of capacity fade were assessed via post-cycling EIS and *ex-situ* XRD characterization.

## 4.2. Materials and Methods

### 4.2.1. Synthesis of P2-$Na_{2/3}Mn_{1-y}Mg_yO_2$

P2-$Na_{2/3}Mn_{1-y}Mg_yO_2$ was synthesized using a modified Pechini method. Stoichiometric amounts (for y = 0.05 and y = 0.1) of sodium (5% excess), manganese, and magnesium acetate (Sigma-Aldrich, Mississauga, Canada) were dissolved in distilled water (0.25 M metal ions). An equivalent volume of aqueous 0.575 M citric acid (Sigma-Aldrich) and aqueous 5 wt% poly(ethylene glycol) (number-average $M_W$ = 8,000 Da) were added dropwise to the metal-acetate mixture. Ethylene glycol (3 mL, Sigma-Aldrich) and concentrated nitric acid (1 mL, 70%, Sigma-Aldrich) were then added dropwise to the mixture, which was stirred at 110˚C for ~ 4 h. The resulting gel precursor was dried overnight at 110˚C, then pre-calcined at 400˚C for 4 h in a muffle furnace (Thermo Scientific, Mississauga, Canada) to remove organic residue. Finally, the resulting powder was ground and sintered at 850˚C for 12 hr in a tube furnace (Thermo Scientific) under open air. The final P2-$Na_{2/3}Mn_{1-y}Mg_yO_2$ powder was stored in a vacuum oven to avoid water ingress and oxidation.

### 4.2.2. Characterization of P2-$Na_{2/3}Mn_{1-y}Mg_yO_2$ Particles

The phase purity of the active material was assessed using powder X-ray diffraction (XRDMiniflex 600, Rigaku, Japan) with Cu $K_\alpha$ radiation ($\lambda$ = 1.5406 nm). The morphology of the particles was observed using scanning electron microscopy (SEM, LEO Zeiss 1550, Switzerland) using a 20 kV acceleration voltage and a working distance between 8 – 9 mm. Rietveld refinement was conducted on MAUD software[81] using COD ID: 1525855[82] as a reference. Inductively coupled plasma atomic emission spectroscopy (ICP-AES) was conducted after dissolution of metal oxides in Aqua regia (4:1 concentrated HCl:$HNO_3$ (v/v)).

### 4.2.3. Preparation of P2-$Na_{2/3}Mn_{1-y}Mg_yO_2$ Electrode

The electrode was prepared by grinding a slurry of 70 wt% active material, 20% conductive carbon black (Ketjenblack, Lion Specialty Chemical Co., Japan), and 10% PTFE-acetylene black binder in ethanol using a mortar and pestle. The electrode film was pressed (~10,000 kPa) onto a 15 mm diameter stainless steel mesh and dried overnight at 80˚C in a vacuum oven. The active material loading was 6 mg $cm^{-2}$.

### 4.2.4. Electrochemical Characterization of P2-$Na_{2/3}Mn_{1-y}Mg_yO_2$ Electrode

The electrochemical performance of the P2-$Na_{2/3}Mn_{1-y}Mg_yO_2$ electrode was assessed by assembling CR2032 coin cells in an argon-filled glove box ($O_2$ and $H_2O$ ppm < 0.5) using a pure sodium foil (Sigma-Aldrich) as the counter electrode, a polypropylene separator (Celgard 2400, Charlotte, NC, USA), and an electrolyte comprised of 1 M $NaClO_4$ dissolved in 1:1:0.05 ethylene carbonate:diethyl carbonate:fluoroethylene carbonate (Sigma-Aldrich) by volume. Charge-discharge studies were carried out at ambient temperature using a CT2001A LAND battery testing

system (Wuhan, China). Electrochemical impedance spectroscopy (EIS) measurements (Gamry Instruments, Warminster, PA, USA) were conducted from 1 MHz to 100 mHz at a discharged state (~2 V).

## 4.3. Results and Discussion

$Na_{2/3}Mn_{1-y}Mg_yO_2$ was synthesized using a modified Pechini method at two compositions with target stoichiometries of $Na_{2/3}Mn_{0.95}Mg_{0.05}O_2$ and $Na_{2/3}Mn_{0.9}Mg_{0.1}O_2$. In this technique, the metal ion precursors are dissolved in dilute $HNO_3$(aq) and mixed with citric acid and PEG. The metal ions form coordination complexes with citric acid while PEG grafts onto the citric acid through an esterification reaction, forming a polymeric resin where cations are uniformly distributed. Following calcination and decomposition of the polymer matrix, the ceramic particles produced typically possess a smaller and more uniform size compared to conventional sol-gel methods.[64,83,84] The synthesized compositions were confirmed using ICP-AES with resulting Mg/Mn ratios of 0.0512 and 0.115 respectively. SEM images of the particles are shown in Figure 16C-D. Both compositions display an identical plate-like particle morphology with sizes ranging from 1 – 3 μm, which is typically observed in P2-layered structures. To our knowledge, no other studies have explored the modified Pechini synthesis method for this composition. In comparison, the same composition was synthesized using a conventional citric-acid assisted sol-gel method using identical sintering conditions. SEM images of the resultant particles (Figure 16A-B) appear larger with a more heterogeneous size distribution (2 – 5 μm). The benefits of having a smaller and uniform particle size toward electrochemical performance are well established – the higher surface area can increase the availability of electrochemical reaction sites and improve contact between the particles, thus improving electrical conductivity and capacity, while also shortening the

diffusion length for $Na^+$.[85] Thus, $Na_{2/3}Mn_{1-y}Mg_yO_2$ synthesized using the modified Pechini method was used for further physical and electrochemical characterization.

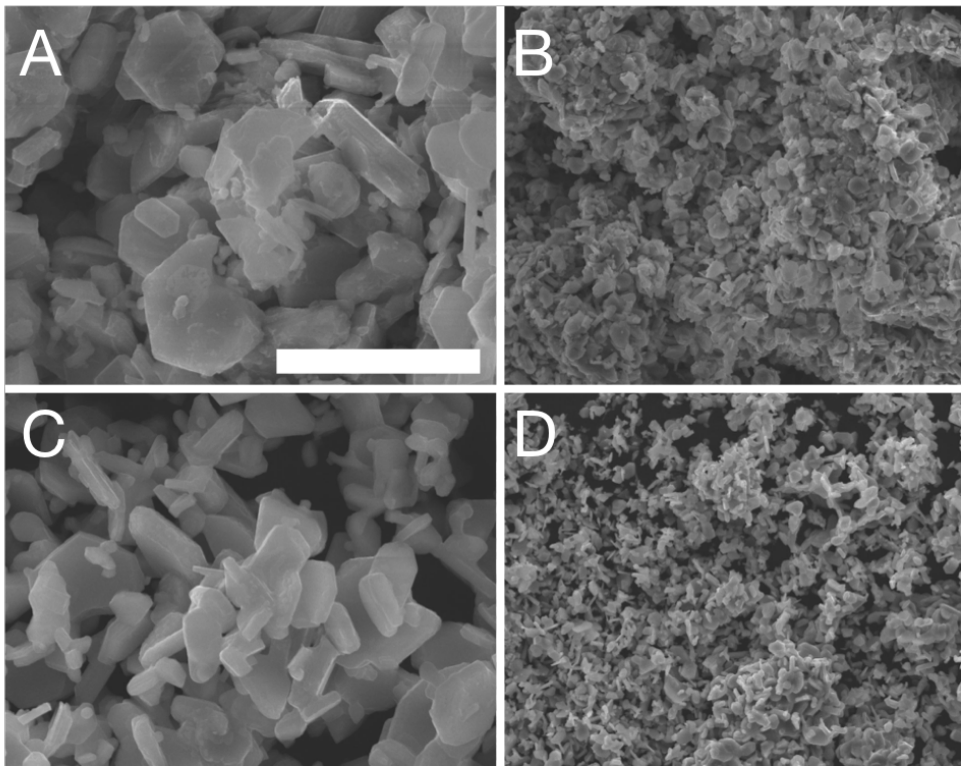


**Figure 16.** SEM images of synthesized P2- $Na_{2/3}Mn_{1-y}Mg_yO_2$ particles using A and B) citric-acid assisted sol-gel method; C and D) modified Pechini method. Scale bar: 10 µm (A and C), 50 µm (B and D)

The powder XRD spectra (Figure 17) shows that $Na_{2/3}Mn_{1-y}Mg_yO_2$ formed a phase-pure P2-layered material with a hexagonal lattice indexed to the $P6_3/mmc$ space group. The hexagonal lattice parameters were obtained using via a Rietveld refinement, yielding $a$ = 2.888, $c$ = 11.314 for y = 0.1 and $a$ = 2.882, $c$ = 11.281 for y = 0.05. The lattice parameters increase with higher $Mg^{2+}$ substitution due to $Mg^{2+}$ having a larger ionic radius compared to $Mn^{3+}/Mn^{4+}$.[86] The larger $c$-axis lattice parameter implies an expanded interlayer space for the y = 0.1 composition, which can improve $Na^+$ diffusion kinetics and facilitate reversibility of potential phase changes. It should

be noted that no superlattice peaks that may correspond to $Na^{+}$/vacancy or $Mn^{3+}/Mn^{4+}/Mg^{2+}$ ordering were observed in the spectra.[76,77]

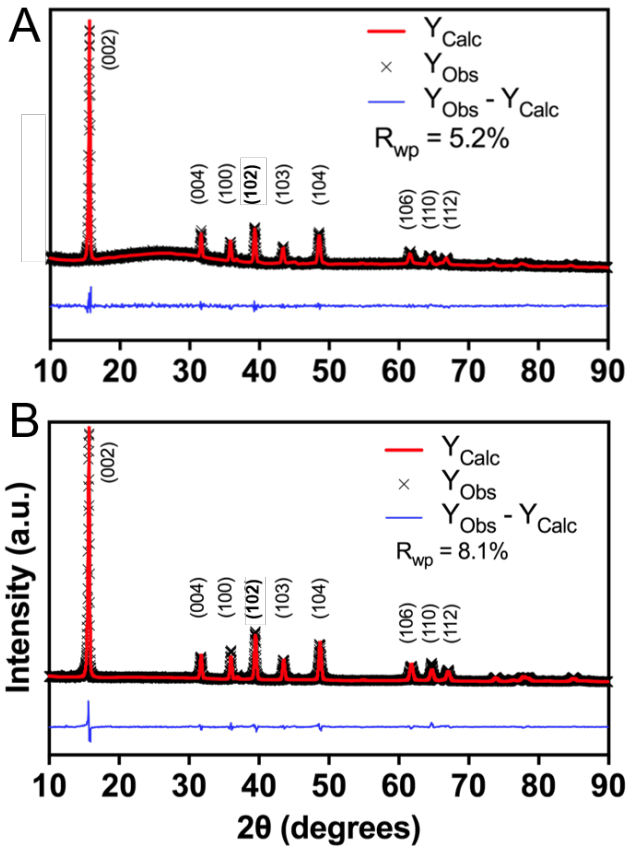


**Figure 17.** Refined XRD spectra of pristine P2-$Na_{2/3}Mn_{1-y}Mg_yO_2$. A) y = 0.1, $R_{wp}$ = 5.2% B) y = 0.05, $R_{wp}$ = 8.1%

### 4.3.1. $Na_{2/3}Mn_{1-y}Mg_yO_2$ Electrochemical Performance

The galvanostatic charge-discharge performance results are summarized in Table 2 below. The initial charge-discharge curves of $Na_{2/3}Mn_{0.95}Mg_{0.05}O_2$ at various $V_{cut\text{-}off}$ are shown in Figure 18A, which appear significantly smoother compared to our synthesized $Na_{2/3}MnO_2$ (Figure 19). As clearly shown in the dQ/dV plots (Figure 20), the peaks appearing from 2.1 – 2.4 V for $Na_{2/3}Mn_{0.95}Mg_{0.05}O_2$ correspond to the $Mn^{3+}/Mn^{4+}$ redox reaction while the 3.0 – 3.5 V peaks are

ascribed to a reversible P2-OP4 phase transition.[40] This transition occurs when $Na^+$ is extracted from large prismatic sites within the P2 phase with 'AB BA' stacking. As $Na^+$ is extracted, adjacent transition metal oxide slabs repel electrostatically, which generally corresponds with an expansion of the *c*-axis lattice parameter and shrinking of the *a* parameter.[45] With further extraction, the process is also associated with slab gliding for energetic balance, forming octahedral vacancies that shrink the interlayer spacing. The stacked-fault OP4 phase is an intermediate transition occurring ~3.5-3.6 V where every other prismatic layer is converted into an octahedral layer with 'AB BA CB BC' stacking. At ~4.2 – 4.3 V, the prismatic sites may convert entirely to octahedral sites, resulting in an O2 phase with 'ABC BAB' stacking. The formation of this phase is clearly observed in compositions such as P2-$Na_{2/3}Ni_{1/3}Mn_{2/3}O_2$.[45] The O2 phase transition is not as reversible as the OP4 transition and is a significant reason for capacity fade when cycling at high $V_{cut\text{-}off}$ ranges. The effect of $Mg^{2+}$ doping on P2 cathodes has been characterized in prior work.[87,88] $Mg^{2+}$ can suppress and delay the onset OP4 and P2 phase transition by allowing more $Na^+$ ions to reside in prismatic sites during charging. For Mn-rich cathodes, $Mg^{2+}$ doping significantly improves the cycle retention as it not only delays the OP4 and P2 phase transitions, but also increases the average ionicity of Mn, and thus suppresses ordering effects and structural changes associated with Jahn-Teller distorted $Mn^{3+}$ ions. This corresponds to much smoother-appearing charge-discharge curves for the Mg-doped samples. While our synthesized $Na_{2/3}MnO_2$ possessed a distinct oxidation peak at 4.22 V (Figure 19B), this was not observed in $Na_{2/3}Mn_{0.95}Mg_{0.05}O_2$ (Figure 20), confirming that Mg doping suppressed/delayed the P2-O2 phase transition. The smoothing of plateaus appearing below 4.0 V also implies that Mg substitution suppressed $Na^+$/vacancy ordering.[89] Both samples displayed a distinct peak when charged to ~4.7 V,

suggesting that $Na^+$ extraction was strained at this $V_{cut\text{-}off}$ and likely approached the theoretical limit.

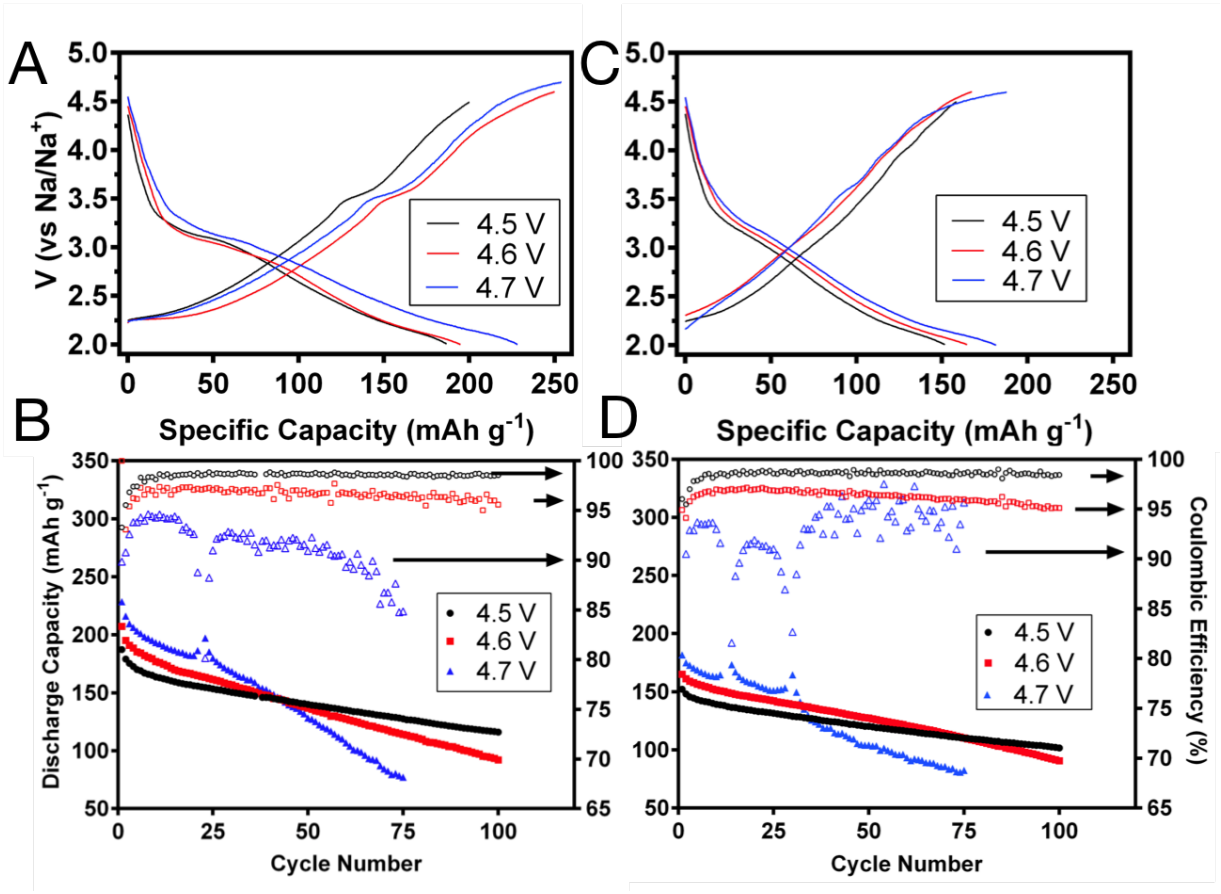


**Figure 18.** Initial galvanostatic charge-discharge curves (A and C) and cycle stability (B and D) for $Na_{2/3}Mn_{1-y}Mg_yO_2$, y = 0.05 (A and B) and y = 0.1 (C and D) at 4.5, 4.6, and 4.7 $V_{cut\text{-}off}$.

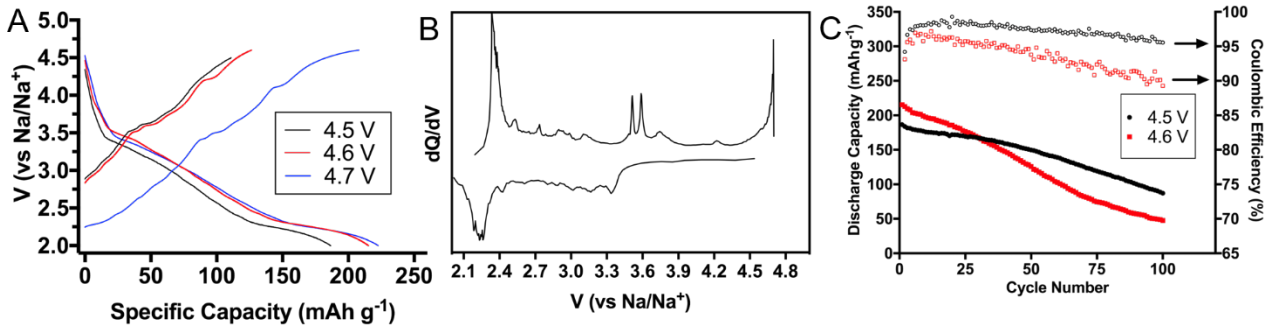

**Figure 19.** Electrochemical performance of $Na_{2/3}MnO_2$ at 40 mA $g^{-1}$. A) Initial charge-discharge curves. B) dQ/dV plots of second charge-discharge cycle from 2 – 4.7 V. C) Capacity retention and coulombic efficiency over 100 cycles.

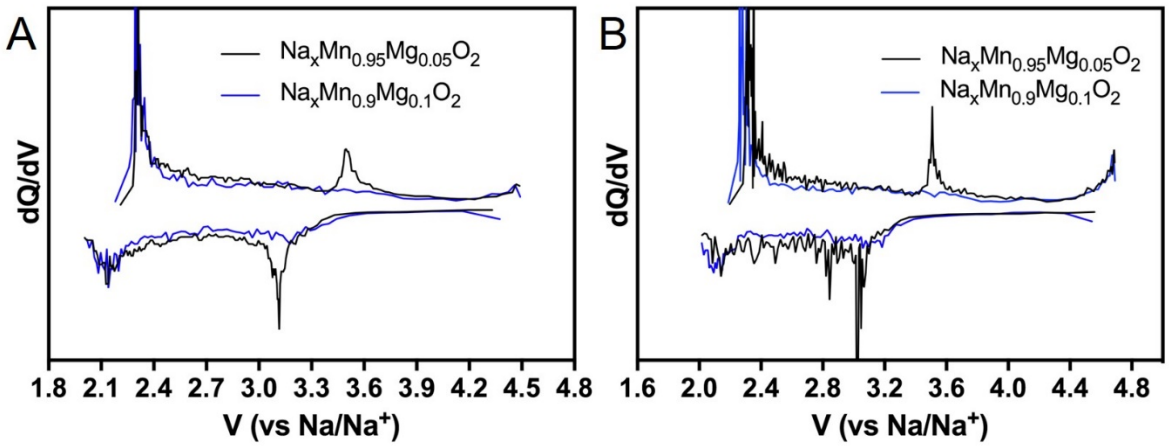


**Figure 20.** dQ/dV plot of second charge-discharge cycle of $Na_{2/3}Mn_{0.95}Mg_{0.05}O_2$ and $Na_{2/3}Mn_{0.9}Mg_{0.1}O_2$ at A) 4.5 $V_{cut\text{-}off}$ and B) 4.7 $V_{cut\text{-}off}$.

Electrochemical performance of our synthesized Mg-doped cathodes was characterized at three upper $V_{cut\text{-}off}$: 4.5, 4.6, and 4.7 V. As expected, the initial discharge capacity increased with respect to $V_{cut\text{-}off}$ due to the increased $Na^+$ extraction, but this came at the expense of poorer capacity retention. It is well understood that at high $V_{cut\text{-}off}$, cyclability is reduced substantially due to 1) irreversible changes in the bulk structure (*e.g.*, slab gliding and $Na^+$/vacancy ordering), 2) extensive decomposition of electrolyte resulting in increased interfacial resistance due to unstable solid-electrolyte-interphase (SEI) layer growth, 3) solvent insertion within the interlayer space of transition metal oxide slabs, and 4) active material dissolution and particle/electrode pulverization from extensive cycling.[44] These factors for capacity degradation are examined in subsequent sections. It is interesting to note that $Na_{2/3}Mn_{0.95}Mg_{0.05}O_2$ displayed a similar initial discharge capacity (Table 2) compared to our synthesized $Na_{2/3}MnO_2$; however, the 5% substitution of $Mn^{3+}/Mn^{4+}$ with $Mg^{2+}$ enhanced the cycle retention significantly. When cycling between 2 – 4.5

V, the capacity retention of $Na_{2/3}Mn_{0.95}Mg_{0.05}O_2$ was promising, retaining 140 mAh $g^{-1}$ (82%) and 116 mAh $g^{-1}$ (68%) after 50 and 100 cycles respectively. Table 3 compares this capacity retention to other layered oxide cathodes in the literature cycled at similar voltage range and current. Cycle stability enhancement was more pronounced at higher $V_{cut\text{-}off}$, for instance $Na_{2/3}Mn_{0.95}Mg_{0.05}O_2$ retained 50% of its discharge capacity after 100 cycles between 2 – 4.6 V, whereas $Na_{2/3}MnO_2$ decayed to 23%. At 4.7 $V_{cut\text{-}off}$, the initial discharge capacity of $Na_{2/3}Mn_{0.95}Mg_{0.05}O_2$ (229 mAh $g^{-1}$) is among the highest ever reported for a sodium layered metal oxide[90] – it should be noted that despite the low average discharge potential (2.7 V), this still corresponds to an ultra-high energy density of 616 Wh $kg^{-1}$. However, cycle stability was drastically poorer, retaining 38% capacity after 75 cycles. Figure S4 shows the evolution of the charge-discharge curves over 100 cycles at the various $V_{cut\text{-}off}$. It is evident that voltage polarization increased with respect to $V_{cut\text{-}off}$ and cycle number. However, the shape of the curves at 4.5 and 4.6 $V_{cut\text{-}off}$ remained similar, whereas at 4.7 $V_{cut\text{-}off}$, a severe shrinkage of the smooth plateau from 2 – 3.25 V was observed. This suggests that active material dissolution/degradation was a significant factor for capacity loss. It is understood that the Jahn-Teller distorted $Mn^{3+}$ ion can undergo a disproportionation reaction to form $Mn^{4+}$ and $Mn^{2+}$, where $Mn^{2+}$ is known to dissolve in liquid carbonate-based electrolyte.[91] The charge curve plateaus at ~4.7 V indicates that $Na^+$ extraction was strained at this $V_{cut\text{-}off}$ due to irreversible losses of $Na^+$ availability. The capacity contribution from the plateaus likely correspond to electrolyte decomposition, which is reflected by the low coulombic efficiency.

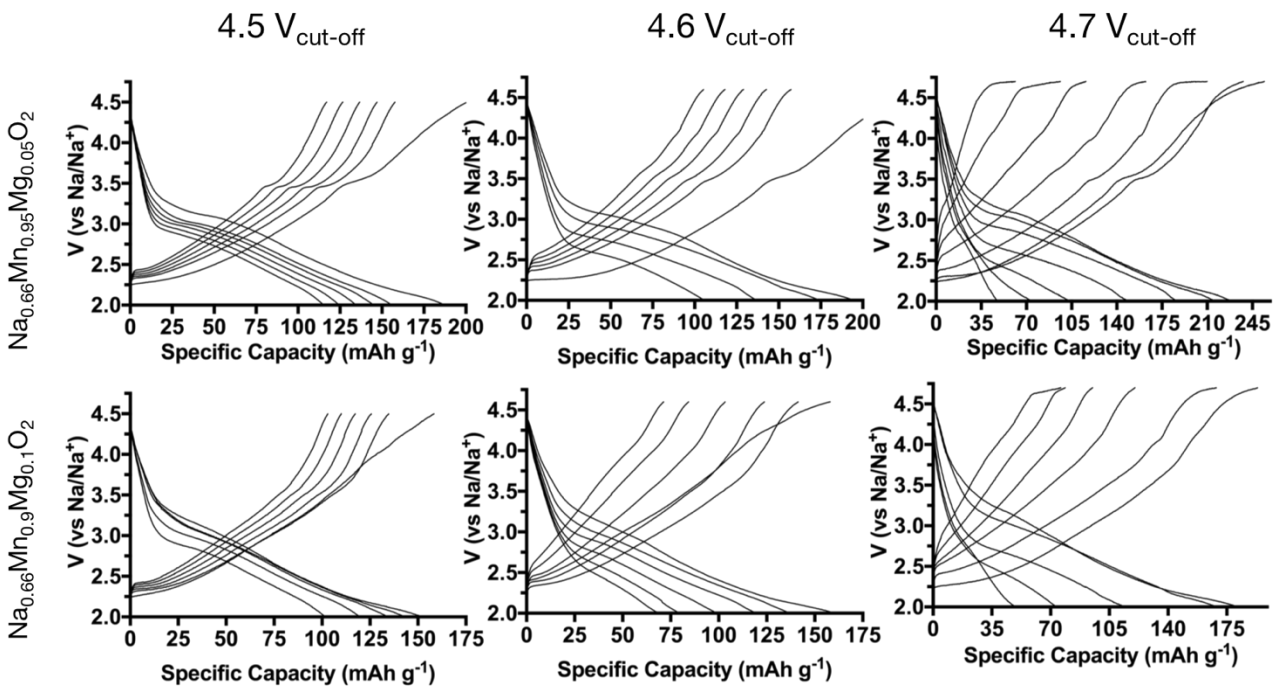


**Figure 21.** Evolution of charge-discharge curves of $Na_{2/3}Mn_{1-y}Mg_yO_2$ from cycle 1 to 100 at various $V_{cut\text{-}off}$.

On the other hand, the charge-discharge curves of $Na_{2/3}Mn_{0.9}Mg_{0.1}O_2$ showed no peaks from 3.0 – 3.5 V, suggesting that the P2-OP4 phase transition was suppressed due to the higher quantity of Mg dopant. As expected, the initial discharge capacity was suppressed compared to $Na_{2/3}Mn_{0.95}Mg_{0.05}O_2$, whereas the cycle stability improved. The improvement was more notable when cycled at $V_{cut\text{-}off}$, supporting the claim that Mg delays and suppresses irreversible high-voltage phase transitions. A comparison between the compositions (y = 0, 0.05, 0.1) is shown in Figure 22. At 4.5 $V_{cut\text{-}off}$, $Na_{2/3}Mn_{0.95}Mg_{0.05}O_2$ and $Na_{2/3}Mn_{0.9}Mg_{0.1}O_2$ have a similar trend in cycle stability. However, at 4.6 and 4.7 $V_{cut\text{-}off}$, the two compositions reach the same discharge capacity after ~100 and 73 cycles respectively. Thus, the energy density and long-term cyclability of $Na_{2/3}Mn_yMg_{1-y}O_2$ can be maximized at a y = 0.05 composition at 4.5 $V_{cut\text{-}off}$.

**Table 2.** Summary of electrochemical performance benchmarks of $Na_{2/3}Mn_{1-y}Mg_yO_2$ cycled at various voltage ranges.

| | Voltage Range | $Na_{2/3}Mn_{0.9}Mg_{0.1}O_2$ | $Na_{2/3}Mn_{0.95}Mg_{0.05}O_2$ |
|---|---|---|---|
| Initial Discharge Capacity (mAh $g^{-1}$) | 2 – 4.5 V | 152 | 187 |
| | 2 – 4.6 V | 165 | 207 |
| | 2 – 4.7 V | 182 | 229 |
| Capacity Retention | 2 – 4.5 V (100 Cycles) | 71% | 68% |
| | 2 – 4.6 V (100 Cycles) | 58% | 50% |
| | 2 – 4.7 V (100 Cycles) | 49% | 38% |
| Coulombic Efficiency (Cycle 5) | 2 – 4.5 V | 98.5% | 98.7% |
| | 2 – 4.6 V | 96.4% | 96.2% |
| | 2 – 4.7 V | 93.7% | 93.8% |
| Discharge Capacity at 50, 83, 167, 250, and 333 mA $g^{-1}$ respectively | 2 – 4.5 V | 145, 136, 120, 105, and 94 mAh $g^{-1}$ | 177, 159, 142, 125, and 112 mAh $g^{-1}$ |
| | 2 – 4.6 V | 159, 142, 124, 109, and 98 mAh $g^{-1}$ | 196, 168, 134, 113, and 99 mAh $g^{-1}$ |
| | 2 – 4.7 V | 175, 153, 130, 108, and 93 mAh $g^{-1}$ | 204, 179, 154, 129, 108 mAh $g^{-1}$ |

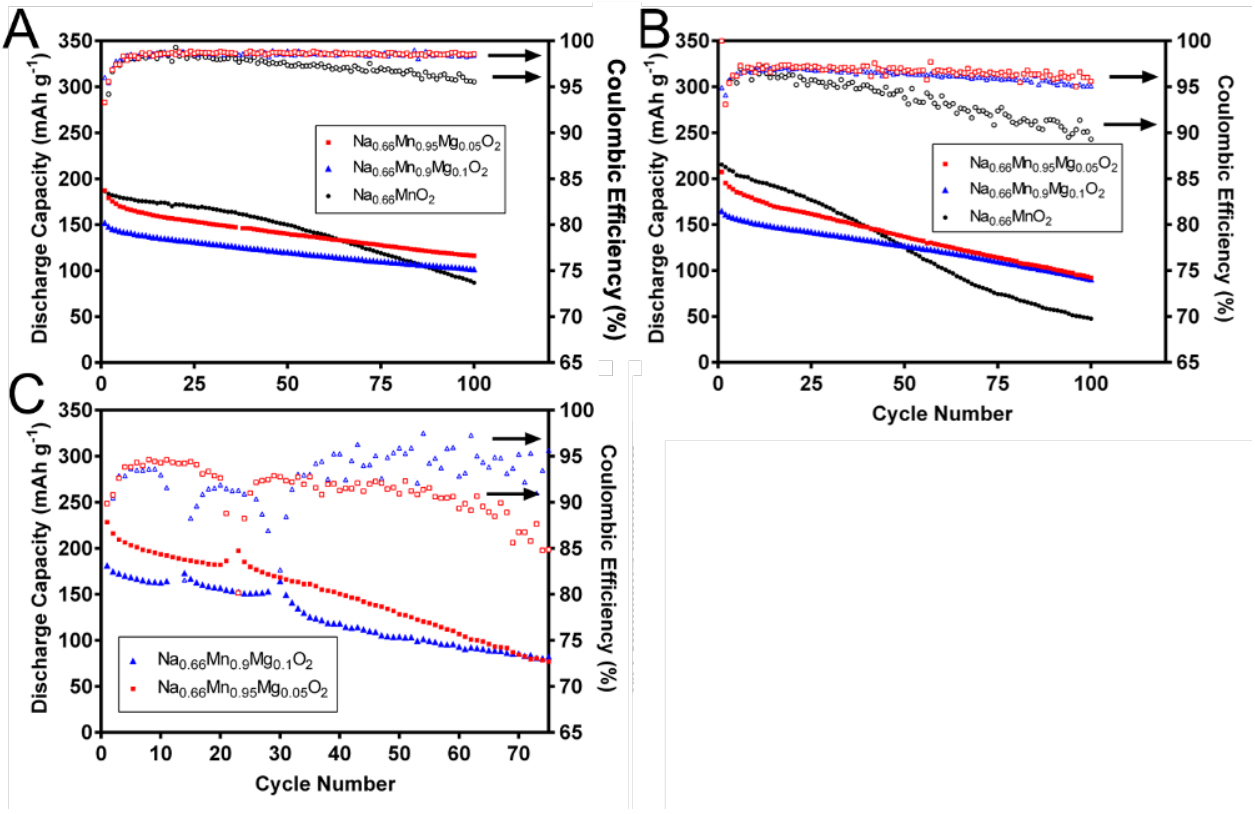


**Figure 22.** Comparison of cycle performance of $Na_{2/3}Mn_{1-y}Mg_yO_2$ at various $V_{cut\text{-}off}$. A) 4.5 $V_{cut\text{-}off}$, B) 4.6 $V_{cut\text{-}off}$, C) 4.7 $V_{cut\text{-}off}$

The rate performance of both Mg-doped compositions is shown in Figure 3. An interesting trend is noted where the discharge capacity is throttled at high current when cycled at high cut-off voltages. At a 4.5V cut-off, $Na_{2/3}Mn_{0.95}Mg_{0.05}O_2$ lost 63% of its discharge capacity from 50 to 333 mA $g^{-1}$, while a 51% and 53% capacity loss were observed at 4.6 and 4.7 $V_{cut\text{-}offs}$ respectively. Similarly, $Na_{2/3}Mn_{0.9}Mg_{0.1}O_2$ lost 65%, 62%, and 53% of its discharge capacity at 4.5, 4.6, and 4.7 $V_{cut\text{-}off}$ respectively at the same current density range. A similar trend was observed by Buchholz *et al.* when comparing the rate capability of $Na_xMn_{0.89}Mg_{0.11}O_2$ at 4.4 and 4.6 $V_{cut\text{-}off}$.[77] This effect is ascribed to the kinetic unfavorability of the high-voltage phase transitions, supported by the fact that our synthesized $Na_{2/3}Mn_{0.9}Mg_{0.1}O_2$ greatly outperformed $Na_{2/3}Mn_{0.95}Mg_{0.05}O_2$ at a 4.6 V cut-off. It is understood that there is a high energy barrier for $Na^+$ diffusion through octahedral sites

that form at high voltages, due to strong Coulombic repulsion between $Na^+$ and the metal oxide layers.[92] The improved rate capability of $Na_{2/3}Mn_{0.9}Mg_{0.1}O_2$ can also be ascribed to its expanded *c*-axis lattice parameter, which enables facile diffusion of $Na^+$ in the interlayer spacing.[93] Furthermore, reducing the amount of Jahn-Teller active ions and $Na^+$/vacancy ordering by increasing the Mg doping has significant impact toward reducing the energy barrier for $Na^+$ diffusion.[94]

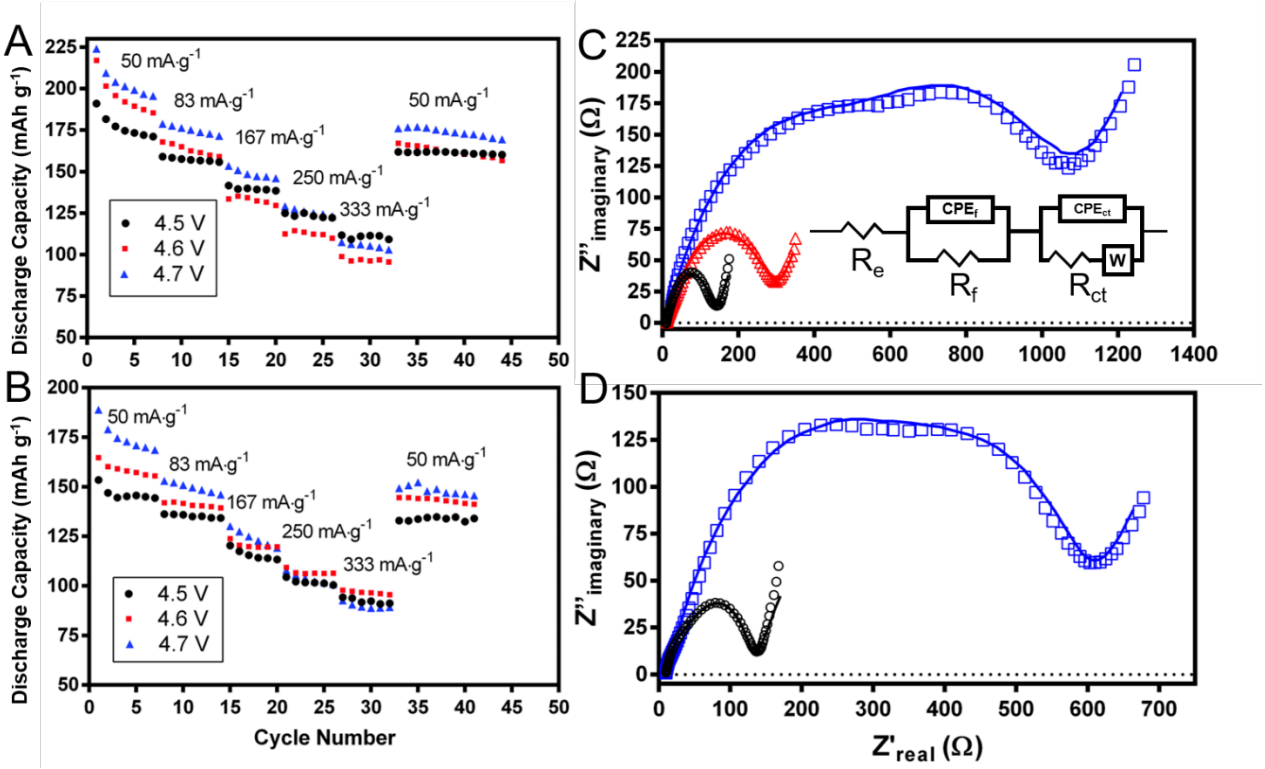


**Figure 23.** Rate performance of A) $Na_{2/3}Mn_{0.95}Mg_{0.05}O_2$ and B) $Na_{2/3}Mn_{0.9}Mg_{0.1}O_2$. EIS spectra after 100 cycles. Symbols represent the data point while solid lines show the fitted spectra. C) $Na_{2/3}Mn_{0.95}Mg_{0.05}O_2$ cycled at $V_{cut\text{-}off}$ of 4.5 V (black), 4.6 V (red), and 4.7 V (blue). D) $Na_{2/3}Mn_{0.9}Mg_{0.1}O_2$ cycled at $V_{cut\text{-}off}$ of 4.5 V (black) and 4.7 V (blue).

**Table 3.** Comparison of long-term discharge capacity retention of our synthesized $Na_{2/3}Mn_{1-y}Mg_yO_2$ with other layered oxides in the literature cycled at similar voltage ranges based on the maximum number of cycles reported.

| Material | Discharge Capacity Retained (mAh $g^{-1}$) | Current | Number of Cycles | Voltage Range (V) | Reference |
|---|---|---|---|---|---|

| | | | | | |
|---|---|---|---|---|---|
| This Work – $Na_{2/3}Mn_{0.95}Mg_{0.05}O_2$ | 116 | 40 mA $g^{-1}$ | 100 | 2 – 4.5 | - |
| This Work – $Na_{2/3}Mn_{0.9}Mg_{0.1}O_2$ | 102 | 40 mA $g^{-1}$ | 100 | 2 – 4.5 | - |
| $Na_{2/3}Ni_{0.3}Co_{0.1}Mn_{0.6}O_2$ | 128 | 0.1 C | 50 | 2 – 4.3 | [95] |
| $Na_{2/3}Ni_{0.23}Mn_{2/3}Mg_{0.1}O_2$ | 84.9 | 48 mA $g^{-1}$ | 100 | 2 – 4.5 | [96] |
| $Na_{2/3}Ni_{0.19}Zn_{0.14}Mn_{2/3}O_2$ | 118 | 12 mA $g^{-1}$ | 30 | 2 – 4.4 | [89] |
| $Na_{2/3}Ni_{1/3}Mn_{2/3}O_2$ | 40 | 17 mA $g^{-1}$ | 100 | 2 – 4.5 | [97] |
| $NaFe_{0.2}Mn_{0.4}Ni_{0.4}O_2$ | 144 | 0.05 C | 20 | 2 – 4.3 | [98] |
| $Na_{2/3}Mn_{0.54}Ni_{0.13}Co_{0.13}O_2$ | 61 | 1 C | 100 | 2 – 4.5 | [99] |
| $Na_{0.5}Ni_{0.25}Cu_{0.07}Mn_{2/3}O_2$ | 92 | 45 mA $g^{-1}$ | 100 | 2 – 4.5 | [100] |
| $Na_{2/3}Mn_{2/3}Ni_{0.28}Mg_{0.05}O_2$ | 105 | 17 mA $g^{-1}$ | 50 | 2.5 – 4.35 | [87] |
| $Na_{2/3}Mn_{1/2}Co_{1/3}Cu_{1/6}O_2$ | 78 | 20 mA $g^{-1}$ | 100 | 1.6 – 4.3 | [101] |
| $Na_{2/3}Ni_{1/3}Mn_{7/12}Fe_{1/12}O_2$ | 127 | 0.1 C | 50 | 2.2 – 4.4 | [102] |
| $Na_{2/3}Ni_{0.2}Mg_{0.1}Mn_{0.7}O_2$ | 122.4 | 12 mA $g^{-1}$ | 50 | 2 – 4.5 | [88] |

### 4.3.2. Post-Cycling Characterization

The EIS spectra of the electrodes after 100 cycles at 40 mA $g^{-1}$ were obtained to study the interfacial properties of the electrodes at various conditions. The Nyquist plots (Figure 23C) of $Na_{2/3}Mn_{0.95}Mg_{0.05}O_2$ cycled at 4.5 and 4.6 $V_{cut\text{-}off}$ show a semicircle at the high-medium frequency region followed by a straight incline at low frequency, which correspond to the electrode/electrolyte charge-transfer impedance ($R_{ct}$) and Warburg impedance (W) respectively. Figure 23C shows that $R_{ct}$ increases substantially when cycled at higher $V_{cut\text{-}off}$, which reflects the poor kinetics likely associated with irreversible phase changes at high $V_{cut\text{-}off}$. With extensive cycling at 4.7 $V_{cut\text{-}off}$, a new overlapped semicircle appears at the high-frequency region, which is ascribed to a $Na^+$ migration impedance ($R_f$) through the surface of the electrode. This likely arises from the formation of a thick SEI layer due to significant decomposition of the carbonate-based electrolyte at this $V_{cut\text{-}off}$, combined with irreversible structural degradation on the surface of the active material.[89] The magnitudes of $R_f$ and $R_{ct}$ are substantial after cycling at 4.7 $V_{cut\text{-}off}$ – Table 4 shows the calculated impedances from curve fitting based on the equivalent circuit shown as an

inset of Figure 23C. In comparison, $Na_{2/3}Mn_{0.9}Mg_{0.1}O_2$ cycled at 4.5 $V_{cut\text{-}off}$ displayed a similar $R_{ct}$ to $Na_{2/3}Mn_{0.95}Mg_{0.05}O_2$, while at 4.7 $V_{cut\text{-}off}$, the magnitude of $R_f$ and $R_{ct}$ was considerably lower (Figure 23D). These results indicate that SEI layer growth is a significant factor for capacity loss at 4.7 $V_{cut\text{-}off}$, and supports the fact that Mg substitution can suppress irreversible high-voltage phase changes, resulting in improved capacity retention and kinetics.

**Table 4.** EIS parameters from curve fitting after 100 charge-discharge cycles

| Material | $V_{cut\text{-}off}$ | $R_e$ (Ω) | $R_f$ (Ω) | $R_{ct}$ (Ω) |
|---|---|---|---|---|
| $Na_{2/3}Mn_{0.95}Mg_{0.05}O_2$ | 4.5 | 10.4 | 26.2 | 103.2 |
| $Na_{2/3}Mn_{0.95}Mg_{0.05}O_2$ | 4.6 | 10.7 | 25.3 | 259.3 |
| $Na_{2/3}Mn_{0.95}Mg_{0.05}O_2$ | 4.7 | 14.2 | 528.6 | 570.9 |
| $Na_{2/3}Mn_{0.9}Mg_{0.1}O_2$ | 4.5 | 9.6 | 31.7 | 90.4 |
| $Na_{2/3}Mn_{0.9}Mg_{0.1}O_2$ | 4.7 | 12.5 | 181.4 | 394.5 |

In order to study the structural stability of $Na_{2/3}Mn_{0.9}Mg_{0.1}O_2$ and $Na_{2/3}Mn_{0.95}Mg_{0.05}O_2$, samples were characterized via *ex-situ* XRD at various stages of cycling from 2 – 4.5 V. Figure 24 reveals that for both compositions, the P2 structure was retained throughout cycling, with no discernible shifts in peak position and intensity ratio. Even the XRD spectra at 4.5 V (first charge) showed no peaks associated with the octahedral phase, which confirms that Mg doping suppresses/delays the P2-O2/OP4 phase transition and explains the smoothened charge-discharge profile and better capacity retention. Formation of the octahedral phase is typically observed in desodiated P2 structures (> 3.8 V), and is characterized by an upshifted reflection of the (002) peak (denoted (002')) that corresponds to a contraction of the *c*-axis.[45] This is also associated with peak broadening due to the formation of stacking faults from slab gliding. However, after 150 charge-discharge cycles, a minor (002') peak at ~18º was observed in both $Na_{2/3}Mn_{0.9}Mg_{0.1}O_2$ and

$Na_{2/3}Mn_{0.95}Mg_{0.05}O_2$. This reflects a contraction of the interlayer space with O2-type stacking.[103–105] It is often explained as an OP4 phase that possesses alternating layers of octahedral and prismatic sites along the *c*-axis.[103] Alternatively, it is referred to the Z phase and ascribed to the migration of a transition metal ions (M) into the interlayer space to form $MO_4$ tetrahedra caused by high $Na^+$ vacancy. This induces short range order between the metal oxide slabs with O2 stacking.[105] The presence of the (002') peak indicates that minor irreversible phase changes occurred over long-term cycling at 4.5 $V_{cut\text{-}off}$. Differences between the $Na_{2/3}Mn_{0.9}Mg_{0.1}O_2$ and $Na_{2/3}Mn_{0.95}Mg_{0.05}O_2$ spectra were observed upon closer examination after 150 charge-discharge cycles (Figure 24C). The (102), (104), (106), and (110) peaks on $Na_{2/3}Mn_{0.95}Mg_{0.05}O_2$ appear spectra to broaden, which we believe is associated with inhomogeneous microstrains and stacking faults in the P2 structure due to slab gliding. Thus, the *ex-situ* XRD studies confirm that the increased Mg doping extends cyclability by suppressing irreversible structural changes.

The *ex-situ* XRD spectra of $Na_{2/3}Mn_{0.95}Mg_{0.05}O_2$ after 150 and 100 cycles at 4.6 and 4.7 $V_{cut\text{-}off}$ respectively are shown in Figure 25. Peaks corresponding to the hydrated P2-phase were observed in both samples, which reflects an expanded interlayer space caused by electrolyte insertion between the transition metal oxide slabs.[106] This phase is commonly observed when charged to high voltages, due to the increased susceptibility toward electrolyte insertion at low $Na^+$ content.[87,95] Both samples also displayed greater peak broadening, which is indicative of more stacking faults. In addition, a broad (002') peak at ~22º was observed which can be indexed as the O2-phase. The peak intensity was considerably greater for the sample cycled at 4.7 $V_{cut\text{-}off}$. These results indicate that irreversible electrolyte insertion and phase changes were largely responsible for the loss of $Na^+$ storage capacity. It should be noted that significant active material dissolution

was observed for the sample cycled at 4.7 $V_{cut\text{-}off}$, which corresponds with the drastic evolution of the charge-discharge curves shown in Figure 21.

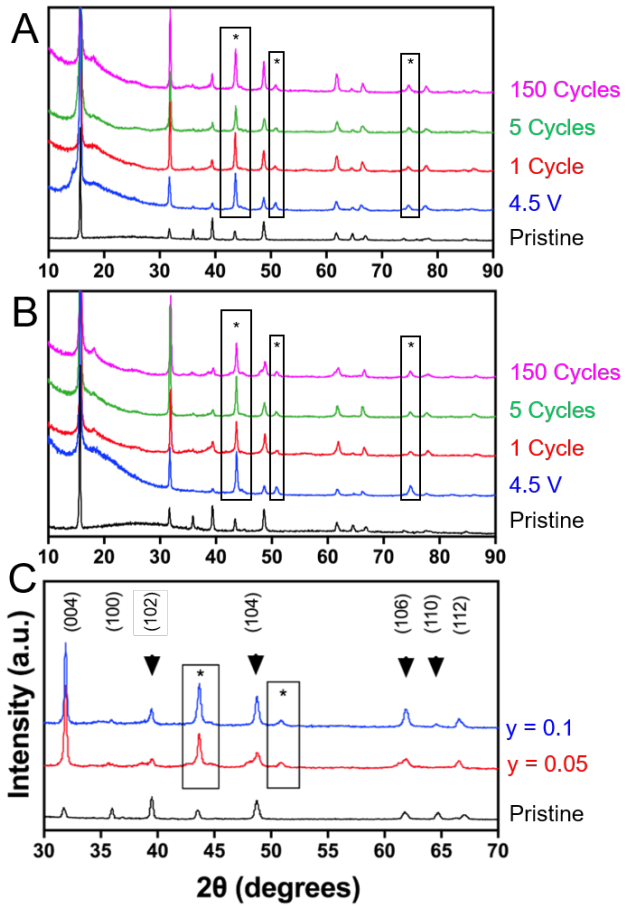


**Figure 24.** *Ex-situ* XRD spectra of $Na_{2/3}Mn_{1-y}Mg_yO_2$ at various stages of cycling between 2 – 4.5 V. '*' marks peaks from the stainless steel current collector. A) y = 0.1, B) y = 0.05, C) Comparison between both compositions after 150 cycles.

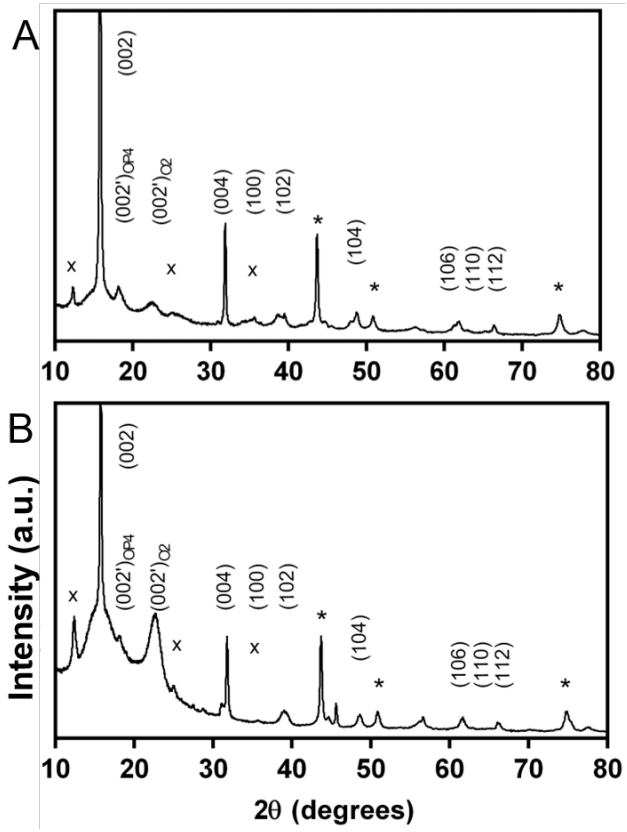


**Figure 25.** *Ex-situ* XRD spectra of $Na_{2/3}Mn_{0.95}Mg_{0.05}O_2$ A) after 150 cycles between 2 – 4.6 V and B) after 100 cycles between 2 – 4.7 V.

## 4.4. Conclusions

P2-$Na_{2/3}Mn_{1-y}Mg_yO_2$ was synthesized using a modified Pechini method at various Mg content (y = 0, 0.5, and 0.1) and the electrochemical performance was characterized at various upper cut-off voltages (4.5, 4.6, and 4.7 V). $Na_{2/3}Mn_{0.95}Mg_{0.05}O_2$ displayed a similar initial discharge capacity compared to $Na_{2/3}MnO_2$ with significantly improved cycle retention, due to suppressed $Na^+$/vacancy ordering, Jahn-Teller distortion, and high-voltage phase transitions. $Na_{2/3}Mn_{0.9}Mg_{0.1}O_2$ showcased an improvement in cycle retention and rate capability, albeit with lower discharge capacity. *Ex-situ* XRD characterization revealed that both $Na_{2/3}Mn_{0.95}Mg_{0.05}O_2$ and $Na_{2/3}Mn_{0.9}Mg_{0.1}O_2$ retained their pristine P2 structure after extensive cycling from 2 – 4.5 V.

The small differences in cycle retention was ascribed the formation of stacking faults and microstrains, leading to peak broadening. At 4.6 and 4.7 V cut-offs, electrolyte insertion into the metal oxide slabs, excessive electrolyte decomposition, irreversible octahedral-related phase transitions, and active material dissolution (at 4.7 V) were major factors of irreversible capacity loss. The extraordinarily high discharge capacity of P2-$Na_{2/3}Mn_{1-y}Mg_yO_2$ when cycled at high voltage cut-offs makes it a promising cathode material for sodium-ion battery application, with opportunities to further improve its cyclability through strategies such as surface coatings, forming nanostructured composites, and using ionic liquid electrolyte.

# 5. $Na_2CoPO_4F$ as a Pseudocapacitive Anode for High-Performance and Ultrastable Hybrid Sodium-Ion Capacitors

## 5.1. Introduction

Hybrid-ion capacitors (HICs) are designed to bridge the features of metal-ion batteries and electric double-layer capacitors (EDLCs).[53] Typically comprised of an insertion electrode and a carbonaceous capacitive electrode in an organic (carbonate-based) electrolyte, HICs can deliver 3-4 times the energy density compared of EDLCs albeit with lower rate performance and cycle stability.[53] HICs use either lithium or sodium-based salts as charge carriers, with these devices termed lithium-ion capacitors (LICs) and sodium-ion capacitors (NICs), respectively. The operating mechanism of the device relies on the intercalation/deintercalation of $Na^+$/$Li^+$ with the insertion electrode while the energy storage on the capacitive electrode relies on the formation of an electric double layer through the adsorption/desorption of counter-ions (*e.g.,* $ClO_4^-$ and $PF_6^-$) at the electrode-electrolyte interface.[54] The insertion electrode contributes to the HIC energy density as it can store charge through redox pseudocapacitive (surface) and intercalation (bulk) processes, while non-Faradaic processes on the carbonaceous electrode are responsible for delivering high power density. However, the main disadvantage of this system is the mismatched kinetics between the sluggish intercalation mechanism and capacitive charge storage, resulting in poor rate performance.[54] Thus, the design, preparation, and improvement of novel insertion electrodes to match suitable capacitive electrodes is urgently required in order for HICs to be competitive in the secondary energy storage market.

A large variety of insertion electrodes for HICs have been explored and developed in the literature, such as titania-based compounds,[55,56] carbonaceous electrodes,[57] and transition metal oxides used

as intercalation cathodes in metal-ion batteries.[58–60] Some HIC systems reported recently demonstrate an impressive energy density (upper range of 60 – 80 Wh $kg^{-1}$, normalized by active material mass), narrowing the gap in energy storage capabilities with batteries.[53] However, the vast majority of HICs still display relatively poor cycle stability and rate capability. For instance, HICs containing titania-based insertion electrodes are desired due to their structural stability and have been optimized using nanostructuring, heteroatom doping, and carbon coating approaches in order to improve their conductivity and rate performance, but most reports demonstrate relatively poor long-term cycle stability.[53] Cycle retention loss is therefore ascribed to solid-electrolyte interphase (SEI) layer buildup and dissolution of active materials on the anode due to voltage polarization.[107] Carbonaceous insertion electrodes (*e.g.,* hard carbon[108]) are attractive due to their ecofriendly and inexpensive composition; however, they generally showcase poor cyclability and rate performance. Cycle stability is a particularly important benchmark for HICs as their proposed applications (*e.g.,* regenerative breaking) are similar to that of supercapacitors.[53] However, while commercial supercapacitors are stable over 100,000 charge-discharge cycles, few reports in the literature on HICs demonstrate a capacity retention ≥90% over 10,000 cycles.[109–113]

While LICs have been more extensively studied, NICs are an emerging technology with its development motivated by the uneven global distribution of lithium reserves, which may cause price spikes for raw lithium materials as the demand for lithium-based batteries increases.[9] However, limited high-performance $Na^+$ intercalation electrodes are available due to stability issues associated with the larger ionic radius of $Na^+$ compared to $Li^+$ (0.102 nm vs 0.076 nm). Intercalation/deintercalation of $Na^+$ is kinetically sluggish and causes irreversible structural deformation, especially at high voltage windows. However, numerous NICs have been reported

which are competitive with and even exceed the performance of most LICs in the literature.[109,114,115] This is because in addition to bulk intercalation processes, some NIC insertion electrodes possess a significant amount of pseudocapacitive charge storage contributions, which are kinetically facile and stable.[116,117] Hence, NIC technology has a promising outlook, but more work must be devoted to developing high-performance electrode materials for NICs that can deliver high energy and power density without sacrificing its cycle life.

Future energy demands require an electrode that can deliver high capacity, energy density, and high operating voltages. In this regard, sodium fluorophosphate materials ($Na_2MPO_4F$, M = Mn, Ni, Fe and Co) have been proposed as potential cathode materials for NIBs.[69,118–121] These materials have a higher operating voltage than layered cathodes, due to the higher ionicity of the M-F bond compared to M-O.[122] Moreover, the highly electronegative $F^-$ anion can charge compensate for the additional $Na^+$ and provide stability at high cut-off voltages.[123] They also have a high theoretical discharge capacity (>250 mAh $g^{-1}$) assuming both $Na^+$ are extracted from the structure. Among the sodium fluorophosphates, $Na_2CoPO_4F$ (NCPF) has displayed a high energy density (525 Wh $kg^{-1}$) with a discharge plateau near 4.3 V (*vs* $Na/Na^+$).[69,118] Few reports are available on the performance of $Na_2MPO_4F$ in half cell configuration with sodium metal anodes in organic electrolyte.[69,118–121] These materials showed poor cycle performance and delivered low practical capacity, demonstrating that extensive studies are required to utilize metal fluorophosphates in battery applications. However, due to the exceptionally wide operating voltage range of NCPF, we chose to assess its suitability as an insertion electrode for NICs.

In this work, we demonstrate the use of NCPF as an insertion electrode for NICs for the first time. We adopt a novel two-step synthesis technique to develop NCPF for both NIB and NIC applications. Our synthesized NCPF demonstrates promising cycle retention at the cathodic (2 – 5 V) and anodic (0 – 3 V) regions using a sodium half-cell configuration, although the initial discharge capacities were only partially reversible. The charge storage mechanism at the anodic region was primarily pseudocapacitive. Hence, an NCPF//AC NIC was assembled for the first time using NCPF as the anode and AC as the cathode. The resulting performance was remarkable in terms of cyclic life (over 100,000 cycles) and power output, which outperforms most LICs and NICs reported in the literature.

## 5.2. Experimental

### 5.2.1. Synthesis of NCPF

Nano-sized NCPF powders were prepared by a two-step method. Initially, $NaCoPO_4$ (NCP) nanoparticles were synthesized using a citric acid assisted sol-gel method. Stoichiometric amounts of sodium acetate trihydrate (Sigma-Aldrich, Mississauga, Canada), cobalt(II) acetate tetrahydrate (Sigma-Aldrich), and ammonium phosphate dibasic (Sigma-Aldrich) were dissolved in deionized water with citric acid (Sigma-Aldrich) and stirred at 110˚C. The molar ratio of metal ions to citric acid was fixed at 1:3. After evaporating excess water, the obtained gel precursor was decomposed at 400˚C for 4 h to remove organic and ammonium moieties. The final calcination was performed at 800˚C for 10 h in air to form NCP. To obtain NCPF, the NCP powder was ground with sodium fluoride (Sigma-Aldrich) using a mortar and pestle, then calcined at 750˚C for 1.5 h under Ar flow, and immediately quenched to room temperature in air. The resultant NCPF was ground to a fine

powder and stored in a vacuum oven. AC with a surface area of 1700 $m^2$ $g^{-1}$ was purchased from Wako Chemicals (Japan) and used as received.

### 5.2.2. Physical and Chemical Characterization of NCPF

The phase purity of the pristine NCPF active material was assessed using powder X-ray diffraction (XRD, XRDMiniflex 600, Rigaku, Japan) with Cu $K_\alpha$ radiation ($\lambda$ = 1.5406 nm) at a scan rate of 0.1 º/min. Rietveld refinement was conducted on MAUD software[81] while the crystal lattice structure was generated using VESTA.[124] The morphology of the particles was observed with scanning electron microscopy (SEM, LEO Zeiss 1550, Switzerland) using a 20 kV acceleration voltage and a working distance between 8 – 9 mm coupled with energy-dispersive X-ray spectroscopy (EDX). Prior to imaging, the particles were sputtered with ~5 nm of gold. The valence state of the metal ions in NCPF were determined by X-ray photoelectron spectroscopy (XPS, Thermo Scientific Theta Probe, Waltham, MA, USA) using Al $K_\alpha$ radiation. The binding energies reported are referenced to graphitic carbon at 284.8 eV. Thermogravimetric analysis (TGA, TA Instruments Q500, Grimsby, Canada) was conducted from 0 to 800 ºC at a ramp rate of 5 ºC/min to detect the presence of a carbon coating. Surface area measurements were conducted by Brunauer-Emmett-Teller (BET) analysis using $N_2$ adsorption (Gemini VII, Micromeritics, Norcross, GA, USA).

### 5.2.3. Preparation of NCPF and AC Electrodes

The electrode was prepared by grinding a slurry of 70 wt% active material (NCPF or AC), 20 wt% conductive carbon black (Ketjenblack, Lion Specialty Chemical Co., Japan), and 10 wt% Teflonized acetylene black binder in ethanol using a mortar and pestle. The electrode film was

pressed (~8,000 kPa) onto a 15 mm diameter stainless steel mesh and dried overnight at 80˚C in a vacuum oven. The mass loading for the active material was 6 mg $cm^{-2}$. In order to assemble the NIC, a 1:1 weight ratio of NCPF:AC active material was used.

### 5.2.4. Electrochemical Characterization of NIC and Electrode Half Cells

The electrochemical performance of the NCPF electrode was assessed by assembling CR2032 coin cells in an Ar-filled glove box ($O_2$ and $H_2O$ < 0.5 ppm, MBRAUN, Stratham, NH, USA) using a pure sodium foil as the counter electrode, a polypropylene separator (Celgard 2400, Charlotte, NC, USA), and an electrolyte comprised of 1 M $NaClO_4$ dissolved in 1:1 ethylene carbonate:diethyl carbonate (Sigma-Aldrich, 1:1 v/v). NIC cells were constructed as described above using NCPF as the anode and commercial AC (Sigma-Aldrich) as the cathode. Cyclic voltammetry (CV) and electrochemical impedance spectroscopy (EIS) curves were acquired using a Gamry Instruments potentiostat (Warminster, PA, USA). EIS measurements were conducted from 1 MHz to 100 mHz at discharged state. Long-term galvanostatic charge-discharge studies and rate performance tests were carried out at ambient temperature using a CT2001A LAND battery testing system (Wuhan, China). After long-term cycling, the coin cell was disassembled in a glove box, and the NCPF electrode was washed in ethylene carbonate, dried in a vacuum oven, and subsequently characterized via XRD, XPS, and EDX.

The cell capacitance ($C_{cell}$) of the NIC was calculated from the charge-discharge curves using Eq. 1:

$$C_{cell} = \frac{it}{\Delta V} \quad (1)$$

where $i$ is the current (A), $t$ is the discharge time (s), and ΔV is the voltage range (V). The specific discharge capacitance ($C_{dc}$) was then obtained using Eq. 2:

$$C_{dc} = \frac{4C_{cell}}{m} \quad (2)$$

where $m$ is the total mass of the anode and cathode active materials. The energy ($E_D$, Wh $kg^{-1}$) and power density ($P_D$, W $kg^{-1}$) were then obtained from $C_{cell}$ using Eqs. 3 and 4 respectively:

$$E_D = \frac{1}{2}\frac{C_{cell}\Delta V^2}{3.6} \quad (3)$$

$$P_D = \frac{E_D \times 3600}{t} \quad (4)$$

## 5.3. Results and Discussion

### 5.3.1. Physical Characterization of Synthesized NCPF

NCPF was synthesized by a two-step process for the first time, where $NaCoPO_4$ (NCP) was first formed through a citric-acid assisted sol-gel method. The XRD pattern of NCP indicates that the structure matches the α-polymorph indexed to the *Pnma* space group with lattice parameters $a$ = 8.880, $b$ = 6.799, $c$ = 5.035 (Figure 26A), which comprises octahedrally coordinated Na and Co atoms, and P tetrahedra (Figure 26B).[125] NCP was then reacted with NaF through a conventional solid-state method to generate NCPF.

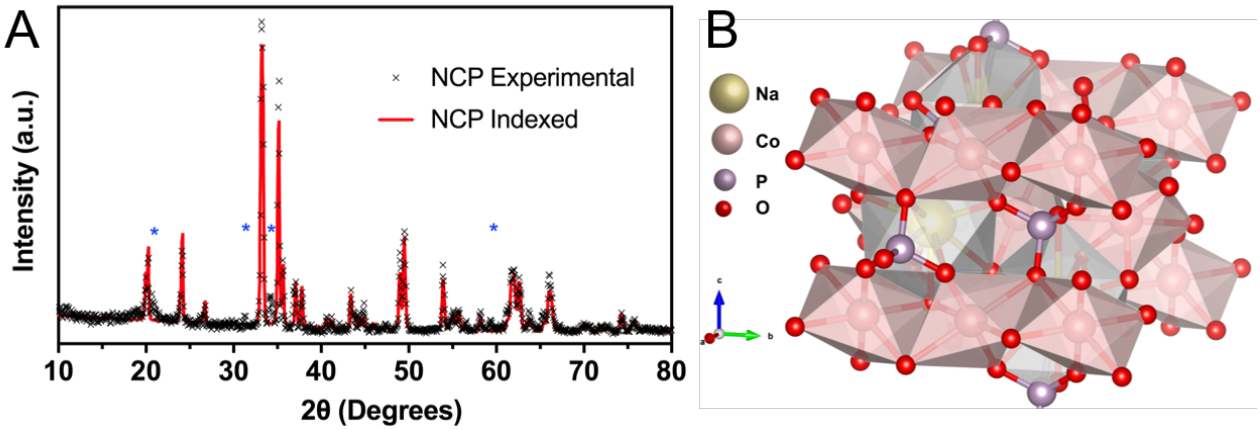


**Figure 26.** A) XRD pattern of synthesized NCP. The NCP data used for indexing was based on COD ID: 2101516. Impurity peak positions are labelled (*) and correspond with excess sodium phosphate. B) Lattice structure of NCP generated using VESTA.

SEM images of the synthesized NCPF powder show large primary particles with an average size of 10 μm (Figure 27A) and at higher magnifications (Figure 27B), nanometer-scale secondary particles are evident. This morphology is expected to increase the surface area of contact with the electrolyte, thus reducing the diffusion path of $Na^+$ and enhancing electrochemical performance.[85] Indeed, the BET surface area was measured as 6.3 $m^2$ $g^{-1}$, which is higher than typical transition metal oxide electrode powders.[126] The high surface area can also be explained by the decomposition of citric acid among the NCP particles during calcination, which evolves CO and $CO_2$ gases and thus forms void spaces within the particles.[127] Although citric acid and acetate precursor was used, no carbon coating was present on the final NCPF particles following calcination, according to TGA measurements (data not shown). The powder XRD pattern (Figure 27C) indicates that the NCPF has an orthorhombic structure indexed to the *Pbcn* space group with the lattice parameters $a$ = 5.2415 Å, $b$ = 13.7823 Å, and $c$ = 11.6814 Å calculated from a Rietveld refinement, corresponding with previous reports.[69,118,119] As seen in Figure 27D, the structure is

comprised of layers built from $PO_4$ tetrahedral and $Co_2O_7F_2$ bi-octahedral units, and $Na^+$ located in the interlayer space.[119]

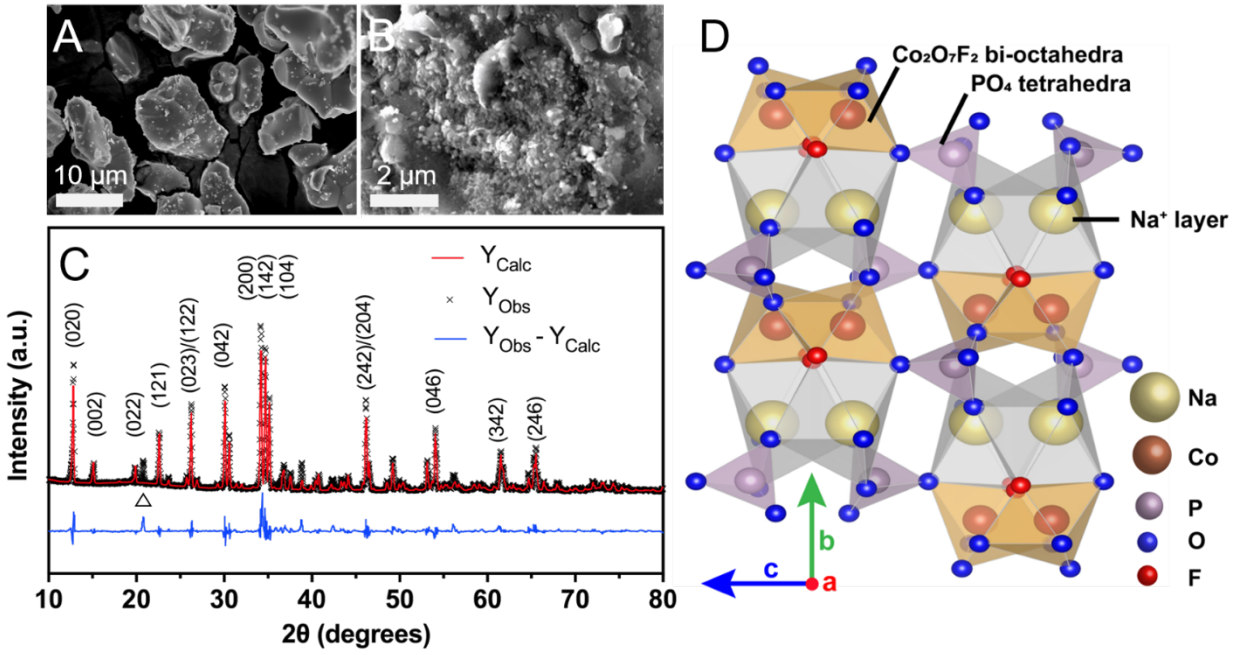


**Figure 27.** Powder NCPF Characterization. A and B) SEM images of particles. C) XRD pattern with Rietveld Refinement ($R_{wp}$ = 13.2%). Δ marks location of impurity peak likely from excess sodium phosphate.[128] D) Unit cell of NCPF lattice.

The high-resolution XPS spectra of the Na 1s, Co 2p, P 2p, O 1s, and F 1s subshells of pristine NCPF is shown in Figure 28. The Na 1s photoemission spectra (Figure 28B) shows a peak centered at 1070.81 eV, which is in good agreement with tabulated values for Na-phosphate compounds (*e.g.,* $Na_4P_2O_7$ at 1070.8 eV[129]). The broad and slightly asymmetric appearance of the spectra is likely due to the fact that NCPF contains two energetically inequivalent Na sites (denoted Na1 and Na2) that are difficult to distinguish as the binding energy difference is small.[130] This was similarly observed in $Na_2FePO_4F$[131] and $Li_2CoPO_4F$.[132] The Co 2p region (Figure 28C) shows binding energies of 780.76 and 796.92 eV for the $2p_{3/2}$ and $2p_{1/2}$ multiplets respectively (orbital splitting

of 16.2 eV) that each possess satellite peaks at 785.83 and 803.07 eV, which is characteristic of a +2 valence state.[133] It is worth mentioning that the NCPF Co $2p_{3/2}$ binding energy is upshifted compared to our synthesized $NaCoPO_4$ (780.32 eV). This is likely due to the presence of Co-F bonds, which possess a higher bond ionicity compared to Co-O.[134] The P 2p binding energy at 132.97 eV (Figure 28D) corresponds to a +5 valence state, while O 1s at 530.57 eV (Figure 28E) is similar to the values of $Na_3PO_4$ (530.4 eV) and CoO (530.1 eV). Like Na, F is located in two energetically inequivalent sites. The F 1s spectra (Figure 28F) displays a broad and asymmetric appearance that is deconvoluted to reveal two peaks at 684.30 and 686.36 eV, which can be indexed to Na-F and Co-F bonds respectively.[129] The elemental composition of the synthesized NCPF was confirmed using EDX, revealing a Na:Co:P:O:F atomic ratio of 1.92:0.98:1.02:4.24:1 (Figure 29). These characterizations confirm the successful synthesis of carbon-free NCPF.

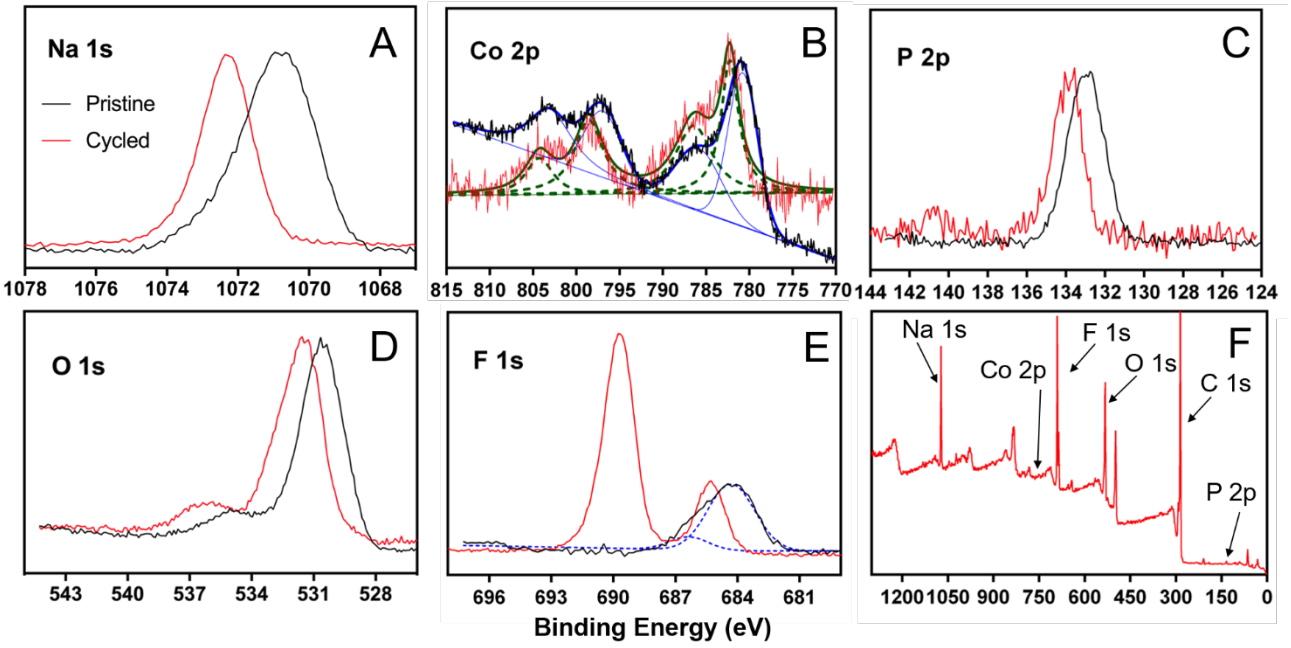


**Figure 28.** High-resolution XPS spectra of pristine (black curve) and cycled (red curve) NCPF elements. Peak deconvolution for Co 2p (pristine and cycled) and F 1s (pristine) is shown.

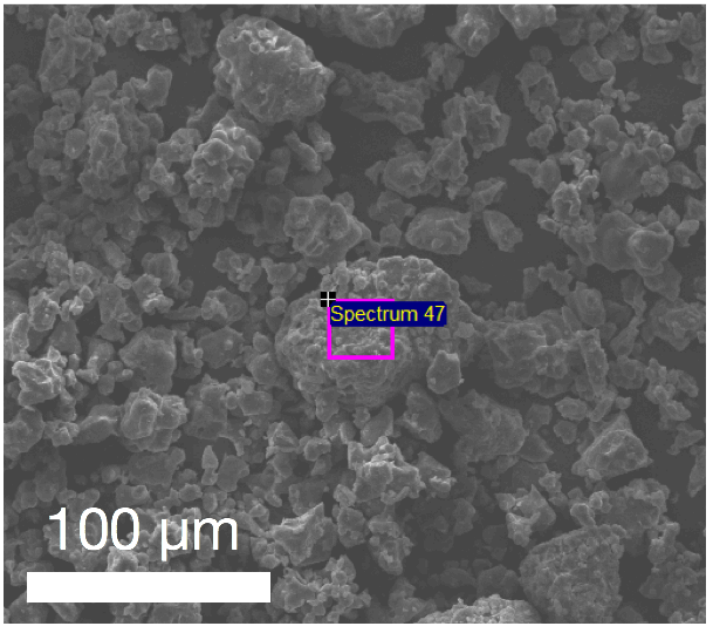


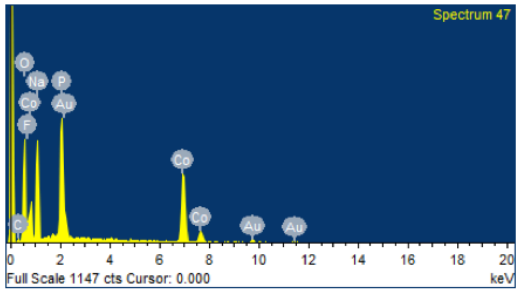


| Element | Atomic Ratio |
|---|---|
| Na | 1.95 |
| Co | 0.98 |
| P | 1.02 |
| O | 4.24 |
| F | 1 |

**Figure 29.** EDX spectra of synthesized NCPF powder.

### 5.3.2. Electrochemical characterization of NCPF

The electrochemical performance of NCPF was first assessed by assembling half cells using sodium foil as the counter electrode. Due to the lack of published reports on NCPF, our half-cell performance at the anodic (0 – 3 V *vs* $Na/Na^+$) and cathodic (2 – 5 V *vs* $Na/Na^+$) region is shown in detail in Figure 30 and Figure 31, respectively. At the anodic region (0 – 3 V *vs* $Na/Na^+$), galvanostatic charge-discharge data show that the Na/NCPF cell has an initial discharge capacity of 130 mAh $g^{-1}$ at 17 mA $g^{-1}$ (0.13 C), with significant irreversible capacity loss in subsequent cycles, likely due to lattice structural changes and formation of a passivating SEI layer. Figure 32 displays the *ex-situ* XRD pattern, which reveals significant peak broadening associated with structural defects over the first 20 cycles. The initial discharge curves (Figure 30A) show a plateau at ~1.1 V, likely associated with $Na^+$ insertion, which resulted in capacity decay and structural evolution that was observed over the preliminary cycles. However, reasonable capacity retention was maintained after 40 cycles, stabilizing at ~50 mAh $g^{-1}$ (Figure 30B). Following the irreversible

capacity loss, CV curves (Figure 30C) show no defined peaks in the 0 – 3 V region. The featureless appearance of the CV curves resembles reports on amorphous pseudocapacitive materials such as $MoO_3$[135] and $Nb_2O_5$.[116] As the electric double-layer charge storage contribution from NCPF is considered to be negligible due to its low specific surface area, this suggests that the charge-storage mechanism is primarily based on redox pseudocapacitance on the surface of the active material. To examine this further, CV was conducted at various potential sweep rates (ν) and the current response (*i*) was analyzed. At the anodic peak potential (~0.75 V), the *b*-parameter (based on the relationship $i = a\nu^b$) was calculated as 1 (Figure 30C inset), which is characteristic of a capacitive behaviour. Taken together, this suggests that the charge storage occurs within a single phase material and is not primarily based on diffusion-limited intercalation.[135,136]

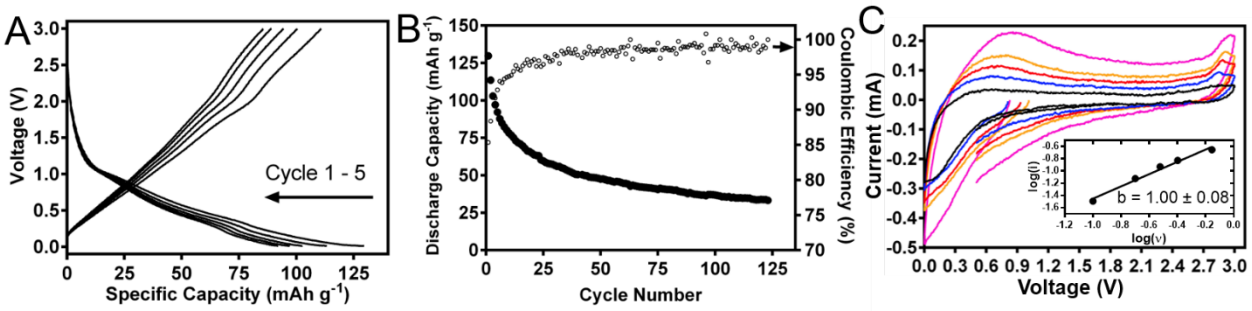


**Figure 30.** Galvanostatic half-cell characterization of NCPF anode cycled from 0 – 3 V vs $Na/Na^+$ at 22 mA $g^{-1}$ current. A) First five charge-discharge curves. B) Discharge capacity retention through 120 cycles. C) CV curves measured with various sweep rates (ν) from 0.1 – 0.7 mV $s^{-1}$.

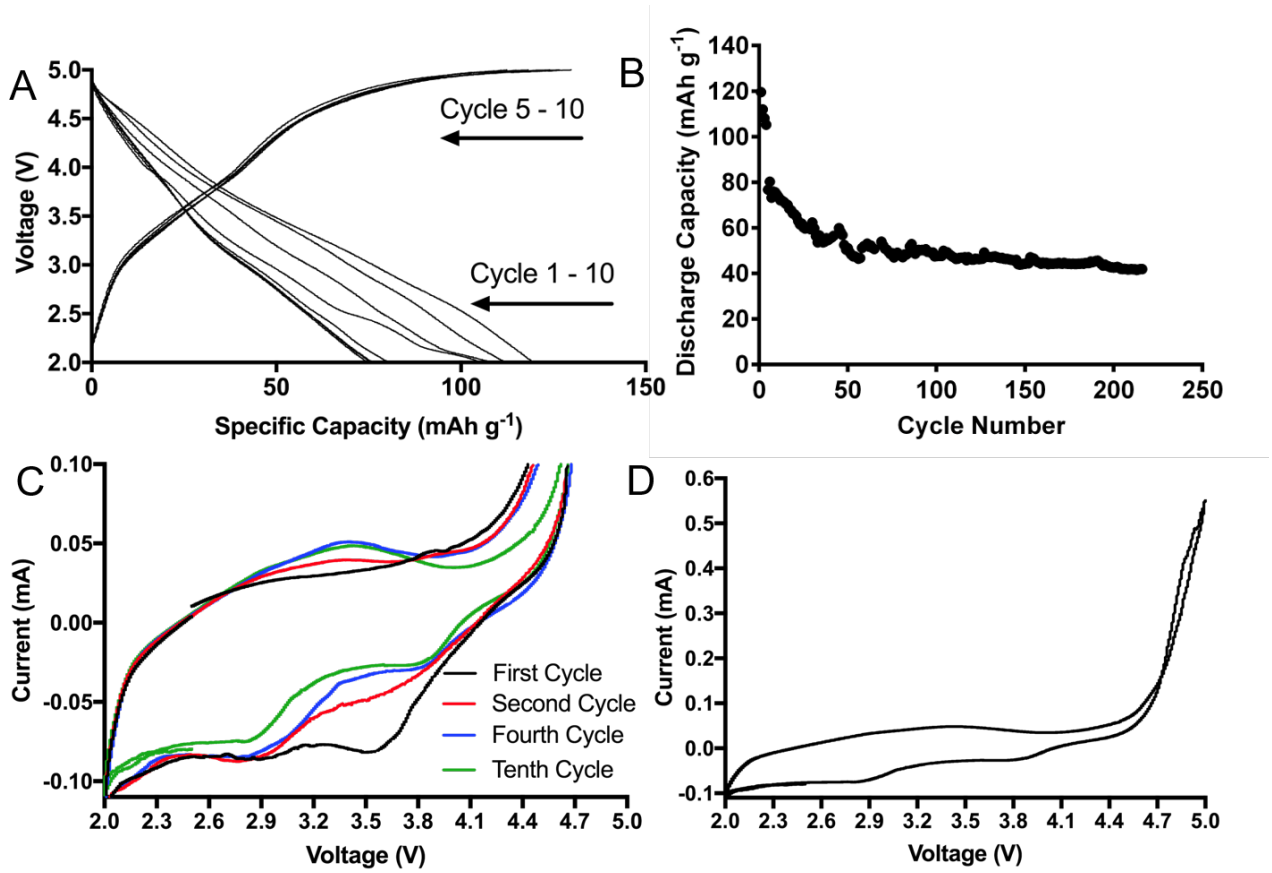


**Figure 31.** NCPF half-cell electrochemical performance. A) Initial charge-discharge curves and B) cycle stability from 2 – 5 V at 17 mA $g^{-1}$. C) CV curves conducted at 0.1 mV $s^{-1}$ enlarged from 2 – 4.7 V. D) CV curve ($10^{th}$ cycle) from 2 – 5 V.

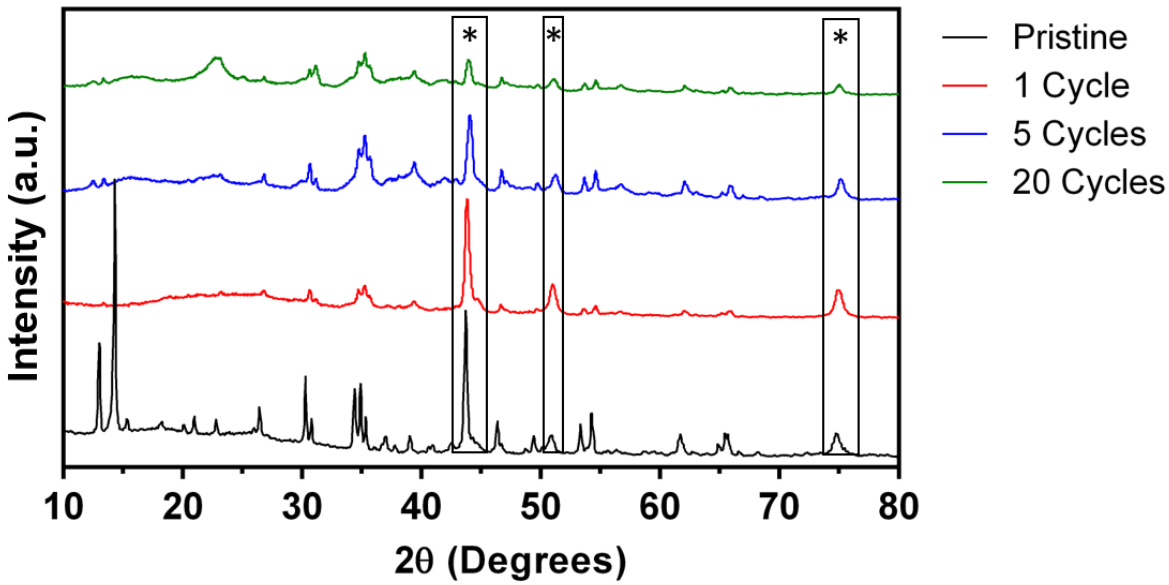


**Figure 32.** *Ex-situ* XRD pattern of NCPF cycled as Na/NCPF half-cell from 0 – 3 V at 17 mA $g^{-1}$. Symbol (*) marks peaks from the stainless steel current collector.

At the cathodic region (2 – 5 V *vs* $Na/Na^+$), an initial discharge capacity of 120 mAh $g^{-1}$ at 22 mA $g^{-1}$ (0.18 C) was obtained with subsequent irreversible capacity loss until it stabilized at ~50 mAh $g^{-1}$ after 50 cycles (Figure 31A). A discharge capacity of 42 mAh $g^{-1}$ was retained after 200 cycles. It should be noted this cycle stability is remarkable for such a high voltage cut-off compared to other NCPF reports.[69,118] For instance, NCPF synthesized by Zou *et al*. displayed an initial discharge capacity of 107 mAh $g^{-1}$ at 61 mA $g^{-1}$ and decayed rapidly to 40 mAh $g^{-1}$ after 20 cycles.[69] CV curves (Figure 31C) show a small anodic peak at ~3.9 V and a broad cathodic peak at ~3.6 V during the first cycle associated with the $Co^{2+}/Co^{3+}$ redox. Subsequent cycles display a broad anodic peak at ~3.4 V and two cathodic peaks at ~2.8 V and ~3.8 V. This implies significant structural changes during the initial cycling, where the two cathodic peaks represent $Na^+$ insertion sites of different local environments.[137] It should be noted that the discharge curves appear different compared to previous reports on NCPF due to the lack of a distinct discharge plateau at ~4.3 V for the $Co^{2+}/Co^{3+}$ redox reaction.[69,118] This difference can be ascribed to the unique synthesis approach in this work. As mentioned, we used a two-step method where $NaCoPO_4$ was first synthesized by a conventional sol-gel method, followed by a solid-state reaction with NaF. The sloping appearance of the discharge curve resembles that of $NaCoPO_4$, suggesting that the difference is associated with the distribution of F atoms in the structure.[137] This helps explain the lower onset potential of the $Co^{2+}/Co^{3+}$ redox reaction. However, this was not distinguished in the powder characterization so the exact mechanisms are a subject for future exploration. The coulombic efficiency was low (≤ 80%) throughout cycling, which is commonly observed due to accelerated decomposition of the carbonate-based electrolyte at high cut-off potentials.[126] Based

on the half-cell electrochemical data, NCPF was chosen as an insertion anode to construct the NIC system along with an AC cathode.

The assembled NCPF//AC NIC was tested at two potential ranges (0 – 3 V and 0 – 3.25 V) at various current densities using 1 M $NaClO_4$ electrolyte. Although a 3 V window is a typical benchmark for HICs, 3.25 V was also explored to expand the energy density of the device. CV curves of the NIC at different scan rates (Figure 33) show characteristic rectangular-like plots that retain their shape from 3 to 50 mV $s^{-1}$, indicating good charge propagation within the electrodes and no noticeable polarization. As seen in Figure 34B, the charge-discharge profiles at various currents deviate slightly from triangular curves observed in ideal supercapacitors, due to the combination of Faradaic and non-Faradaic charge-storage processes.

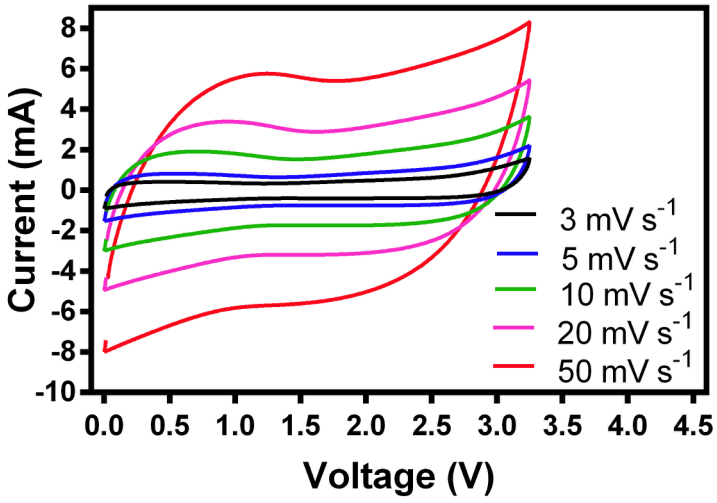


**Figure 33.** CV curves of assembled NCPF//AC cell at various sweep rates from 0 – 3.25 V.

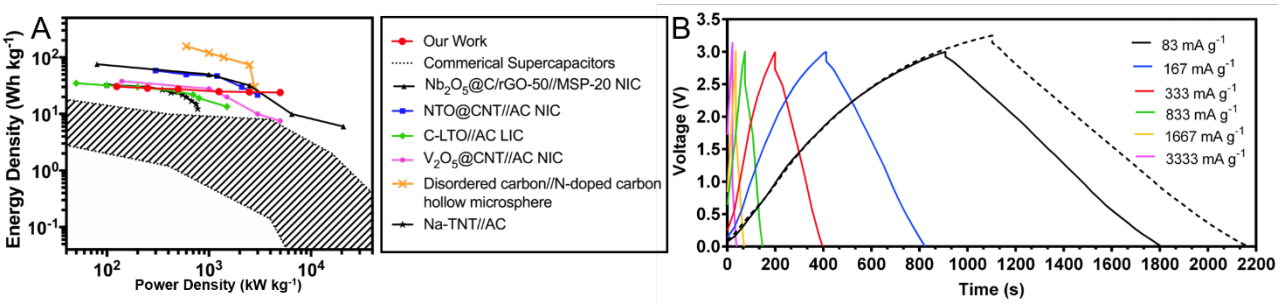


**Figure 34.** Rate performance of NCPF//AC NIC cycled from 0 – 3 V. A) Ragone plot comparison of our NCPF//AC system with notable HICs in the literature[117,138–142] and commercial supercapacitors.[52]

The expected reaction mechanism in the cell is shown in the Eqs. 5 and 6 below:

$$\text{Anode: } Na_2CoPO_4F \text{ (Surface)} \rightleftharpoons Na_{2-x}CoPO_4F + xe^- + xNa^+ \quad (5)$$

$$\text{Cathode: AC} + xe^- + //xClO_4^- \rightleftharpoons \text{AC } (xe^-) \text{ (// stands for double layer)} \quad (6)$$

During charging, Na-ions adsorb on the surface of NCPF where they are reduced. To relieve the charge imbalance, $ClO_4^-$ ions simultaneously adsorb onto the surface of AC to form an electric double-layer. During discharge, the reverse occurs where $Na^+$ is released into the electrolyte and $ClO_4^-$ quickly desorbs from AC.

The assembled NICs were initially cycled at 83 mA $g^{-1}$ (pre-cycling) until the cell capacitance stabilized after ~200 cycles with a ~60% loss of the initial capacitance. Following pre-cycling, the rate performance was assessed from 0 – 3 V at current densities of 83, 167, 333, 833, 1667, and 3333 mA $g^{-1}$. A Ragone plot (Figure 34A) was generated by averaging the energy density calculated at each current over 125 cycles. The NCPF//AC system retained 78% of its energy density from 125 to 5,000 W $kg^{-1}$. At low currents, the energy density of the NCPF//AC device is

higher than commercial supercapacitors but lower than HICs recently reported in the literature. However, the energy density surpasses most HICs at high currents (24 Wh $kg^{-1}$ at 5 kW $kg^{-1}$). Figure 3B displays the initial charge-discharge curves at these currents, where it is clear that the voltage (IR) drop at the charge-discharge transition is unpronounced even at high currents, indicating a low device internal resistance. As long-term cycle retention is critical for the commercial development of HICs, this was then assessed from 0 – 3 V at 250 mA $g^{-1}$, displaying an initial specific capacitance at 90 F $g^{-1}$ (28 Wh $kg^{-1}$) with a retention of 94% over 10,000 cycles. The cycle performance was extended at higher current with little comprise in energy density due to the excellent rate performance. At 667 mA $g^{-1}$, the NCPF//AC NIC retained ~93% of its initial capacitance (corresponding to 24 Wh $kg^{-1}$) after 100,000 cycles (Figure 35A). This stability is among the highest ever reported for HICs (*i.e.,* both LICs and NICs) as compared in Table 5. Figure 35B displays the charge-discharge curves during the initial (following pre-cycling) and final cycles of this sample. The shapes of the curves appear were well retained, and the voltage drop at the charge-discharge transition appeared consistent, suggesting minimal changes in internal resistance of the device throughout cycling. In the interest of expanding the energy density, the cyclability from 0 – 3.25 V was assessed. The cell displayed an initial capacitance of 96 F $g^{-1}$ (35 Wh $kg^{-1}$) and remarkably, 88% of the capacitance was retained after 10,000 cycles at 250 mA $g^{-1}$, eventually decaying to 80% after 30,000 cycles (Figure 35D). This is among the highest stability ever reported for a voltage window >3 V (Table 5). It should be noted that despite the poorer stability at a 3.25 V window, the energy density after 10,000 cycles (29 Wh $kg^{-1}$) still exceeded that of the 3 V window sample (26 Wh $kg^{-1}$) at 250 mA $g^{-1}$.

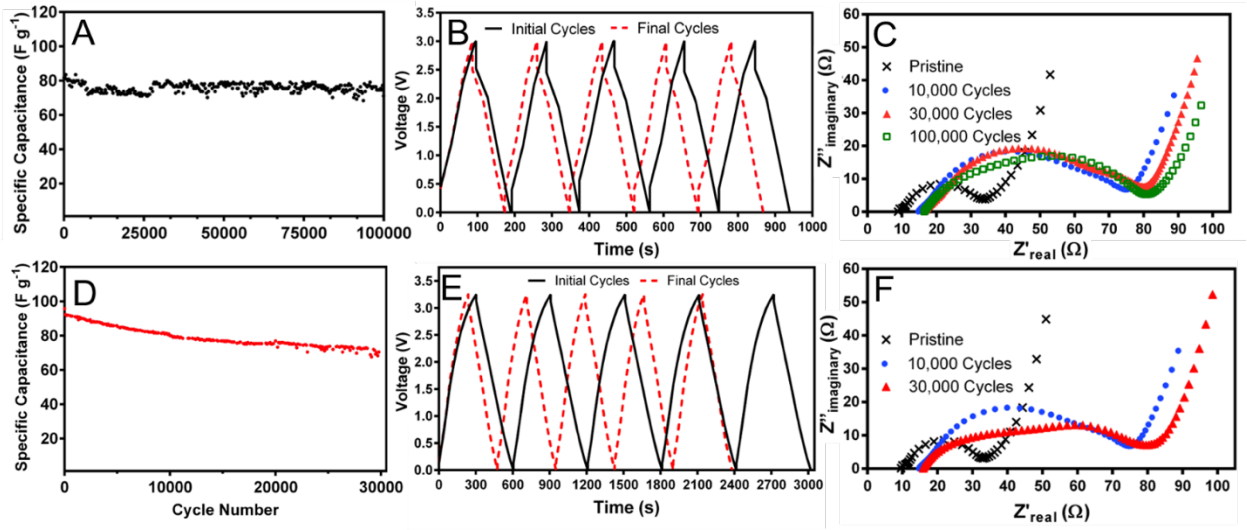


**Figure 35.** Electrochemical performance of NCPF//AC NIC. Long-term cycle stability (A and D), initial (black solid) and final (red dotted) charge-discharge curves (B and E), and EIS spectra (C and F) of samples cycled from: A-C) 0 – 3 V at 667 mA $g^{-1}$ and D-F) 0 – 3.25 V at 250 mA $g^{-1}$.

It is typically observed in HICs that at higher charge-discharge rates, ion diffusion into the pores of active materials is reduced, and thus the charge storage mechanism is primarily dictated by surface phenomena as opposed to bulk processes.[110] Thus, cyclability is improved at higher current, as bulk processes can cause lattice strain in the insertion anode, resulting in irreversible capacity loss. This was clearly observed in our long-term cycling results when comparing the samples cycled from 0 – 3 V at 250 mA $g^{-1}$ *vs* 667 mA $g^{-1}$. However, due to the loss of bulk charge-storage contributions, the energy density should decrease at high rates. The fact that our NIC system displays an excellent rate performance supports our earlier observations that the charge storage mechanism in NCPF when functioning as an anode is mostly pseudocapacitive, and thus its kinetics can match the high-rate adsorption cathode. However, it should be noted that the energy density retention and cyclability at high current was poor when tested from 0 – 3.25 V (data not shown). A similar trend was observed in other reports when the voltage window was expanded.[56,143] This is likely caused by voltage polarization effects that become more prevalent at

high currents, resulting in accelerated SEI layer formation at the anode and capacity throttling at the cathode.[107] As discussed, the excellent long-term cyclability and rate performance of the NIC device (Table 5) is ascribed to the pseudocapacitive charge-storage mechanism of the NCPF anode. Charge storage is aided by the nanometer-scale features of the particles that increase the active surface area for redox reactions. Due to the structural evolution and peak broadening of the NCPF lattice structure displayed in the half-cell *ex-situ* XRD pattern in Figure 32, it is inferred that pseudocapacitance accounts for most of the charge-storage mechanism of NCPF in the NIC device after the irreversible capacity losses that occur during the pre-cycling stage. As pseudocapacitance is mostly a surface-controlled reaction, the reversible energy density (at low current) of our NCPF//AC system is relatively low compared to other HICs in the literature.[53] Thus, our future work aims to expand the capacitive contribution of NCPF by generating carbon-composite structures possessing unique hierarchical architectures.[144]

**Table 5.** Comparison of cycle stability of NCPF//AC with notable NICs and LICs in the literature.

| HIC System (Anode//Cathode) | Voltage Range Tested | Cycle Stability |
|---|---|---|
| Our work – NCPF//AC NIC | 0 – 3 V | 93% after 100,000 cycles at 2/3 A $g^{-1}$ |
| Our work – NCPF//AC NIC | 0 – 3.25 V | 80% after 30,000 cycles at 0.25 A $g^{-1}$ |
| $Nb_2O_5$@C/rGO-50//MSP-20 NIC[140] | 1 – 4.3 V | 66% after 3,000 cycles at 1 A $g^{-1}$ |
| $Nb_2O_5$ nanosheets//Peanut shell AC NIC[145] | 1 – 3 V | 80% after 3,000 cycles at 1.28 A $g^{-1}$ |
| PSNC3-800//PSOC-A NIC[108] (carbonaceous electrodes derived from peanut shells) | 1.5 – 4.2 V | 72% after 10,000 cycles at 6.4 A $g^{-1}$ |
| $LiNi_{0.5}Mn_{1.5}O_4$ //AC LIC[58] | 1.5 – 3.25 V | 81% after 3,000 cycles at 1 A $g^{-1}$ |
| $NaTi_2(PO_4)_3$//AC NIC[114] | 0.01 – 2.5 V | ~100% after 20,000 cycles at 5 A $g^{-1}$ |
| $Mo_{0.1}Ti_{0.9}O_2$//AC LIC[56] | 1 – 3 V | 75% after 5,250 cycles at 5 mA $cm^{-2}$ or 3.7 mA $g^{-1}$ |
| $Na_3V_2(PO_4)_3$//AC NIC[110] | 0 – 3 V | 95% after 10,000 cycles at 1.1 mA $cm^{-2}$ |
| $NaTi_2(PO_4)_3$@GNs//GNs NIC[109] | 0 – 3 V | 90% after 75,000 cycles at 4 A $g^{-1}$ |

| | | |
|---|---|---|
| $V_2O_5$@CNT//AC LIC[146] | 0 – 2.7 V | 78% after 10,000 cycles at 30 C or 820 W $kg^{-1}$ |
| TiC//N-doped carbon LIC[147] | 0 – 4.5 V | 82% after 5,000 cycles at 2 A $g^{-1}$ |
| $TiO_2$@Carbon//Nanoporous carbon NIC[113] | 1 – 4 V | 90% after 10,000 cycles at 1 A $g^{-1}$ |
| $Zn_{0.25}V_2O_5$@rGO//Mesoporous carbon NIC[148] | 1 – 3.8 V | 87% after 2000 cycles at 1 A $g^{-1}$ |
| $MoSe_2$@Graphene//AC NIC[149] | 0.5 – 3 V | 81% after 5,000 cycles at 5 A $g^{-1}$ |
| Disodium rhodizonate//Cardamom shell-derived porous carbon NIC[150] | 0 – 3 V | 85% after 10,000 cycles at 4 A $g^{-1}$ |
| $Na_{2/3}Mn_{0.54}Ni_{0.13}Co_{0.13}O_2$-$Al_2O_3$//AC NIC[111] | 0 – 3 V | 98% after 10,000 cycles at 0.35 A $g^{-1}$ |
| PPy@$V_2$O5//AC aqueous hybrid capacitor[112] | 0 – 1.8 V | 95% after 10,000 cycles at 10 C |
| $Co_xNi_{1-x}(OH)_2$@rGO//PPD-rGO aqueous hybrid capacitor[151] | 0 – 1.6 V | ~100% after 20,000 cycles at 20 A $g^{-1}$ |

Figure 35C and 35F show the EIS spectra of the NIC throughout long-term cycling. The spectra possess a semicircle at the high-medium frequency region followed by a straight incline at low frequency, which correspond to the electrode/electrolyte charge-transfer impedance ($R_{ct}$) and Warburg impedance (W) respectively.[152] The high-frequency intercept at $Z'_{real}$ is denoted the bulk impedance ($R_e$) and is a sum of contributions related to the conductivity throughout the electrolyte, electrode, and current collector. When cycling at 3 and 3.25 V windows, both samples show an increase in $R_{ct}$ and $R_e$ after 10,000 cycles, likely due to irreversible phase changes that impede charge transfer kinetics and the initial formation of an electrically insulating SEI layer. Cycling at a 3 V window, the $R_e$ and $R_{ct}$ impedances show minor increases after 30-100,000 cycles, suggesting good stability of the SEI layer and NCPF structure. However, after 30,000 cycles at 3.25 V, a second overlapped semicircle is clearly observed at the high-frequency region (Figure 4F), which is associated with an $Na^+$ diffusion impedance through the SEI layer.[152] This indicates that the carbonate-based liquid electrolyte was not as stable at this voltage window, and excessive

electrolyte decomposition over long-term cycling leading to formation of a thick SEI layer was a factor for cycle retention loss.

After 30,000 cycles between 0 – 3 V at 250 mA $g^{-1}$, the NIC was discharged to 0 V and an *ex-situ* XRD (Figure 36), XPS (Figure 28), and EDX (Figure 37) spectra of the NCPF anode was obtained. The XRD pattern evidently displays low-intensity peaks, but most pristine lattice peaks are observed and crystallinity is remarkably retained compared to the half-cell *ex-situ* pattern shown in Figure 32. As the half-cell characterization was conducted over a wide voltage range (0 – 3 V *vs* $Na/Na^+$), structural degradation can be ascribed to irreversible bulk intercalation processes. However, in NIC configuration, NCPF likely operates in a narrower voltage range that primarily involves pseudocapacitance (*i.e.,* limited $Na^+$ insertion in the interlayer spacing), which explains the structural preservation over long-term cycling. After cycling, the Na 1s (1072.3 eV, Figure 28A) and O 1s (532.52 eV, Figure 28D) XPS spectra appear in disproportionately high intensity and thus are likely associated with SEI layer and electrolyte species deposited on the surface of the electrode (*e.g.,* NaCl, $NaClO_4$, and $Na_2O$).[153] The high-energy F 1s peak (689.8 eV, Figure 28E) is ascribed to the *p*-$CF_2$=$CF_2$ bonds from the Teflon-based binder while the lower energy peak (685.29 eV) may arise from fluoride salts generated from defluorination side reactions with the binder.[134] On the other hand, the Co 2p (Figure 28B) and P 2p (Figure 28C) spectra appear in low intensity (Figure 28F) due to the limited sampling depth of the spectrometer and thus likely correspond to the active material. The Co 2p displays binding energies of 782.25 and 798.55 eV for the $2p_{3/2}$ and $2p_{1/2}$ multiplets respectively (16.05 eV orbital splitting), with respective shoulder peaks at 786.42 and 804.28 eV. The valence state is difficult to ascertain due to the poor resolution of the satellite region – the position and relative intensity of the $2p_{3/2}$ shoulder peak indicates a

$Co^{2+}$ state, while the broad appearance suggests a mixed $Co^{2+}/Co^{3+}$ state.[154] The upshift in binding energies compared to pristine NCPF can be ascribed to structural changes (Figure 36) as well as an increased Co-F bond character due to charge balance and potential $Na^{+}$ rearrangement during the oxidation of $Co^{2+}$.[134] The atomic percent ratio of the active metals Co:P calculated after cycles from the XPS intensities is 1:0.986, indicating stability throughout cycling. In addition, elemental mapping of Co and P (1:0.994 intensity ratio) from EDX (Figure 37) shows that the elements are distributed similarly throughout the electrode. These characterizations confirm the electrochemical and mechanical stability of the NCPF anode over extended cycling, thus showcasing its promise toward next-generation NIC devices.

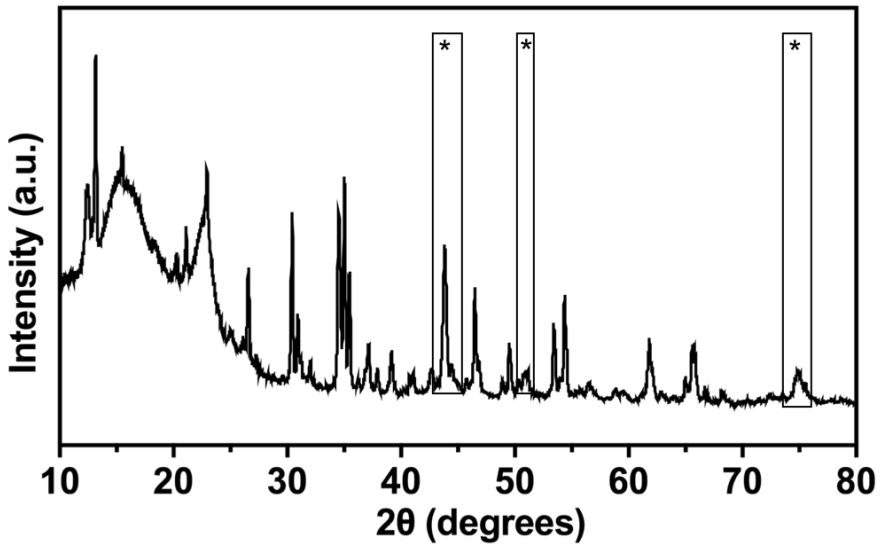


**Figure 36.** *Ex-situ* XRD pattern of NCPF electrode from NCPF//AC NIC cycled from 0 – 3 V at 250 mA $g^{-1}$ after 30,000 cycles. Symbol (*) marks peaks from the stainless steel current collector.

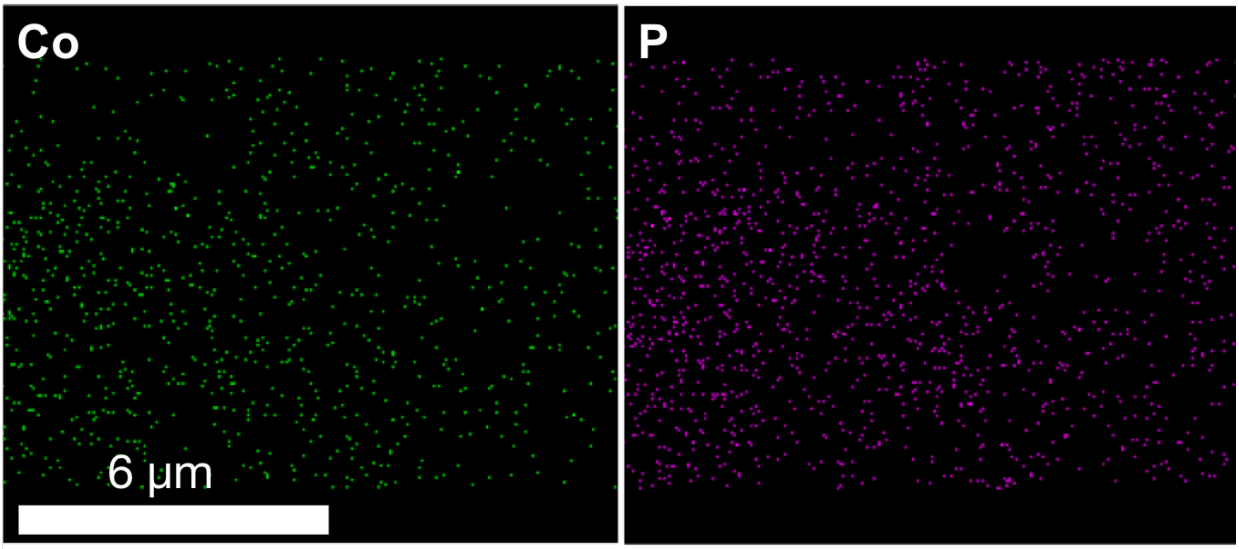


**Figure 37.** *Ex-situ* EDX elemental mapping of NCPF electrode (Co and P) from NCPF//AC NIC cycled from 0 – 3 V at 250 mA $g^{-1}$ after 30,000 cycles.

## 5.4. Conclusions

In this work, NCPF was synthesized using a two-step technique and tested as an NIC anode for the first time. When functioning as an anode, NCPF demonstrated a pseudocapacitive charge-storage mechanism, allowing it to match the facile adsorption-based kinetics of the AC cathode. This resulted in an excellent cycle stability and rate performance when cycled between 0 – 3 V, achieving a 93% capacitance retention over 100,000 cycles and a 78% retention from a 125 to 5,000 W $kg^{-1}$ power output. The energy density of the device was expanded at a voltage range of 0 – 3.25 V and demonstrated good cycle retention at a moderate current density (250 mA $g^{-1}$ or 375 W $kg^{-1}$). At this voltage range, extensive electrolyte decomposition was a notable factor for cycle retention loss. X-ray spectroscopy characterization of the NCPF anode after long-term cycling confirm its electrochemical and mechanical stability. The performance benchmarks with respect to cyclability and power output of our NCPF//AC device are comparable to supercapacitors, while also demonstrating a considerably higher energy density.

# 6. Stabilization of P2-$Na_{2/3}Ni_{0.23}Mn_{2/3}Cu_{0.1}O_2$ Electrode Using Molecular Layer Deposition Coatings

## 6.1. Introduction

In **Section 4**, it was determined that Mg doping of layered P2-$Na_{2/3}Mn_{1-y}Mg_yO_2$ could improve the cycle stability at high cut-off voltages by suppressing the P2-O2 phase transition, Jahn-Teller distortion from $Mn^{3+}$, and $Na^+$/vacancy ordering. While it demonstrated excellent discharge capacities and promising cycle retention, its practicality is ultimately limited due to the low average operating voltage (~2.7 V *vs* $Na/Na^+$). On the other hand, P2-$Na_{2/3}Ni_{1/3}Mn_{2/3}O_2$ is one of the most studied SIB cathode materials and demonstrates a high operating voltage of ~3.6 V *vs* $Na/Na^+$.[155] However, when cycled from 2 – 4.5 V *vs* $Na/Na^+$, the capacity degrades rapidly due to the two-phase P2-O2 phase transition that occurs at ~4.2 V (Na < 1/3). Similarly, the substitution of Ni with various stabilizer cations (including $Mg^{2+}$) can suppress this transition and enhance cycle stability. In this work, P2-$Na_{2/3}Ni_{0.23}Mn_{2/3}Cu_{0.1}O_2$ was explored as Cu can suppress the P2-O2 phase transition while also being redox-active at high voltages. However, substitution of Ni with Cu will lower the theoretical capacity as Cu ($Cu^{2+}/Cu^{3+}$) is less redox active than Ni ($Ni^{2+}/Ni^{4+}$).[156] This work explores the use of titanicone and alucone coatings deposited on the electrodes by molecular layer deposition (MLD) in hopes of further extending the cycle stability. The coating was applied on the electrode surface rather than the active particles due to the contributions of the binder and conductive carbon toward formation of the cathode-electrolyte interface (CEI). In addition, coating the active particles directly could significantly hinder ionic and electronic transport.[157]

In contrast to other coating techniques, MLD can generate highly conformal and ultrathin coatings with thickness control down to ~0.1 nm. Thus, the coating can be optimized to be highly effective while not significantly impeding $Na^+$ diffusion. Moreover, MLD-deposited coatings consume minimal precursor and have negligible mass/volume contributions to the electrode. Compared to metal oxide coatings deposited by ALD (*e.g.,* $TiO_2$ and $Al_2O_3$), the metalcone films are more flexible, mechanically robust, porous, and conductive due to the carbon linkers.

## 6.2. Materials and Methods

### 6.2.1. Synthesis of P2-$Na_{2/3}Ni_{0.23}Mn_{2/3}Cu_{0.1}O_2$

All reagents were purchased from Sigma-Aldrich (Mississauga, Canada) and used as received. P2-$Na_{2/3}Ni_{0.23}Mn_{2/3}Cu_{0.1}O_2$ was synthesized using a modified Pechini method. Here, the appropriate stoichiometric ratios of sodium acetate (5% excess), nickel(II) acetate, and manganese(II) acetate were dissolved in deionized water. Aqueous solutions of citric acid and poly(ethylene glycol) (PEG, number-average $M_W$ = 8 kDa) were added dropwise and stirred at ~110˚C. The molar ratio of transition metals to citric acid and PEG was 1:6 and 16:1 respectively. Concentrated nitric acid (70%) was then added dropwise until the solution appeared transparent and well dispersed. Following solvent evaporation after ~12 h, the resultant gel precursor was pre-calcined at 400 ˚C for 5 h under air to decompose the organic components. The ceramic powder was finely ground with a mortar and pestle and subsequently sintered at 900˚C for 12 h under air with a ramp rate of 2˚C/min using a box furnace (Atmosphere Furnace, Across International, Livingston, NJ, USA). The active material powder was then stored in an argon-filled glovebox ($O_2$ and $H_2O$ < 0.5 ppm; MBRAUN, Stratham, NH, USA).

### 6.2.2. Physical Characterization

The phase purity of the active material was assessed using powder X-ray diffraction (XRDMiniflex 600, Rigaku, Japan) with Cu $K_\alpha$ radiation ($\lambda$ = 1.5406 nm). The morphology of the particles was observed using scanning electron microscopy (SEM, LEO Zeiss 1550, Switzerland) using a 20 kV acceleration voltage and a working distance between 8 – 9 mm. Rietveld refinement was conducted on MAUD software.[81]

### 6.2.3. Molecular Layer Deposition Fabrication of Coin Cells

The electrode was prepared by grinding a slurry of 70 wt% active material, 20% conductive carbon black (Ketjenblack, Lion Specialty Chemical Co., Japan), and 10% PTFE-acetylene black binder in ethanol using a mortar and pestle. The electrode film was pressed (~10,000 kPa) onto a 15 mm diameter stainless steel mesh (400 mesh, grade 316) and dried overnight at 80˚C in a vacuum oven. The active material loading was 8 mg $cm^{-2}$. The coating of ultrathin alucone on the electrodes was performed using an ALD reactor (Thermal Gemstar 6XT, Arradiance LLC, Sudbury, MA, USA) at 100 °C in which trimethylaluminum (TMA) and ethylene glycol (EG) were used as precursors in accordance with prior work.[158] Titanicone deposition was performed at 120 ˚C using titanium tetrachloride (TiCl4) and EG as precursors. $TiCl_4$ and EG were preheated at 60 ˚C and 90 ˚C respectively to increase the vapor pressure. The purging time for the precursors was 21 ms. Thickness was controlled based on the number of deposition cycles – alucone-coated electrodes with five or ten-cycle thickness are denoted Alu-5C or Alu-10C respectively while titanicone samples are denoted Tit-5C or Tit-10C.

### 6.2.4. Electrochemical Characterization

The electrochemical performance of the electrodes was assessed by assembling CR2032 coin cells in an argon-filled glove box using a pure sodium foil (Sigma-Aldrich) as the counter electrode, a polypropylene separator (Celgard 2400, Charlotte, NC, USA), and an electrolyte comprised of 1 M $NaClO_4$ dissolved in 1:1:0.1 ethylene carbonate:diethyl carbonate:fluoroethylene carbonate (Sigma-Aldrich) by volume. Charge-discharge and galvanostatic intermittent titration technique (GITT) studies were carried out at ambient temperature using a CT2001A LANDt battery testing system (Wuhan, China). The C-rate is defined based on 140 mA $g^{-1}$ = 1 C. GITT was conducted using 6 min of charge or discharge at 0.05 C followed by 1 h of rest. Electrochemical impedance spectroscopy (EIS) measurements (Gamry Instruments, Warminster, PA, USA) were conducted from 1 MHz to 100 mHz at a discharged state (~2 V).

## 6.3. Results and Discussion

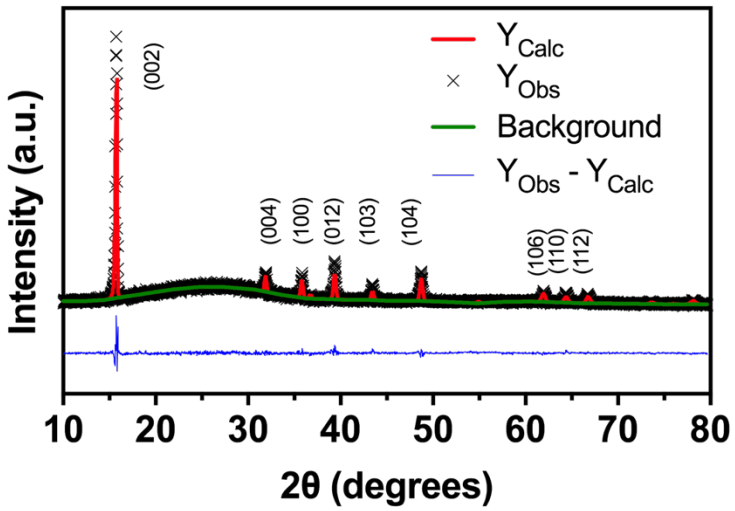


**Figure 38.** XRD pattern and Rietveld Refinement ($R_{wp}$ = 4.2%) of synthesized P2-$Na_{2/3}Ni_{0.23}Mn_{2/3}Cu_{0.1}O_2$.

The powder XRD spectra (Figure 38) shows that $Na_{2/3}Ni_{0.23}Mn_{2/3}Cu_{0.}1O_2$ crystallized as a phase-pure P2-layered material with a hexagonal lattice indexed to the $P6_3/mmc$ space group. The

hexagonal lattice parameters were obtained *via* Rietveld refinement, yielding $a$ = 2.895 and $c$ = 11.212.

In order to study the electrode degradation mechanisms and the effect of the ultrathin metalcone coating, the cycle stability was assessed at two voltage ranges: 2 – 4.5 V and 1.5 – 4.1 V *vs* $Na/Na^+$. As discussed earlier, the 2 – 4.5 V range involves the harmful P2-O2 phase transition and electrolyte instability, which cannot be kinetically avoided at low-current testing, while the 1.5 – 4.1 V range avoids these issues but introduces the $Mn^{3+}/Mn^{4+}$ redox activity. In comparison, the cycle stability of the pristine electrode tested at 2 – 4.1 V and 20 mA $g^{-1}$ is shown in Figure 39, which displays excellent stability by avoiding the aforementioned issues albeit with low discharge capacity. Thus, coatings are unlikely to improve the performance at this voltage range.

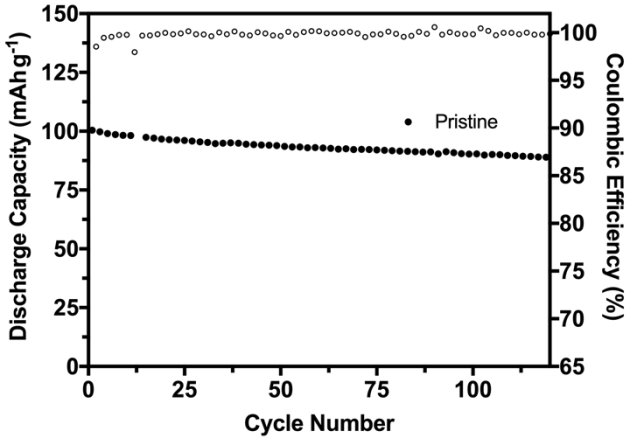


**Figure 39.** Stability of pristine electrode cycled from 2 – 4.1 V at 20 mA $g^{-1}$.

Figure 40 displays the initial redox behavior of the pristine and coated electrodes at 20 mA $g^{-1}$. As seen in the charge-discharge plateaus (Figure 40A and 40B) and corresponding dQ/dV plots (Figure 40C and 40D), the $Ni^{2+}/Ni^{3+}$ and $Ni^{3+}/Ni^{4+}$ redox peak potentials are observed from 3.3 – 3.7 V while $Cu^{2+}/Cu^{3+}$ occurs from 3.8 – 4 V.[156] The minor peaks from 2 – 3 V are associated with

$Na^+$/vacancy ordering. When cycling from 2 – 4.5 V, of particular note is the redox pair at 4.23/3.78 V, which is associated with the P2-O2 phase transition. This redox pair was not observed in the second cycle (Figure 40C), indicating poor reversibility of the phase transition. Compared to the parent P2-$Na_{2/3}Ni_{1/3}Mn_{2/3}O_2$ compound, the charge curve plateau associated with the P2-O2 transition is substantially less pronounced, indicating suppression of $Na^+$/vacancy ordering and gliding of the transition metal oxide layers.[87] From 1.5 – 4.1 V (Figure 40B and 40C) the large plateaus and peak potentials below 2 V indicate the substantial capacity contribution from the $Mn^{3+}/Mn^{4+}$ redox. As the P2-O2 phase transition is not involved, the redox behavior between the first two cycles appears highly reversible. A comparison of the initial dQ/dV plot of the coated electrodes is shown in Figure 40E and 40F. In general, the ultrathin metalcone coatings did not increase the voltage polarization, suggesting good ionic and electronic conductivity. Furthermore, the alucone coating clearly lowered the voltage polarization in the discharge (reduction) curve. This effect is likely associated with alucone's ability to serve as an artificial cathode-electrolyte interface (CEI) and mitigate side-reactions with the electrolyte, as electrolyte oxidation will occur during the initial charge cycle, especially at low current. On the other hand, the higher polarization of the titanicone sample suggests that it may not be as effective in suppressing electrolyte side reactions. Comparisons between $Al_2O_3$ ($E_g$ = 9.00 eV) and $TiO_2$ ($E_g$ = 3.18 eV) coatings in prior work have shown that $TiO_2$ is more reactive with the electrolyte due to its lower band gap, [157] and thus a similar effect may apply for the metalcone analogues. The relatively low peak intensities of the P2-O2 transition in the Tit-5C, Tit-10C, and Alu-10C coated samples may indicate some ability to suppress this transition.

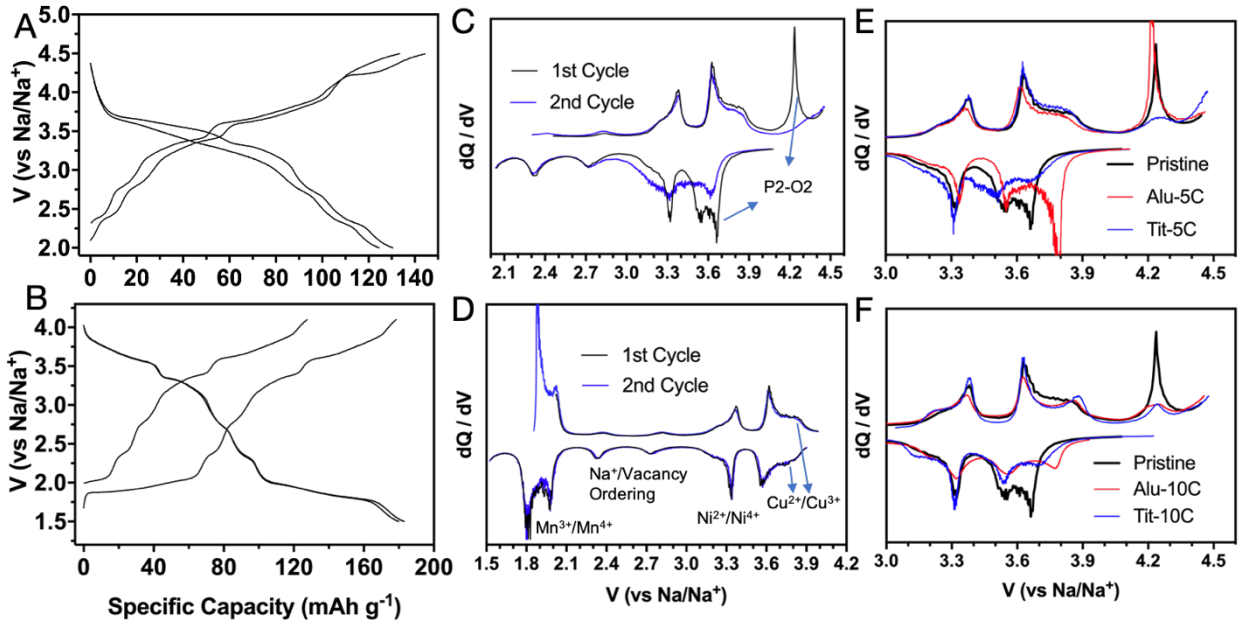


**Figure 40.** First two charge-discharge curves of pristine electrode cycled from 2 – 4.5 V (A) and 1.5 – 4.1 V (B) with corresponding dQ/dV curves at (C) and (D) respectively. Comparison of initial charge-discharge dQ/dV plots among pristine and metalcone coatings at five cycle (E) and 10 cycle (F) thickness.

The $Na^+$ diffusion coefficients ($D_{Na+}$) calculated by GITT throughout the first charge-discharge cycle are shown in Figure 41. During the first charge (Figure 41A), the $D_{Na+}$ rapidly drops as the voltage exceeds 4.2 V due to the kinetic unfavorability of the P2-O2 phase transition. There is a high energy barrier for $Na^+$ diffusion through the octahedral sites that form at high voltages due to strong Coulombic repulsion between $Na^+$ and the metal oxide layers.[92] During discharge, the peak minima of $D_{Na+}$ are associated with the transformation back to the P2 phase at ~3.6 V, $Na^+$/vacancy ordering (2-3 V), and the P2-P2' phase transition below 2 V attributed to orthorhombic distortion from the formation of Jahn-Teller distorted $Mn^{3+}$. These events correspond with the dQ/dV curves in Figure 40. As shown in Figure 41B, the coatings generally increased tge $D_{Na+}$ throughout discharge, likely due to the suppression of electrolyte decomposition.

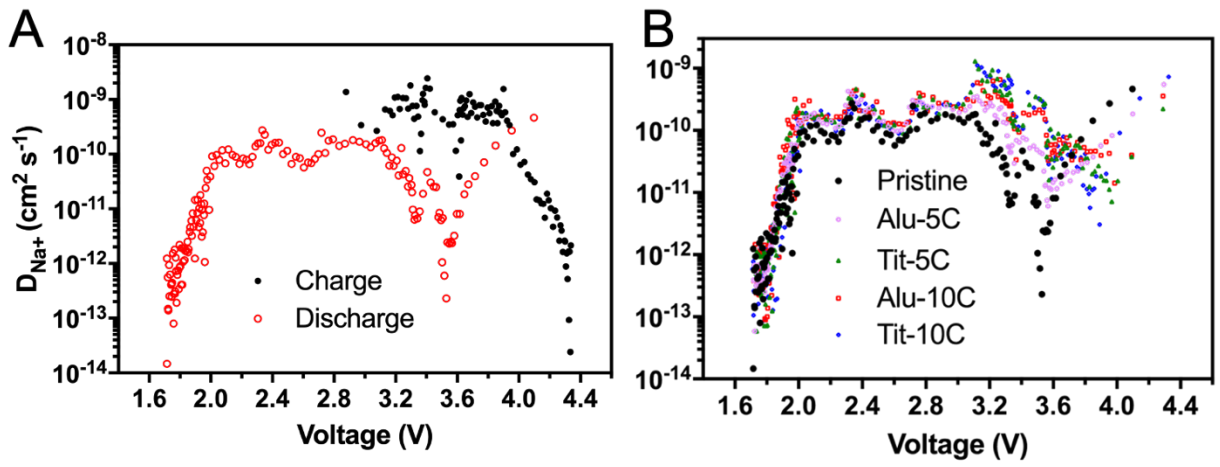


**Figure 41.** $D_{Na+}$ determined by GITT as a function of voltage. A) First charge and discharge cycle of pristine sample. B) Comparison among pristine and coated samples of the first discharge ($Na^+$ insertion) cycle.

It should be emphasized that there are potentially competing effects of the coating. The coating can serve as an artificial CEI layer and can mitigate electrode-electrolyte side reactions and active material dissolution. However, it can also restrict $Na^+$ diffusion at the interface, thus requiring optimization. When cycling from 2 – 4.5 V at 20 mA $g^{-1}$ (0.14 C), the initial discharge capacity (IDC) of the Alu-5C sample was similar to the pristine sample (Table 6), while Alu-10C displayed a lower IDC, which is likely due to its thicker $Na^+$ diffusion barrier. However, the loss of discharge capacity between the first two cycles was low for Alu-10C (Table 6), suggesting that the coating was effective at serving as an artificial CEI and suppressing electrode-electrolyte side reactions. On the other hand, the IDC and capacity drop of both Tit-5C and Tit-10C was high, likely due to its increased electrolyte reactivity as discussed earlier. However, Figure 42 clearly shows that all coatings tested did not noticeably improve the cycle stability. While the dQ/dV plots (Figure 40E and 40F) and GITT data suggest that the coatings could potentially suppress the P2-O2 phase changes, their effectiveness is ultimately limited, as the coatings were applied on the electrode surface rather than the active material powder. Furthermore, the deposited coatings are amorphous

and were not sintered at high temperatures (~600 ˚C) to potentially cation-dope the surface of the active particles, thus limiting their influence on lattice changes. Although prior work has demonstrated that amorphous metal oxide coatings (typically $Al_2O_3$) could physically suppress *c*-axis lattice expansion upon desodiation and reduce particle exfoliation,[48,159] the metalcone coatings may not be as effective due to their soft and flexible nature. In contrast to other reports,[160,161] we observed no noticeable difference in coulombic efficiency between the pristine and coated samples (Table 6). This may be an effect of the fluoroethylene carbonate electrolyte additive used in this work, which can help form a stable CEI layer and significantly improve the coulombic efficiency.[162] The lack of stability improvements from the coatings may also be associated with the use of $NaClO_4$ instead of $NaPF_6$, which mitigates the issue of cathode metal corrosion from trace HF generated ($NaPF_6 + H_2O_{(trace)} \rightarrow NaF + 2HF + OPF_3$). HF corrosion is a persistent and well known issue in $LiPF_6$-based LIBs, and coatings (typically $Al_2O_3$) can act as a Lewis base to quench residual HF.[50] Under these conditions, the stabilization of the electrode-electrolyte patristic reactions from the coatings was not impactful, as the irreversible bulk P2-O2 phase change predominates the degradation mechanism at this voltage range and current. Similarly, Wang *et al.* studied the degradation behavior of the parent P2-$Na_{2/3}Ni_{1/3}Mn_{2/3}O_2$ compound using the same electrolyte composition and found near-identical cycle stability at an upper cut-off voltage of 4.25 V and 4.5 V at 17.3 mA $g^{-1}$, suggesting that electrolyte side-reaction and surface degradation factors were insignificant relative to the P2-O2 phase transition.[163] They found that the P2-O2 transition induced intragranular crack propagation along the (002) lattice plane, which was the main contributor to capacity decay. While we would expect the applied coating to help maintain the particle integrity and protect cracked surfaces from exposure to the electrolyte, resulting in an

improved cycle retention, this factor may not be as prevalent in our material as the Cu doping generates a solid-solution type behavior with suppressed volume changes at high voltages.[156,164]

To study the degradation mechanism in further detail, EIS measurements were collected throughout cycling (Figure 42D and 42E) at 2 – 45 V and 20 mA $g^{-1}$. The spectra display an asymmetric semicircle denoted the charge-transfer resistance ($R_{ct}$) which reflects the combined effect of $Na^+$ diffusion resistance across the coating and/or CEI layer and structural degradation on the active material surface. The inclined line represents the finite-length Warburg impedance (W) that corresponds to the solid-state diffusion of $Na^+$. As seen in Figure 42D, after 10 cycles, the alucone-coated samples displayed a lower $R_{ct}$ in a thickness-dependent manner, which supports the data from Table 6 and Figure 40E and 40F on its conductive property and ability to suppress electrode-electrolyte side reactions. On the other hand, the $R_{ct}$ of the titanicone-coated samples was relatively large, likely due to the increased electrolyte decomposition as suggested in Table 6. However, after 100 cycles, the $R_{ct}$ in all samples increased substantially by a similar magnitude, which is attributed to structural degradation and explains why the coated samples did not noticeably improve the long-term capacity retention.

**Table 6.** Comparison of initial discharge capacity, average coulombic efficiency (cycle 2 – 100), and drop in initial discharge capacity (cycle 1 – 2) of pristine and coated electrodes cycled at 2 – 4.5 V and 20 mA $g^{-1}$.

| Sample | Pristine | Alu-5C | Alu-10C | Tit-5C | Tit-10C |
|---|---|---|---|---|---|
| Initial Discharge Capacity (mAh $g^{-1}$) | 130.4 | 134.3 | 116.0 | 129.1 | 129.4 |
| Average Coulombic Efficiency (%) | 96.92 | 96.85 | 96.57% | 97.14 | 97.03% |
| Discharge Capacity Loss between First Two Cycles (%) | 4.4 | 3.8 | 2.3 | 5.7 | 6.5 |

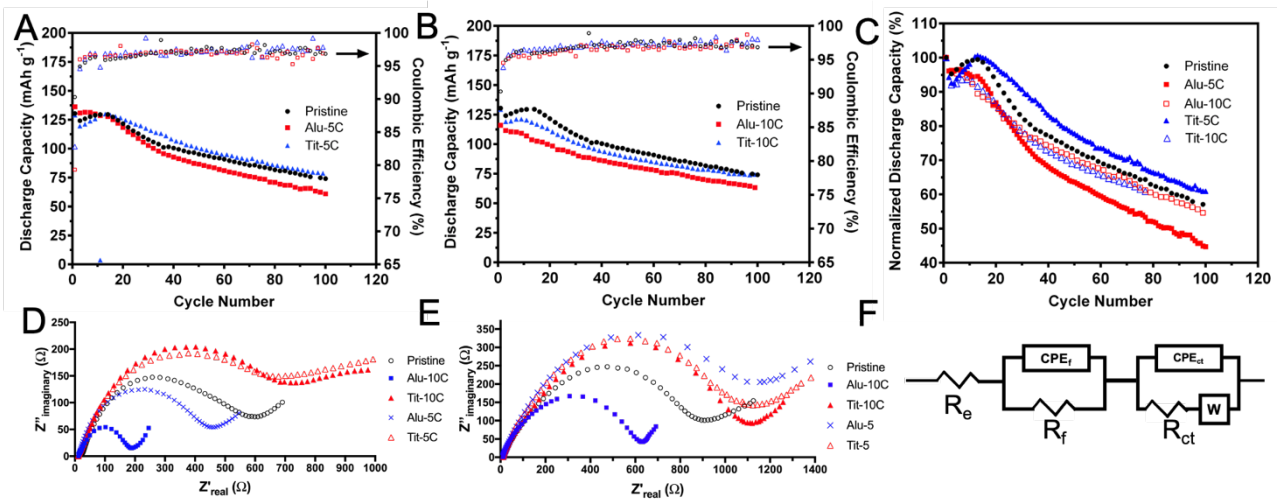


**Figure 42.** Cycle stability and EIS spectra of pristine and coated P2-$Na_{2/3}Ni_{0.23}Mn_{2/3}Cu_{0.1}O_2$ electrodes tested at 20 mA $g^{-1}$. A) Electrodes coated with 5 cycles tested from 2 – 4.5 V. B) Electrodes coated with 10 cycles tested from 2 – 4.5 V. C) Comparison based on normalized capacity retention. D) EIS spectra obtained after 10 cycles. E) EIS spectra collected after 100 cycles. F) Equivalent circuit model used to calculate the EIS parameters.

Figure 43 below shows the rate performance of the pristine and coated samples. The coatings improved the rate performance in a thickness-dependent manner, remarkably even at a high current of 4 C. In comparison, reports on 5-10 cycle ALD-deposited ultrathin $Al_2O_3$ and $TiO_2$ typically demonstrate reduced rate performance as they are electronically and ionically insulating.[99,157,160,165] This demonstrates the porous and conductive nature of the metalcone coatings. The improved rate performance can be attributed to the stable artificial CEI that has a lower barrier for $Na^+$ diffusion compared to the typical CEI generated from electrolyte decomposition, which corresponds with the GITT results, while the effectiveness of alucone over titanicone can be ascribed to its lower reactivity with the electrolyte. The rate performance improvement, especially for titanicone, can also be ascribed to the coating maintaining the overall integrity and interconnectivity of the active particles. High discharge currents will concentrate $Na^+$ at the surface of the active particles, which can lead to anisotropic volume changes, particle cracking, and surface exfoliation. To verify this effect, the cycle stability of the electrodes were assessed at 2 C (280 mA $g^{-1}$) after three initial

cycles at 0.1 C. At this elevated current, the adverse effects of the P2-O2 phase transition and electrolyte decomposition are kinetically suppressed, and the degradation mechanism is primarily ascribed to particle cracking. As seen in Figure 43C and 43D, the coatings significantly improved the stability, retaining 97%, 93%, and 82% capacity for the Alu-10C, Tit-10C, and pristine samples respectively after 200 cycles. After 500 cycles, the pristine sample decayed entirely, suggesting significant losses of interconnectivity among the active particles, carbonaceous matrix, and current collector, while Alu-10C and Tit-10C retained 81% and 70% capacity respectively. The improved stability of alucone over titanicone may be associated with its higher fracture toughness. Although the mechanical properties of our deposited metalcone coatings were not directly measured, the higher fracture toughness of $Al_2O_3 > TiO_2$ resulting in improved stability is well documented.[49]

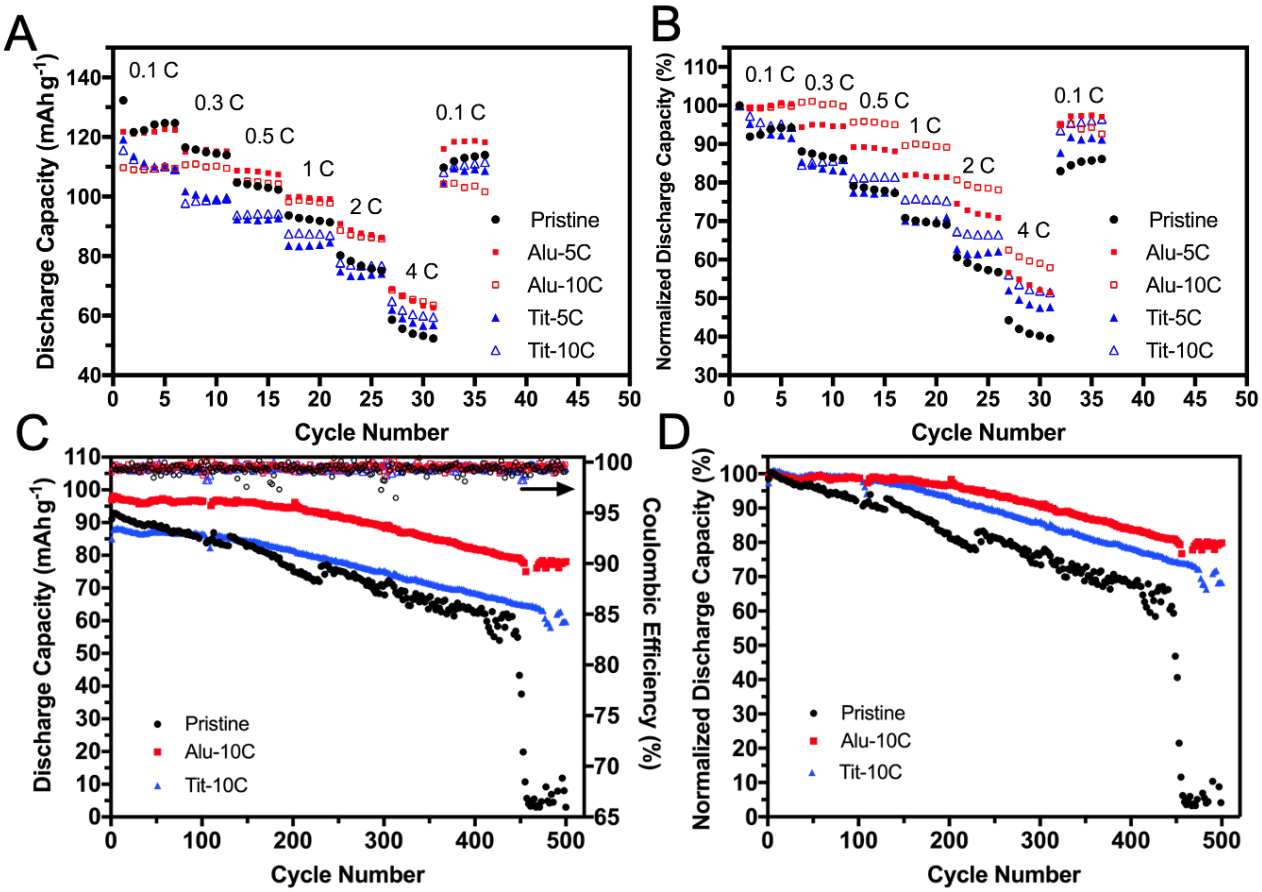


**Figure 43.** A and B) Rate performance of pristine and coated P2-$Na_{2/3}Ni_{0.23}Mn_{2/3}Cu_{0.1}O_2$ electrodes. C and D) Cycle stability of pristine and coated P2-$Na_{2/3}Ni_{0.23}Mn_{2/3}Cu_{0.1}O_2$ electrodes tested at 280 mA $g^{-1}$ (2 C) from 2 – 4.5 V.

The cycle performance of the pristine and coated electrodes was also tested from 1.5 – 4.1 V at 20 mA $g^{-1}$ (Figure 44A-C). The coatings improved the cycle retention in a thickness-dependent manner, in which the Alu-10C, Alu-5C, Tit-10C, Tit-5C, and pristine samples retained 73%, 70%, 64%, 61%, and 57% capacity respectively after 100 cycles. Although an increased coating thickness did not suppress the initial discharge capacity, the titanicone-coated samples displayed a lower capacity. Comparison of the dQ/dV curves (Figure 44D) reveals that the titanicone-coated samples displayed increased voltage polarization at the $Mn^{3+}/Mn^{4+}$ peak potential, suggesting that $Na^+$ insertion was impeded at this region. As seen in Figure 44E, capacity loss at this voltage range,

especially throughout the initial cycles, is largely associated the loss of the discharge plateau at < 2 V, which as mentioned represents the $Mn^{3+}/Mn^{4+}$ redox. Voltage polarization > 2 V is also evident, likely due to lattice distortion from $Mn^{3+}O_6$ octahedra, resulting in constrictions of $Na^+$ diffusion sites. Comparing the capacity change at voltage windows of 2 – 4.1 V and 1.5 – 2 V, the pristine sample retained 72% and 38% respectively after 100 cycles. This is indicative of Mn dissolution caused by the formation of $Mn^{3+}$ upon discharge and the ensuing disproportionation reaction: $2Mn^{3+}_{solid} \rightarrow Mn^{4+}_{solid} + Mn^{2+}_{solution}$. Mn dissolution also generates structural distortion, leading to significant polarization as seen in Figure 44E. Figure 44F compares the discharge curves after 50 cycles, which shows that the coatings can suppress Mn dissolution and help preserve the plateau at < 2 V. The Alu-10C sample retained 61% of its capacity from 1.5 – 2 V while the pristine sample retained only 50%. The issue with Mn dissolution is particularly concerning in full cell configuration, as solvated $Mn^{2+}$ can diffuse to the anode where it is reduced and plated, thus quenching the cell capacity.[161,166]

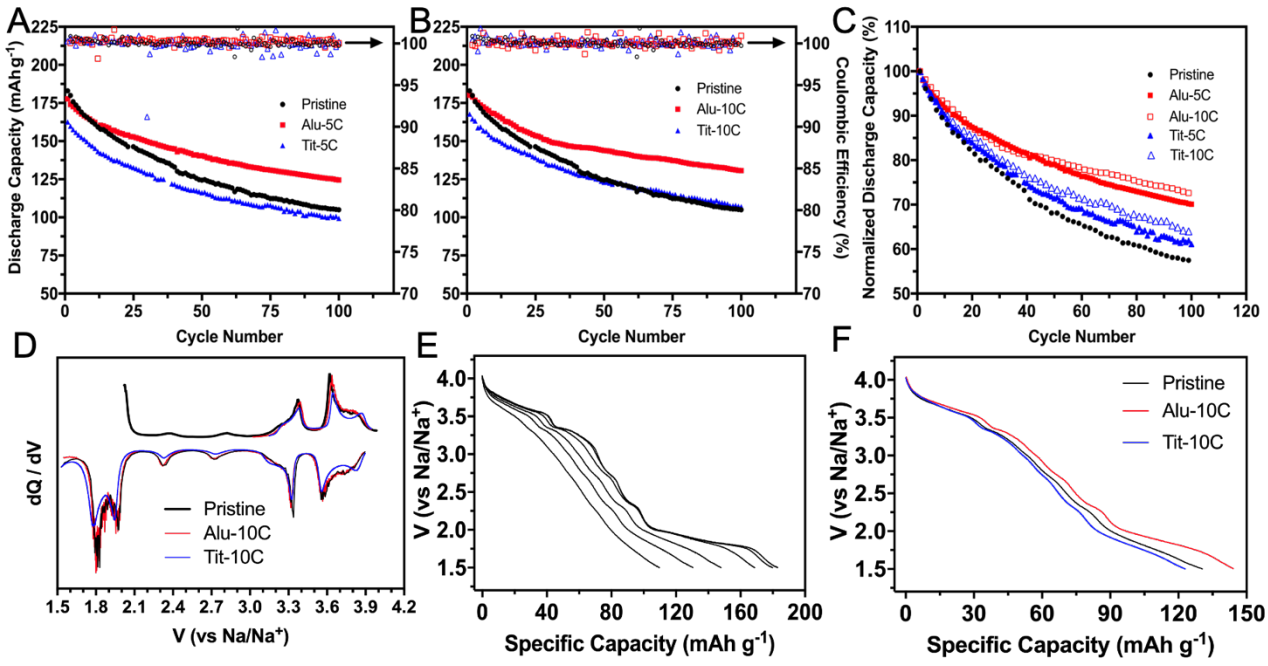

**Figure 44.** Cycle stability of pristine and coated P2-$Na_{2/3}Ni_{0.23}Mn_{2/3}Cu_{0.1}O_2$ electrodes tested at 20 mA $g^{-1}$ from 1.5 – 4.1 V. A) Electrodes coated with 5 cycles. B) Electrodes coated with 10 cycles. C) Comparison based on normalized capacity retention. D) dQ/dV plot of initial charge-discharge cycle. E) Pristine electrode discharge curves at cycle 1, 2, 10, 30, 50, and 100. F) Comparison of discharge curves at cycle 50.

# 7. Conclusions and Perspectives

Sodium-ion energy storage technologies demonstrate significant promise toward large-scale applications, such as stationary energy storage for intermittent renewable energy sources. Constraints over the supply of lithium in the next 50-100 years can bring the momentum and optimism of clean energy storage solutions to a halt. However, the performances demonstrated are currently not adequate for commercial applications, particularly due to the poor cycle performance associated with the repeated insertion and removal of large $Na^+$ ions from the host structures. In addition, electrodes should be comprised of cheap and abundant materials. For instance, cobalt is a scarce resource with a monopolistic supply chain structure, which has arisen significant concerns due to its use in LIB cathodes.[7] Clearly, reliance on cobalt for SIB electrodes is neither sustainable nor practical.

In **Section 4**, the cycle stability of P2-$Na_{2/3}Mn_yMg_{1-y}O_2$ was assessed at upper cut-off voltages of 4.5, 4.6, and 4.7 V *vs* $Na/Na^+$ for $y = 0, 0.05, 0.1$ at low current. Raising the upper cut-off voltage increased the initial discharge capacity due to the enhanced $Na^+$ extraction and utilization. A 4.7 V extraction approached the theoretical limit. However, the cycle stability decayed severely – EIS and *ex-situ* XRD characterization demonstrated that the decay was associated with excessive

electrolyte decomposition, irreversible phase changes, and solvent insertion into the interlayer space. Furthermore, the reliance on the $Mn^{3+}/Mn^{4+}$ results in significant Mn dissolution due to the instability of the $Mn^{3+}$ ion. Mg doping was effective at suppressing phase changes and enhancing cycle stability. However, as the stabilizing mechanism is based on ensuring that $Na^+$ is retained in the structure at high cut-off voltages, Mg doping lowered the initial discharge capacity considerably. These findings indicate that a cathode coating to suppress Mn dissolution, maintain the electrode integrity, and reduce parasitic side-reactions with the electrolyte can further enhance the cycle stability. This was demonstrated in subsequent work that I was tangentially involved with.[158] A key disadvantage of the material is the low average discharge voltage (~2.6 V *vs* $Na/Na^+$). Thus it is important to find a suitable anode material (operating at < 0.5 V *vs* $Na/Na^+$) such that the full cell has a reasonable output voltage.

**Section 5** introduces $Na_2CoPO_4F$ for hybrid sodium-ion capacitors. The concept and early work of a hybrid capacitor was first introduced by Conway's group over 40 years ago using a ruthenium-based cathode that reversibly intercalated $H^+$.[167] However, these devices operated using aqueous electrolyte, which has a limited voltage window of thermodynamic stability. Modern hybrid capacitors utilize organic electrolyte that can achieve significantly expanded voltage windows (up to 3.5 V) and energy densities, and thus research interest has picked up over the past decade.[53] Hybrid capacitors can occupy a unique sector of the energy storage market, displaying an intermediate cycle stability and energy density to LIBs and supercapacitors. However, their utility is ultimately limited until the cycle stability can reach supercapacitor-like benchmarks (>100,000 cycles). $Na_2CoPO_4F$ has previously been tested as a SIB cathode (2 – 5 V *vs* $Na/Na^+$), demonstrating poor cycle stability due to structural evolution, and low solid-state $Na^+$ diffusion

kinetics. However, it demonstrated a pseudocapacitive charge-storage mechanism when functioning as an anode (0 – 3 V *vs* $Na/Na^+$). When coupled with commercial activated carbon as the cathode, the sodium hybrid capacitor demonstrated excellent cycle stability and rate performance. This performance can only be ascribed to the pseudocapacitance mechanism, as the $Na_2CoPO_4F$ powder had a low surface area and displayed poor performance (cycle stability and kinetics) when intercalation was involved. However, the main limitation is the relatively low energy density. Future work can involve generating nanostructures and coupling $Na_2CoPO_4F$ with conductive carbon matrices to enhance the pseudocapacitive and capacitive charge-storage contributions. In addition, the reliance on cobalt is not ideal for practical applications. Alternative compositions such as $Na_2FePO_4F$ and $Na_2Fe_{0.5}Mn_{0.5}PO_4F$ should be tested.

**Section 6** continues the exploration of P2-type SIB cathodes cycled at high cut-off voltages from **Section 4**. Here, P2-$Na_{2/3}Ni_{0.23}Mn_{2/3}Cu_{0.1}O_2$ was tested due to its high average voltage and popularity in the literature. Alucone and titanicone coatings were applied on the electrodes by molecular layer deposition at two thicknesses (5 and 10 deposition cycles). When cycled from 2 – 4.5 V *vs* $Na/Na^+$ at low current, the coatings demonstrated evidence of suppressing electrolyte decomposition; however, they did not improve the cycle stability. At this range, degradation was predominated by the irreversible P2-O2 phase transition (onset ~4.22 V). Alucone was less electronically conductive and thus less electrolyte-reactive than titanicone. At elevated currents, electrolyte decomposition and the high-voltage P2-O2 phase transition was kinetically suppressed, and thus stability was predominated by particle cracking and fractured connectivity. Here, the coatings substantially improved the cycle retention by maintaining the overall integrity of the electrode. When cycled from 1.5 – 4.1 V *vs* $Na/Na^+$ at low current, the P2-O2 phase transition is

avoided while the $Mn^{3+}/Mn^{4+}$ becomes active. In this scenario, the coatings significantly improved cycle retention by suppressing Mn dissolution. In follow-up work, *in-situ* XRD will be conducted to assess the coatings' impact on potentially suppressing phase changes in closer detail. ICP-OES dissolution tests will verify that the coatings can suppress active material dissolution into the electrolyte. SEM and HR-TEM imaging of the cycled electrodes will be used to verify that the coatings can suppress particle cracking and disconnection. Finally, the mechanical properties and thickness of the metalcone films will be measured using atomic force microscopy.

# References


(1) International Energy Agency. *World Energy Outlook 2012*; 2012.
(2) AVICENNE Energy. *Current Status and Future Trends of the Global Li-Ion Battery Market*; 2018.
(3) Or, T.; Gourley, S. W. D.; Kaliyappan, K.; Yu, A.; Chen, Z. Recycling of Mixed Cathode Lithium-ion Batteries for Electric Vehicles: Current Status and Future Outlook. *Carbon Energy* **2020**, *2* (1), 6–43.
(4) U.S. Geological Survey. *Mineral Commodity Summaries*; 2019.
(5) Gruber, P. W.; Medina, P. A.; Keoleian, G. A.; Kesler, S. E.; Everson, M. P.; Wallington, T. J. Global Lithium Availability. *J. Ind. Ecol.* **2011**, *15* (5), 760–775.
(6) Narins, T. P. The Battery Business: Lithium Availability and the Growth of the Global Electric Car Industry. *Extr. Ind. Soc.* **2017**, *4* (2), 321–328.
(7) Olivetti, E. A.; Ceder, G.; Gaustad, G. G.; Fu, X. Lithium-Ion Battery Supply Chain Considerations: Analysis of Potential Bottlenecks in Critical Metals. *Joule* **2017**, *1* (2), 229–243.
(8) Zeng, X.; Li, J.; Liu, L. Solving Spent Lithium-Ion Battery Problems in China: Opportunities and Challenges. *Renew. Sustain. Energy Rev.* **2015**, *52*, 1759–1767.
(9) Vikström, H.; Davidsson, S.; Höök, M. Lithium Availability and Future Production Outlooks. *Appl. Energy* **2013**, *110*, 252–266.
(10) Speirs, J.; Contestabile, M.; Houari, Y.; Gross, R. The Future of Lithium Availability for Electric Vehicle Batteries. *Renew. Sustain. Energy Rev.* **2014**, *35*, 183–193.
(11) Manthiram, A.; Yu, X.; Wang, S. Lithium Battery Chemistries Enabled by Solid-State Electrolytes. *Nat. Rev. Mater.* **2017**, *2* (4), 16103.
(12) Hadjipaschalis, I.; Poullikkas, A.; Efthimiou, V. Overview of Current and Future Energy Storage Technologies for Electric Power Applications. *Renew. Sustain. Energy Rev.* **2009**, *13* (6–7), 1513–1522.
(13) Yokoyama, Y.; Fukutsuka, T.; Miyazaki, K.; Abe, T. Origin of the Electrochemical Stability of Aqueous Concentrated Electrolyte Solutions. *J. Electrochem. Soc.* **2018**, *165* (14), A3299–A3303.
(14) Takehara, Z. Dissolution and Precipitation Reactions of Lead Sulfate in Positive and Negative Electrodes in Lead Acid Battery. *J. Power Sources* **2000**, *85* (1), 29–37.
(15) Bjornbom, P. Modeling the Recharge Kinetics of the Positive Electrode Active Mass of a Lead-Acid Battery. *J. Electrochem. Soc.* **1987**, *134* (7), 1600–1603.
(16) Cano, Z. P.; Banham, D.; Ye, S.; Hintennach, A.; Lu, J.; Fowler, M.; Chen, Z. Batteries and Fuel Cells for Emerging Electric Vehicle Markets. *Nat. Energy* **2018**, *3* (4), 279–289.
(17) Whittingham, M. S. Electrical Energy Storage and Intercalation Chemistry. *Science (80-. ).* **1976**, *192* (4244), 1126–1127.
(18) Mauger, A.; Julien, C. M.; Goodenough, J. B.; Zaghib, K. Tribute to Michel Armand: From Rocking Chair – Li-Ion to Solid-State Lithium Batteries. *J. Electrochem. Soc.* **2020**, *167* (7), 070507.
(19) Blomgren, G. E. The Development and Future of Lithium Ion Batteries. *J. Electrochem. Soc.* **2017**, *164* (1), A5019–A5025.
(20) Mizushima, K.; Jones, P. C.; Wiseman, P. J.; Goodenough, J. B. LixCoO2(0<x≤1): A New Cathode Material for Batteries of High Energy Density. *Solid State Ionics* **1981**, *3–4* (C), 171–174.

(21) Yoshino, A. The Birth of the Lithium-Ion Battery. *Angew. Chem. Int. Ed. Engl.* **2012**, *51* (24), 5798–5800.
(22) IITK. Basic Crystal Concepts http://home.iitk.ac.in/~sangals/crystosim/crystaltut.html (accessed Mar 5, 2020).
(23) Nitta, N.; Wu, F.; Lee, J. T.; Yushin, G. Li-Ion Battery Materials: Present and Future. *Mater. Today* **2015**, *18* (5), 252–264.
(24) Yamada, A. Lattice Instability in Li(LixMn2−x)O4. *J. Solid State Chem.* **1996**, *122* (1), 160–165.
(25) Li, X.; Xu, Y.; Wang, C. Suppression of Jahn–Teller Distortion of Spinel LiMn2O4 Cathode. *J. Alloys Compd.* **2009**, *479* (1–2), 310–313.
(26) Capsoni, D.; Bini, M.; Chiodelli, G.; Massarotti, V.; Mustarelli, P.; Linati, L.; Mozzati, M. C.; Azzoni, C. B. Jahn–Teller Transition in Al3+ Doped LiMn2O4 Spinel. *Solid State Commun.* **2003**, *126* (4), 169–174.
(27) Kim, K. J.; Lee, J. H. Effects of Nickel Doping on Structural and Optical Properties of Spinel Lithium Manganate Thin Films. *Solid State Commun.* **2007**, *141* (2), 99–103.
(28) Li, X.; Xu, Y.; Wang, C. Suppression of Jahn–Teller Distortion of Spinel LiMn2O4 Cathode. *J. Alloys Compd.* **2009**, *479* (1–2), 310–313.
(29) Guan, D.; Jeevarajan, J. A.; Wang, Y. Enhanced Cycleability of LiMn2O4 Cathodes by Atomic Layer Deposition of Nanosized-Thin Al2O3 Coatings. *Nanoscale* **2011**, *3* (4), 1465.
(30) Ansean, D.; Gonzalez, M.; Viera, J. C.; Alvarez, J. C.; Blanco, C.; Garcia, V. M. Evaluation of LiFePO4 in Batteries for Electric Vehicle Applications. In *2013 International Conference on New Concepts in Smart Cities: Fostering Public and Private Alliances (SmartMILE)*; 2013; pp 1–8.
(31) Bi, Z.; Zhang, X.; He, W.; Min, D.; Zhang, W. Recent Advances in LiFePO4 Nanoparticles with Different Morphology for High-Performance Lithium-Ion Batteries. *RSC Adv.* **2013**, *3* (43), 19744.
(32) Zubi, G.; Dufo-López, R.; Carvalho, M.; Pasaoglu, G. The Lithium-Ion Battery: State of the Art and Future Perspectives. *Renew. Sustain. Energy Rev.* **2018**, *89*, 292–308.
(33) Cheng, X.-B.; Zhang, R.; Zhao, C.-Z.; Zhang, Q. Toward Safe Lithium Metal Anode in Rechargeable Batteries: A Review. *Chem. Rev.* **2017**, *117* (15), 10403–10473.
(34) Abraham, K. M. Intercalation Positive Electrodes for Rechargeable Sodium Cells. *Solid State Ionics* **1982**, *7* (3), 199–212.
(35) Nayak, P. K.; Yang, L.; Brehm, W.; Adelhelm, P. From Lithium-Ion to Sodium-Ion Batteries: Advantages, Challenges, and Surprises. *Angew. Chemie Int. Ed.* **2018**, *57* (1), 102–120.
(36) Xiang, X.; Zhang, K.; Chen, J. Recent Advances and Prospects of Cathode Materials for Sodium-Ion Batteries. *Advanced Materials*. 2015, pp 5343–5364.
(37) Wen, Y.; He, K.; Zhu, Y.; Han, F.; Xu, Y.; Matsuda, I.; Ishii, Y.; Cumings, J.; Wang, C. Expanded Graphite as Superior Anode for Sodium-Ion Batteries. *Nat. Commun.* **2014**, *5* (1), 1–10.
(38) Cao, Y.; Xiao, L.; Sushko, M. L.; Wang, W.; Schwenzer, B.; Xiao, J.; Nie, Z.; Saraf, L. V.; Yang, Z.; Liu, J. Sodium Ion Insertion in Hollow Carbon Nanowires for Battery Applications. *Nano Lett.* **2012**, *12* (7), 3783–3787.
(39) Xiao, B.; Rojo, T.; Li, X. Hard Carbon as Sodium-Ion Battery Anodes: Progress and Challenges. *ChemSusChem* **2019**, *12* (1), 133–144.

(40) Clément, R. J.; Billaud, J.; Robert Armstrong, A.; Singh, G.; Rojo, T.; Bruce, P. G.; Grey, C. P. Structurally Stable Mg-Doped P2-Na $_{2/3}$ Mn $_{1-y}$ Mg $_{y}$ O $_{2}$ Sodium-Ion Battery Cathodes with High Rate Performance: Insights from Electrochemical, NMR and Diffraction Studies. *Energy Environ. Sci.* **2016**, *9* (10), 3240–3251.
(41) Delmas, C.; Fouassier, C.; Hagenmuller, P. Structural Classification and Properties of the Layered Oxides. *Phys. B+C* **1980**, *99* (1–4), 81–85.
(42) Wang, Y.; Xiao, R.; Hu, Y.-S.; Avdeev, M.; Chen, L. P2-Na0.6[Cr0.6Ti0.4]O2 Cation-Disordered Electrode for High-Rate Symmetric Rechargeable Sodium-Ion Batteries. *Nat. Commun.* **2015**, *6* (1), 6954.
(43) Wang, P.-F.; You, Y.; Yin, Y.-X.; Guo, Y.-G. Layered Oxide Cathodes for Sodium-Ion Batteries: Phase Transition, Air Stability, and Performance. *Adv. Energy Mater.* **2018**, *8* (8), 1701912.
(44) You, Y.; Manthiram, A. Progress in High-Voltage Cathode Materials for Rechargeable Sodium-Ion Batteries. *Adv. Energy Mater.* **2018**, *8* (2), 1701785.
(45) Lu, Z.; Dahn, J. R. In Situ X-Ray Diffraction Study of P2-Na[Sub 2/3][Ni[Sub 1/3]Mn[Sub 2/3]]O[Sub 2]. *J. Electrochem. Soc.* **2001**, *148* (11), A1225.
(46) Yabuuchi, N.; Hara, R.; Kubota, K.; Paulsen, J.; Kumakura, S.; Komaba, S. A New Electrode Material for Rechargeable Sodium Batteries: P2-Type Na2/3[Mg0.28Mn0.72]O2 with Anomalously High Reversible Capacity. *J. Mater. Chem. A* **2014**, *2* (40), 16851–16855.
(47) Cho, J. Enhancement of Thermal Stability of LiCoO[Sub 2] by LiMn[Sub 2]O[Sub 4] Coating. *Electrochem. Solid-State Lett.* **1999**, *2* (6), 253.
(48) Cho, J.; Kim, Y. J.; Park, B. Novel LiCoO2 Cathode Material with Al2O3 Coating for a Li Ion Cell. *Chem. Mater.* **2000**, *12* (12), 3788–3791.
(49) Cho, J.; Kim, Y. J.; Kim, T. J.; Park, B. Zero-Strain Intercalation Cathode for Rechargeable Li-Ion Cell. *Angew. Chemie - Int. Ed.* **2001**, *40* (18), 3367–3369.
(50) Chen, Z.; Dahn, J. R. Methods to Obtain Excellent Capacity Retention in LiCoO2 Cycled to 4.5 V. *Electrochim. Acta* **2004**, *49* (7), 1079–1090.
(51) Zhao, Y.; Zheng, K.; Sun, X. Addressing Interfacial Issues in Liquid-Based and Solid-State Batteries by Atomic and Molecular Layer Deposition. *Joule* **2018**, *2* (12), 2583–2604.
(52) SIMON, P.; GOGOTSI, Y. Materials for Electrochemical Capacitors. In *Nanoscience and Technology*; Co-Published with Macmillan Publishers Ltd, UK, 2009; pp 320–329.
(53) Ding, J.; Hu, W.; Paek, E.; Mitlin, D. Review of Hybrid Ion Capacitors: From Aqueous to Lithium to Sodium. *Chem. Rev.* **2018**, *118* (14), 6457–6498.
(54) Dubal, D. P.; Ayyad, O.; Gómez-Romero, P. Hybrid Energy Storage: The Merging of Battery and Supercapacitor Chemistries. *Chem. Soc. Rev.* **2015**, *34* (11), 4889–4899.
(55) Deng, S.; Li, J.; Sun, S.; Wang, H.; Liu, J.; Yan, H. Synthesis and Electrochemical Properties of Li4Ti5O12 Spheres and Its Application for Hybrid Supercapacitors. *Electrochim. Acta* **2014**, *146*, 37–43.
(56) Bauer, D.; Roberts, A. J.; Matsumi, N.; Darr, J. A. Nano-Sized Mo- and Nb-Doped TiO 2 as Anode Materials for High Energy and High Power Hybrid Li-Ion Capacitors. *Nanotechnology* **2017**, *28* (19), 195403.
(57) Yao, F.; Pham, D. T.; Lee, Y. H. Carbon-Based Materials for Lithium-Ion Batteries, Electrochemical Capacitors, and Their Hybrid Devices. *ChemSusChem* **2015**, *8* (14), 2284–2311.

(58) Arun, N.; Jain, A.; Aravindan, V.; Jayaraman, S.; Chui Ling, W.; Srinivasan, M. P.; Madhavi, S. Nanostructured Spinel LiNi0.5Mn1.5O4 as New Insertion Anode for Advanced Li-Ion Capacitors with High Power Capability. *Nano Energy* **2015**, *12*, 69–75.
(59) Karthikeyan, K.; Aravindan, V.; Lee, S. B.; Jang, I. C.; Lim, H. H.; Park, G. J.; Yoshio, M.; Lee, Y. S. A Novel Asymmetric Hybrid Supercapacitor Based on Li2FeSiO 4 and Activated Carbon Electrodes. *J. Alloys Compd.* **2010**, *504* (1), 224–227.
(60) Cericola, D.; Novák, P.; Wokaun, A.; Kötz, R. Hybridization of Electrochemical Capacitors and Rechargeable Batteries: An Experimental Analysis of the Different Possible Approaches Utilizing Activated Carbon, Li4Ti5O12 and LiMn2O 4. *J. Power Sources* **2011**, *196* (23), 10305–10313.
(61) Ohzuku, T.; Makimura, Y. Layered Lithium Insertion Material of LiNi1/2Mn1/2O2 : A Possible Alternative to LiCoO2 for Advanced Lithium-Ion Batteries. *Chem. Lett.* **2001**, *30* (8), 744–745.
(62) Zhou, F.; Zhao, X.; Van Bommel, A.; Rowe, A. W.; Dahn, J. R. Coprecipitation Synthesis of NixMn1-x(OH)2 Mixed Hydroxides. *Chem. Mater.* **2010**, *22* (3), 1015–1021.
(63) Danks, A. E.; Hall, S. R.; Schnepp, Z. The Evolution of 'Sol–Gel' Chemistry as a Technique for Materials Synthesis. *Mater. Horizons* **2016**, *3* (2), 91–112.
(64) Kaliyappan, K.; Xiao, W.; Adair, K. R.; Sham, T.-K.; Sun, X. Designing High-Performance Nanostructured P2-Type Cathode Based on a Template-Free Modified Pechini Method for Sodium-Ion Batteries. *ACS Omega* **2018**, *3* (7), 8309–8316.
(65) Etacheri, V.; Haik, O.; Goffer, Y.; Roberts, G. A.; Stefan, I. C.; Fasching, R.; Aurbach, D. Effect of Fluoroethylene Carbonate (FEC) on the Performance and Surface Chemistry of Si-Nanowire Li-Ion Battery Anodes. *Langmuir* **2012**, *28* (1), 965–976.
(66) Anton Paar. X-Ray diffraction (XRD) https://wiki.anton-paar.com/en/x-ray-diffraction-xrd/ (accessed Mar 4, 2020).
(67) Zhou, W.; Apkarian, R.; Wang, Z. L.; Joy, D. Fundamentals of Scanning Electron Microscopy (SEM). In *Scanning Microscopy for Nanotechnology*; Springer New York: New York, NY, 2006; pp 1–40.
(68) Henry, D. Electron-Sample Interactions https://serc.carleton.edu/research_education/geochemsheets/electroninteractions.html (accessed Mar 4, 2020).
(69) Zou, H.; Li, S.; Wu, X.; McDonald, M. J.; Yang, Y. Spray-Drying Synthesis of Pure Na2CoPO4F as Cathode Material for Sodium Ion Batteries. *ECS Electrochem. Lett.* **2015**, *4* (6), A53–A55.
(70) Zhang, S. S.; Xu, K.; Jow, T. R. Electrochemical Impedance Study on the Low Temperature of Li-Ion Batteries. *Electrochim. Acta* **2004**, *49* (7), 1057–1061.
(71) Dees, D. W.; Kawauchi, S.; Abraham, D. P.; Prakash, J. Analysis of the Galvanostatic Intermittent Titration Technique (GITT) as Applied to a Lithium-Ion Porous Electrode. *J. Power Sources* **2009**, *189* (1), 263–268.
(72) Metrohm Autolab. *Galvanostatic Intermittent Titration Technique*; 2014.
(73) Hwang, J.-Y.; Myung, S.-T.; Sun, Y.-K. Sodium-Ion Batteries: Present and Future. *Chem. Soc. Rev.* **2017**, *46* (12), 3529–3614.
(74) Caballero, A.; Hernán, L.; Morales, J.; Sánchez, L.; Santos Peña, J.; Aranda, M. A. G. Synthesis and Characterization of High-Temperature Hexagonal P2-Na0.6 Mno2 and Its Electrochemical Behaviour as Cathode in Sodium Cells. *J. Mater. Chem.* **2002**, *12* (4), 1142–1147.

(75) Su, D.; Wang, C.; Ahn, H. J.; Wang, G. Single Crystalline Na0.7MnO2 Nanoplates as Cathode Materials for Sodium-Ion Batteries with Enhanced Performance. *Chem. - A Eur. J.* **2013**, *19* (33), 10884–10889.
(76) Billaud, J.; Singh, G.; Armstrong, A. R.; Gonzalo, E.; Roddatis, V.; Armand, M.; Ofilo Rojo, T.; Bruce, P. G. Na2/3Mn1-XMgxO2 ($0 \leq x \leq 0.2$): A High Capacity Cathode for Sodium-Ion Batteries. *Energy Environ. Sci* **2014**, *7*.
(77) Buchholz, D.; Vaalma, C.; Chagas, L. G.; Passerini, S. Mg-Doping for Improved Long-Term Cyclability of Layered Na-Ion Cathode Materials - The Example of P2-Type NaxMg0.11Mn0.89O2. *J. Power Sources* **2015**, *282*, 581–585.
(78) Sharma, N.; Tapia-Ruiz, N.; Singh, G.; Armstrong, A. R.; Pramudita, J. C.; Brand, H. E. A.; Billaud, J.; Bruce, P. G.; Rojo, T. Rate Dependent Performance Related to Crystal Structure Evolution of Na2/3Mn0.8Mg0.2O2 in a Sodium-Ion Battery. *Chem. Mater.* **2015**, *27* (20), 6976–6986.
(79) Yabuuchi, N.; Hara, R.; Kubota, K.; Paulsen, J.; Kumakura, S.; Komaba, S. A New Electrode Material for Rechargeable Sodium Batteries: P2-Type Na 2/3 [Mg 0.28 Mn 0.72 ]O 2 with Anomalously High Reversible Capacity. *J. Mater. Chem. A* **2014**, *2* (40), 16851–16855.
(80) Clément, R. J.; Billaud, J.; Robert Armstrong, A.; Singh, G.; Rojo, T.; Bruce, P. G.; Grey, C. P. Structurally Stable Mg-Doped P2-Na2/3Mn1-YMgyO2sodium-Ion Battery Cathodes with High Rate Performance: Insights from Electrochemical, NMR and Diffraction Studies. *Energy Environ. Sci.* **2016**, *9* (10), 3240–3251.
(81) Lutterotti, L. Total Pattern Fitting for the Combined Size–Strain–Stress–Texture Determination in Thin Film Diffraction. *Nucl. Instruments Methods Phys. Res. Sect. B Beam Interact. with Mater. Atoms* **2010**, *268* (3–4), 334–340.
(82) Lu, Z.; Dahn, J. R. The Effect of Co Substitution for Ni on the Structure and Electrochemical Behavior of T2 and O2 Structure Li[Sub 2/3][Co[Sub x]Ni[Sub 1/3−x]Mn[Sub 2/3]]O[Sub 2]. *J. Electrochem. Soc.* **2001**, *148* (3), A237.
(83) Xia, H.; Wang, H.; Xiao, W.; Lu, L.; Lai, M. O. Properties of LiNi1/3Co1/3Mn1/3O2 Cathode Material Synthesized by a Modified Pechini Method for High-Power Lithium-Ion Batteries. *J. Alloys Compd.* **2009**, *480* (2), 696–701.
(84) Zaki, T.; Kabel, K. I.; Hassan, H. Using Modified Pechini Method to Synthesize α-Al2O3 Nanoparticles of High Surface Area. *Ceram. Int.* **2012**, *38* (6), 4861–4866.
(85) Croce, F.; D' Epifanio, A.; Hassoun, J.; Deptula, A.; Olczac, T.; Scrosati, B. A Novel Concept for the Synthesis of an Improved LiFePO[Sub 4] Lithium Battery Cathode. *Electrochem. Solid-State Lett.* **2002**, *5* (3), A47.
(86) Shannon, R. D.; Prewitt, C. T. Effective Ionic Radii in Oxides and Fluorides. *Acta Crystallogr. Sect. B Struct. Crystallogr. Cryst. Chem.* **1969**, *25* (5), 925–946.
(87) Wang, P.-F.; You, Y.; Yin, Y.-X.; Wang, Y.-S.; Wan, L.-J.; Gu, L.; Guo, Y.-G. Suppressing the P2-O2 Phase Transition of $Na_{2/3}Mn_{2/3}Ni_{0.33}O_2$ by Magnesium Substitution for Improved Sodium-Ion Batteries. *Angew. Chemie Int. Ed.* **2016**, *55* (26), 7445–7449.
(88) Singh, G.; Tapia-Ruiz, N.; Lopez del Amo, J. M.; Maitra, U.; Somerville, J. W.; Armstrong, A. R.; Martinez de Ilarduya, J.; Rojo, T.; Bruce, P. G. High Voltage Mg-Doped $Na_{2/3}Ni_{0.3-x}Mg_xMn_{0.7}O_2$ ($x = 0.05, 0.1$) Na-Ion Cathodes with Enhanced Stability and Rate Capability. *Chem. Mater.* **2016**, *28* (14), 5087–5094.
(89) Wu, X.; Guo, J.; Wang, D.; Zhong, G.; McDonald, M. J.; Yang, Y. P2-Type

Na2/3Ni0.33–XZnxMn2/3O2 as New High-Voltage Cathode Materials for Sodium-Ion Batteries. *J. Power Sources* **2015**, *281*, 18–26.
(90) Chayambuka, K.; Mulder, G.; Danilov, D. L.; Notten, P. H. L. Sodium-Ion Battery Materials and Electrochemical Properties Reviewed. *Adv. Energy Mater.* **2018**, *8* (16), 1800079.
(91) Chagas, L. G.; Buchholz, D.; Wu, L.; Vortmann, B.; Passerini, S. Unexpected Performance of Layered Sodium-Ion Cathode Material in Ionic Liquid-Based Electrolyte. *J. Power Sources* **2014**, *247*, 377–383.
(92) Saadoune, I.; Maazaz, A.; Ménétrier, M.; Delmas, C. On the NaxNi0.6Co0.4O2System: Physical and Electrochemical Studies. *J. Solid State Chem.* **1996**, *122* (1), 111–117.
(93) Li, Z.-Y.; Gao, R.; Zhang, J.; Zhang, X.; Hu, Z.; Liu, X. New Insights into Designing High-Rate Performance Cathode Materials for Sodium Ion Batteries by Enlarging the Slab-Spacing of the Na-Ion Diffusion Layer. *J. Mater. Chem. A* **2016**, *4* (9), 3453–3461.
(94) Mendiboure, A.; Delmas, C.; Hagenmuller, P. Electrochemical Intercalation and Deintercalation of NaxMnO2 Bronzes. *J. Solid State Chem.* **1985**, *57* (3), 323–331.
(95) Hou, P.; Sun, Y.; Li, F.; Sun, Y.; Deng, X.; Zhang, H.; Xu, X.; Zhang, L. A High Energy-Density P2-Na $_{2/3}$ [Ni $_{0.3}$ Co $_{0.1}$ Mn $_{0.6}$ ]O $_{2}$ Cathode with Mitigated P2–O2 Transition for Sodium-Ion Batteries. *Nanoscale* **2019**, *11* (6), 2787–2794.
(96) Hou, H.; Gan, B.; Gong, Y.; Chen, N.; Sun, C. P2-Type Na $_{2/3}$ Ni $_{0.23}$ Mg $_{0.1}$ Mn $_{2/3}$ O $_{2}$ as a High-Performance Cathode for a Sodium-Ion Battery. *Inorg. Chem.* **2016**, *55* (17), 9033–9037.
(97) Wang, H.; Yang, B.; Liao, X.-Z.; Xu, J.; Yang, D.; He, Y.-S.; Ma, Z.-F. Electrochemical Properties of P2-Na2/3[Ni1/3Mn2/3]O2 Cathode Material for Sodium Ion Batteries When Cycled in Different Voltage Ranges. *Electrochim. Acta* **2013**, *113*, 200–204.
(98) Yuan, D. D.; Wang, Y. X.; Cao, Y. L.; Ai, X. P.; Yang, H. X. Improved Electrochemical Performance of Fe-Substituted NaNi $_{0.5}$ Mn $_{0.5}$ O $_{2}$ Cathode Materials for Sodium-Ion Batteries. *ACS Appl. Mater. Interfaces* **2015**, *7* (16), 8585–8591.
(99) Kaliyappan, K.; Liu, J.; Lushington, A.; Li, R.; Sun, X. Highly Stable Na $_{2/3}$ (Mn $_{0.54}$ Ni $_{0.13}$ Co $_{0.13}$ )O $_{2}$ Cathode Modified by Atomic Layer Deposition for Sodium-Ion Batteries. *ChemSusChem* **2015**, *8* (15), 2537–2543.
(100) Ramasamy, H. V.; Kaliyappan, K.; Thangavel, R.; Aravindan, V.; Kang, K.; Kim, D. U.; Park, Y.; Sun, X.; Lee, Y.-S. Cu-Doped P2-Na $_{0.5}$ Ni $_{0.33}$ Mn $_{2/3}$ O $_{2}$ Encapsulated with MgO as a Novel High Voltage Cathode with Enhanced Na-Storage Properties. *J. Mater. Chem. A* **2017**, *5* (18), 8408–8415.
(101) Pang, W.-L.; Guo, J.-Z.; Zhang, X.-H.; Fan, C.-Y.; Nie, X.-J.; Yu, H.-Y.; Li, W.-H.; Yang, Q.; Wu, X.-L. P2-Type Na2/3Mn1/2Co1/3Cu1/6O2 as Advanced Cathode Material for Sodium-Ion Batteries: Electrochemical Properties and Electrode Kinetics. *J. Alloys Compd.* **2019**, *790*, 1092–1100.
(102) Yang, Q.; Wang, P.-F.; Guo, J.-Z.; Chen, Z.-M.; Pang, W.-L.; Huang, K.-C.; Guo, Y.-G.; Wu, X.-L.; Zhang, J.-P. Advanced P2-Na $_{2/3}$ Ni $_{1/3}$ Mn $_{7/12}$ Fe $_{1/12}$ O $_{2}$ Cathode Material with Suppressed P2–O2 Phase Transition toward High-Performance Sodium-Ion Battery. *ACS Appl. Mater. Interfaces* **2018**, *10* (40), 34272–34282.
(103) Yabuuchi, N.; Kajiyama, M.; Iwatate, J.; Nishikawa, H.; Hitomi, S.; Okuyama, R.; Usui, R.; Yamada, Y.; Komaba, S. P2-Type Nax[Fe1/2Mn1/2]O2 Made from Earth-Abundant Elements for Rechargeable Na Batteries. *Nat. Mater.* **2012**, *11* (6), 512–517.
(104) Mortemard de Boisse, B.; Carlier, D.; Guignard, M.; Bourgeois, L.; Delmas, C. P2-Na $_{x}$

Mn 1/2 Fe 1/2 O 2 Phase Used as Positive Electrode in Na Batteries: Structural Changes Induced by the Electrochemical (De)Intercalation Process. *Inorg. Chem.* **2014**, *53* (20), 11197–11205.
(105) Talaie, E.; Duffort, V.; Smith, H. L.; Fultz, B.; Nazar, L. F. Structure of the High Voltage Phase of Layered P2-Na 2/3−z [Mn 1/2 Fe 1/2 ]O 2 and the Positive Effect of Ni Substitution on Its Stability. *Energy Environ. Sci.* **2015**, *8* (8), 2512–2523.
(106) Buchholz, D.; Chagas, L. G.; Vaalma, C.; Wu, L.; Passerini, S. Water Sensitivity of Layered P2/P3-Na x Ni 0.22 Co 0.11 Mn 2/3 O 2 Cathode Material. *J. Mater. Chem. A* **2014**, *2* (33), 13415–13421.
(107) Dsoke, S.; Fuchs, B.; Gucciardi, E.; Wohlfahrt-Mehrens, M. The Importance of the Electrode Mass Ratio in a Li-Ion Capacitor Based on Activated Carbon and Li4Ti5O12. *J. Power Sources* **2015**, *282*, 385–393.
(108) Ding, J.; Wang, H.; Li, Z.; Cui, K.; Karpuzov, D.; Tan, X.; Kohandehghan, A.; Mitlin, D. Peanut Shell Hybrid Sodium Ion Capacitor with Extreme Energy-Power Rivals Lithium Ion Capacitors. *Energy Environ. Sci.* **2015**, *8* (3), 941–955.
(109) Thangavel, R.; Moorthy, B.; Kim, D. K.; Lee, Y.-S. Pushing the Energy Output and Cyclability of Sodium Hybrid Capacitors at High Power to New Limits. *Adv. Energy Mater.* **2017**, *7* (14), 1602654.
(110) Thangavel, R.; Kaliyappan, K.; Kang, K.; Sun, X.; Lee, Y.-S. Going Beyond Lithium Hybrid Capacitors: Proposing a New High-Performing Sodium Hybrid Capacitor System for Next-Generation Hybrid Vehicles Made with Bio-Inspired Activated Carbon. *Adv. Energy Mater.* **2016**, *6* (7), 1502199.
(111) Kaliyappan, K.; Chen, Z. Atomic-Scale Manipulation of Electrode Surface to Construct Extremely Stable High-Performance Sodium Ion Capacitor. *Nano Energy* **2018**, *48*, 107–116.
(112) Qu, Q.; Zhu, Y.; Gao, X.; Wu, Y. Core-Shell Structure of Polypyrrole Grown on V2O5 Nanoribbon as High Performance Anode Material for Supercapacitors. *Adv. Energy Mater.* **2012**, *2* (8), 950–955.
(113) Li, H.; Lang, J.; Lei, S.; Chen, J.; Wang, K.; Liu, L.; Zhang, T.; Liu, W.; Yan, X. A High-Performance Sodium-Ion Hybrid Capacitor Constructed by Metal-Organic Framework-Derived Anode and Cathode Materials. *Adv. Funct. Mater.* **2018**, *28* (30), 1800757.
(114) Wei, T.; Yang, G.; Wang, C. Iso-Oriented NaTi 2 (PO 4 ) 3 Mesocrystals as Anode Material for High-Energy and Long-Durability Sodium-Ion Capacitor. *ACS Appl. Mater. Interfaces* **2017**, *9* (37), 31861–31870.
(115) Zhu, Y.-E.; Yang, L.; Sheng, J.; Chen, Y.; Gu, H.; Wei, J.; Zhou, Z. Fast Sodium Storage in TiO 2 @CNT@C Nanorods for High-Performance Na-Ion Capacitors. *Adv. Energy Mater.* **2017**, *7* (22), 1701222.
(116) Kim, J. W.; Augustyn, V.; Dunn, B. The Effect of Crystallinity on the Rapid Pseudocapacitive Response of Nb2O5. *Adv. Energy Mater.* **2012**, *2* (1), 141–148.
(117) Dong, S.; Shen, L.; Li, H.; Nie, P.; Zhu, Y.; Sheng, Q.; Zhang, X. Pseudocapacitive Behaviours of Na2Ti3O7@CNT Coaxial Nanocables for High-Performance Sodium-Ion Capacitors. *J. Mater. Chem. A* **2015**, *3* (42), 21277–21283.
(118) Kubota, K.; Yokoh, K.; Yabuuchi, N.; Komaba, S. Na2CoPO4F as a High-Voltage Electrode Material for Na-Ion Batteries. *Electrochemistry* **2014**, *82* (10), 909–911.
(119) Sanz, F.; Parada, C.; Ruíz-Valero, C. Crystal Growth, Crystal Structure and Magnetic Properties of Disodium Cobalt Fluorophosphate. *J. Mater. Chem.* **2001**, *11* (1), 208–211.

(120) Ling, R.; Cai, S.; Shen, S.; Hu, X.; Xie, D.; Zhang, F.; Sun, X.; Yu, N.; Wang, F. Synthesis of Carbon Coated Na2FePO4F as Cathode Materials for High-Performance Sodium Ion Batteries. *J. Alloys Compd.* **2017**, *704*, 631–640.
(121) Khasanova, N. R.; Drozhzhin, O. A.; Storozhilova, D. A.; Delmas, C.; Antipov, E. V. New Form of Li $_2$ FePO $_4$ F as Cathode Material for Li-Ion Batteries. *Chem. Mater.* **2012**, *24* (22), 4271–4273.
(122) Ellis, B. L.; Makahnouk, W. R. M.; Rowan-Weetaluktuk, W. N.; Ryan, D. H.; Nazar, L. F. Crystal Structure and Electrochemical Properties of A $_2$ MPO $_4$ F Fluorophosphates (A = Na, Li; M = Fe, Mn, Co, Ni) †. *Chem. Mater.* **2010**, *22* (3), 1059–1070.
(123) Recham, N.; Chotard, J. N.; Jumas, J. C.; Laffont, L.; Armand, M.; Tarasco, J. M. Ionothermal Synthesis of Li-Based Fluorophosphates Electrodes. *Chem. Mater.* **2010**, *22* (3), 1142–1148.
(124) Momma, K.; Izumi, F.; IUCr. *VESTA 3* for Three-Dimensional Visualization of Crystal, Volumetric and Morphology Data. *J. Appl. Crystallogr.* **2011**, *44* (6), 1272–1276.
(125) Hammond, R.; Barbier, J. Structural Chemistry of NaCoPO4. *Acta Crystallogr. Sect. B Struct. Sci.* **1996**, *52* (3), 440–449.
(126) Wang, D.; Xiao, J.; Xu, W.; Nie, Z.; Wang, C.; Graff, G.; Zhang, J. G. Preparation and Electrochemical Investigation of Li2CoPO4F Cathode Material for Lithium-Ion Batteries. *J. Power Sources* **2011**, *196* (4), 2241–2245.
(127) Kaliyappan, K.; Chen, Z. Facile Solid-State Synthesis of Eco-Friendly Sodium Iron Silicate with Exceptional Sodium Storage Behaviour. *Electrochim. Acta* **2018**, *283*, 1384–1389.
(128) Banach, M.; Kowalski, Z.; Wzorek, Z.; Gorazda, K. A Chemical Method of the Production of "Heavy" Sodium Tripolyphosphate with the High Content of Form I or Form II. *Polish J. Chem. Technol.* **2009**, *11* (2), 13–20.
(129) Moulder, J.; Stickle, W.; Sobol, P.; Bomben, K. *Handbook of X-Ray Photoelectron Spectroscopy*; 1995.
(130) Wu, Q. H.; Thißen, A.; Jaegermann, W. XPS and UPS Study of Na Deposition on Thin Film V2 O5. *Appl. Surf. Sci.* **2005**, *252* (5), 1801–1805.
(131) Li, Q.; Liu, Z.; Zheng, F.; Liu, R.; Lee, J.; Xu, G. L.; Zhong, G.; Hou, X.; Fu, R.; Chen, Z.; et al. Identifying the Structural Evolution of the Sodium Ion Battery Na2FePO4F Cathode. *Angew. Chemie - Int. Ed.* **2018**, *57* (37), 11918–11923.
(132) Okada, S.; Ueno, M.; Uebou, Y.; Yamaki, J. I. Fluoride Phosphate Li2CoPO4F as a High-Voltage Cathode in Li-Ion Batteries. *J. Power Sources* **2005**, *146* (1–2), 565–569.
(133) Wei, C.; Cheng, C.; Zhou, B.; Yuan, X.; Cui, T.; Wang, S.; Zheng, M.; Pang, H. Hierarchically Porous NaCoPO 4 -Co 3 O 4 Hollow Microspheres for Flexible Asymmetric Solid-State Supercapacitors. *Part. Part. Syst. Charact.* **2015**, *32* (8), 831–839.
(134) Quinlan, R. A.; Lu, Y.-C.; Kwabi, D.; Shao-Horn, Y.; Mansour, A. N. XPS Investigation of the Electrolyte Induced Stabilization of LiCoO 2 and "AlPO 4 "-Coated LiCoO 2 Composite Electrodes. *J. Electrochem. Soc.* **2016**, *163* (2), A300–A308.
(135) Brezesinski, T.; Wang, J.; Tolbert, S. H.; Dunn, B. Ordered Mesoporous α-MoO3with Iso-Oriented Nanocrystalline Walls for Thin-Film Pseudocapacitors. *Nat. Mater.* **2010**, *9* (2), 146–151.
(136) Wang, J.; Polleux, J.; Lim, J.; Dunn, B. Pseudocapacitive Contributions to Electrochemical Energy Storage in TiO2(Anatase) Nanoparticles. *J. Phys. Chem. C* **2007**,

*111* (40), 14925–14931.
(137) Gutierrez, A.; Kim, S.; Fister, T. T.; Johnson, C. S. Microwave-Assisted Synthesis of NaCoPO4 Red-Phase and Initial Characterization as High Voltage Cathode for Sodium-Ion Batteries. *ACS Appl. Mater. Interfaces* **2017**, *9* (5), 4391–4396.
(138) Wang, C.; Wang, F.; Liu, Z.; Zhao, Y.; Liu, Y.; Yue, Q.; Zhu, H.; Deng, Y.; Wu, Y.; Zhao, D. N-Doped Carbon Hollow Microspheres for Metal-Free Quasi-Solid-State Full Sodium-Ion Capacitors. *Nano Energy* **2017**, *41*, 674–680.
(139) Jung, H. G.; Venugopal, N.; Scrosati, B.; Sun, Y. K. A High Energy and Power Density Hybrid Supercapacitor Based on an Advanced Carbon-Coated Li4Ti5O12electrode. *J. Power Sources* **2013**, *221*, 266–271.
(140) Lim, E.; Changshin, J.; Kim, M. S.; Kim, M. H.; Chun, J.; Kim, H.; Park, J.; Roh, K. C.; Kang, K.; Yoon, S.; et al. High-Performance Sodium-Ion Hybrid Supercapacitor Based on Nb2O5@Carbon Core–Shell Nanoparticles and Reduced Graphene Oxide Nanocomposites. *Adv. Funct. Mater.* **2016**, *26* (21), 3711–3719.
(141) Chen, Z.; Augustyn, V.; Jia, X.; Xiao, Q.; Dunn, B.; Lu, Y. High-Performance Sodium-Ion Pseudocapacitors Based on Hierarchically Porous Nanowire Composites. *ACS Nano* **2012**, *6* (5), 4319–4327.
(142) Yin, J.; Qi, L.; Wang, H. Sodium Titanate Nanotubes as Negative Electrode Materials for Sodium-Ion Capacitors. *ACS Appl. Mater. Interfaces* **2012**, *4* (5), 2762–2768.
(143) Shu, J. Electrochemical Behavior and Stability of Li4Ti5O12 in a Broad Voltage Window. *J. Solid State Electrochem.* **2009**, *13* (10), 1535–1539.
(144) Huang, M.; Xu, A.; Duan, H.; Wu, S. Enhanced Pseudocapacitance Contribution to Outstanding Li-Storage Performance for a Reduced Graphene Oxide-Wrapped FeS Composite Anode. *J. Mater. Chem. A* **2018**, *6* (16), 7155–7161.
(145) Li, H.; Zhu, Y.; Dong, S.; Shen, L.; Chen, Z.; Zhang, X.; Yu, G. Self-Assembled $Nb_2O_5$ Nanosheets for High Energy–High Power Sodium Ion Capacitors. *Chem. Mater.* **2016**, *28* (16), 5753–5760.
(146) Chen, Z.; Augustyn, V.; Wen, J.; Zhang, Y.; Shen, M.; Dunn, B.; Lu, Y. High-Performance Supercapacitors Based on Intertwined CNT/V2O5 Nanowire Nanocomposites. *Adv. Mater.* **2011**, *23* (6), 791–795.
(147) Wang, H.; Zhang, Y.; Ang, H.; Zhang, Y.; Tan, H. T.; Zhang, Y.; Guo, Y.; Franklin, J. B.; Wu, X. L.; Srinivasan, M.; et al. A High-Energy Lithium-Ion Capacitor by Integration of a 3D Interconnected Titanium Carbide Nanoparticle Chain Anode with a Pyridine-Derived Porous Nitrogen-Doped Carbon Cathode. *Adv. Funct. Mater.* **2016**, *26* (18), 3082–3093.
(148) Huang, H.; Kundu, D.; Yan, R.; Tervoort, E.; Chen, X.; Pan, L.; Oschatz, M.; Antonietti, M.; Niederberger, M. Fast Na-Ion Intercalation in Zinc Vanadate for High-Performance Na-Ion Hybrid Capacitor. *Adv. Energy Mater.* **2018**, *8* (35), 1802800.
(149) Zhao, X.; Cai, W.; Yang, Y.; Song, X.; Neale, Z.; Wang, H. E.; Sui, J.; Cao, G. MoSe2 Nanosheets Perpendicularly Grown on Graphene with Mo–C Bonding for Sodium-Ion Capacitors. *Nano Energy* **2018**, *47*, 224–234.
(150) Thangavel, R.; Ponraj, R.; Kannan, A. G.; Kaliyappan, K.; Kim, D. W.; Chen, Z.; Lee, Y.-S. High Performance Organic Sodium-Ion Hybrid Capacitors Based on Nano-Structured Disodium Rhodizonate Rivaling Inorganic Hybrid Capacitors. *Green Chem.* **2018**, *20* (21), 4920–4931.
(151) Zhao, B.; Chen, D.; Xiong, X.; Song, B.; Hu, R.; Zhang, Q.; Rainwater, B. H.; Waller, G. H.; Zhen, D.; Ding, Y.; et al. A High-Energy, Long Cycle-Life Hybrid Supercapacitor

Based on Graphene Composite Electrodes. *Energy Storage Mater.* **2017**, *7*, 32–39.
(152) Zhang, S. S.; Xu, K.; Jow, T. R. EIS Study on the Formation of Solid Electrolyte Interface in Li-Ion Battery. *Electrochim. Acta* **2006**, *51* (8–9), 1636–1640.
(153) Bodenes, L.; Darwiche, A.; Monconduit, L.; Martinez, H. The Solid Electrolyte Interphase a Key Parameter of the High Performance of Sb in Sodium-Ion Batteries: Comparative X-Ray Photoelectron Spectroscopy Study of Sb/Na-Ion and Sb/Li-Ion Batteries. *J. Power Sources* **2015**, *273*, 14–24.
(154) Dahéron, L.; Dedryvère, R.; Martinez, H.; Ménétrier, M.; Denage, C.; Delmas, C.; Gonbeau, D. Electron Transfer Mechanisms upon Lithium Deintercalation from LiCoO 2 to CoO2 Investigated by XPS. *Chem. Mater.* **2008**, *20* (2), 583–590.
(155) Zhang, J.; Wang, W.; Wang, W.; Wang, S.; Li, B. Comprehensive Review of P2-Type Na 2/3 Ni 1/3 Mn 2/3 O 2 , a Potential Cathode for Practical Application of Na-Ion Batteries. *ACS Appl. Mater. Interfaces* **2019**, *11* (25), 22051–22066.
(156) Wang, L.; Sun, Y.-G.; Hu, L.-L.; Piao, J.-Y.; Guo, J.; Manthiram, A.; Ma, J.; Cao, A.-M. Copper-Substituted Na 2/3 Ni 0.3−x Cu x Mn 0.7 O 2 Cathode Materials for Sodium-Ion Batteries with Suppressed P2–O2 Phase Transition. *J. Mater. Chem. A* **2017**, *5* (18), 8752–8761.
(157) Li, X.; Liu, J.; Meng, X.; Tang, Y.; Banis, M. N.; Yang, J.; Hu, Y.; Li, R.; Cai, M.; Sun, X. Significant Impact on Cathode Performance of Lithium-Ion Batteries by Precisely Controlled Metal Oxide Nanocoatings via Atomic Layer Deposition. *J. Power Sources* **2014**, *247*, 57–69.
(158) Kaliyappan, K.; Or, T.; Deng, Y.; Hu, Y.; Bai, Z.; Chen, Z. Constructing Safe and Durable High-Voltage P2 Layered Cathodes for Sodium Ion Batteries Enabled by Molecular Layer Deposition of Alucone. *Adv. Funct. Mater.* **2020**, 1910251.
(159) Liu, Y.; Fang, X.; Zhang, A.; Shen, C.; Liu, Q.; Enaya, H. A.; Zhou, C. Layered P2-Na2/3[Ni1/3Mn2/3]O2 as High-Voltage Cathode for Sodium-Ion Batteries: The Capacity Decay Mechanism and Al2O3 Surface Modification. *Nano Energy* **2016**, *27*, 27–34.
(160) Alvarado, J.; Ma, C.; Wang, S.; Nguyen, K.; Kodur, M.; Meng, Y. S. Improvement of the Cathode Electrolyte Interphase on P2-Na2/3Ni1/3Mn2/3O2 by Atomic Layer Deposition. *ACS Appl. Mater. Interfaces* **2017**, *9* (31), 26518–26530.
(161) Park, J. S.; Meng, X.; Elam, J. W.; Hao, S.; Wolverton, C.; Kim, C.; Cabana, J. Ultrathin Lithium-Ion Conducting Coatings for Increased Interfacial Stability in High Voltage Lithium-Ion Batteries. *Chem. Mater.* **2014**, *26* (10), 3128–3134.
(162) Komaba, S.; Yabuuchi, N.; Nakayama, T.; Ogata, A.; Ishikawa, T.; Nakai, I. Study on the Reversible Electrode Reaction of Na 1– x Ni 0.5 Mn 0.5 O 2 for a Rechargeable Sodium-Ion Battery. *Inorg. Chem.* **2012**, *51* (11), 6211–6220.
(163) Wang, K.; Yan, P.; Sui, M. Phase Transition Induced Cracking Plaguing Layered Cathode for Sodium-Ion Battery. *Nano Energy* **2018**, *54*, 148–155.
(164) Sehrawat, D.; Zhang, J.; Yu, D. Y. W.; Sharma, N. In Situ Studies of Li/Cu-Doped Layered P2 Na x MnO 2 Electrodes for Sodium-Ion Batteries. *Small Methods* **2019**, *3* (4), 1800092.
(165) Riley, L. A.; Van Atta, S.; Cavanagh, A. S.; Yan, Y.; George, S. M.; Liu, P.; Dillon, A. C.; Lee, S.-H. Electrochemical Effects of ALD Surface Modification on Combustion Synthesized LiNi1/3Mn1/3Co1/3O2 as a Layered-Cathode Material. *J. Power Sources* **2011**, *196* (6), 3317–3324.
(166) Edström, K.; Gustafsson, T.; Thomas, J. O. The Cathode–Electrolyte Interface in the Li-

Ion Battery. *Electrochim. Acta* **2004**, *50* (2–3), 397–403.
(167) Hadži-Jordanov, S. Reversibility and Growth Behavior of Surface Oxide Films at Ruthenium Electrodes. *J. Electrochem. Soc.* **1978**, *125* (9), 1471.